5-2024

Engineering Multifunctional Silicon Nanostructures from Biorenewable Cellulose Nanocrystals

Nancy Chen
nchen4@g.clemson.edu

ENGINEERING MULTIFUNTIONAL SILICON NANOSTRUCTURES FROM BIORENEWABLE CELLULOSE NANOCRYSTALS

A Thesis
Presented to
the Graduate School of
Clemson University

In Partial Fulfillment
of the Requirements for the Degree
Doctor of Philosophy
Automotive Engineering

---

by
Nancy Chen
May 2024

Accepted by:
Dr. Srikanth Pilla, Committee Chair
Dr. Morteza Sabet, Co-Chair
Dr. Craig Clemons
Dr. Apparao M. Rao
Dr. Jiangfeng Zhang

ABSTRACT

The imperative search for alternative materials to address the pressing demand for advance energy storage is underscored by the escalating environmental predicaments. Lithium-ion batteries (LIBs) with graphite anodes have become the benchmark in energy storage; however, they are approaching a saturation point in terms of energy density. Silicon emerges as a promising contender to supplant graphite, owing to its profuse availability, cost-effectiveness, and impressive specific capacity of 4200 mAh g^{-1}. By integrating silicon anodes, LIBs stand to undergo a radical transformation, markedly diminishing in weight and size, thus heralding a novel wave of compact, lightweight energy storage systems. Nonetheless, the incorporation of silicon in LIBs is not without its share of technical impediments, particularly the volume change (approximately 300%) during electrochemical cycling. This volumetric fluctuation can lead to compromised electrical contacts and diminishing capacity retention through the battery's lifespan.

In the burgeoning realm of sustainable materials, bio-based substances have carved a niche, capturing attention for their renewable credentials and the potential for realizing high-value end products with minimized ecological footprint. Cellulose, crowned as the planet's most abundant biopolymer, can offer a greener approach to synthesizing Si nanomaterials. This study adopts an economical and eco-conscious method to develop hollow and porous silicon-based anodes, leveraging bio-derived cellulose nanocrystals as a sacrificial template. The resulting silica materials unveil remarkable attributes, including enhanced porosity and a hollow structure, resulting in an exceptionally high surface area and pore volume when compared to commercial products. This research also explores the conversion of silica to elemental silicon while preserving the unique templated morphology, yielding SiNQ materials with performance metrics comparable to commercially available silicon materials. This approach also addresses and mitigates

environmental concerns associated with conventional metallothermic conversion processes. Furthermore, we scrutinize the lithium-ion diffusion within SiNQ, whose intricate composition encompasses pure silicon, silicon monoxides, and silicon dioxide. Employing GITT, we evaluate SiNQ's electrochemical attributes, focusing on kinetic rate constants and transport properties. This investigation strives to reconcile the promise of silicon-based anodes with their practical deployment in LIBs, advancing towards high-performance, environmentally responsible energy storage solutions.

ACKNOWLEDGEMENTS

First and foremost, my deepest gratitude goes to Dr. Srikanth Pilla, who gave me the opportunity to pursue this journey. His guidance, expertise, and patience have greatly enriched my research experience. I am equally thankful to Dr. Morteza Sabet for his insightful advice and contributions that have significantly enhanced the quality of my work. Dr. Apparao Rao's expertise in lithium-ion batteries have been instrumental in shaping my research direction. I owe much gratitude to Dr. Craig Clemons for his expertise on CNCs and for providing CNCs necessary for my research. My dissertation committee deserves special recognition for their insightful critiques and contributions that deepened my understanding and research.

Further appreciation goes to Nawraj Sapkota for his invaluable help with synthesis in the lab and to Mihir Parekh for his guidance and pivotal role in developing the GITT model. I am grateful to Dr. James Sternberg, Dr. Ting Zheng, and Dr. Sai Aditya Pradeep for their knowledge and expertise. A heartfelt thanks to the laboratory assistants—Tyler McCraw, Cassidy Walsh, Rithvik Reddy Pindi, and Rakesh Ripika—for their diligent contributions.

On a personal note, I am thankful for the friends I've made along this journey who have made the process more enjoyable. My cats, Stinky and Peaches, have been a constant source of emotional support. I am grateful to my family for their financial support. Lastly, I would like to thank my husband, whose constant support and love make everything better.

Table of Contents

LIST OF FIGURES

Figure Page

LIST OF TABLES

Table Page

Chapter One : INTRODUCTION

1.1. Motivation

The growing population and dependence on fossil fuels are overwhelming our supply of a finite resource and limiting the availability for future generations. Energy storage devices are emerging as a replacement to conventional fuel-based technologies in order to meet emissions goals set by world governments subsequently leading to the rapid electrification of the transportation sector [1]. With the support of the public and global superpowers, major original equipment manufacturers (OEMs) have committed to phasing out internal combustion engine vehicles (ICEVs) and committing to all electric line ups [2]. Lithium-ion batteries (LIBs) serve as the principal technology for energy storage in battery electric vehicles (BEVs). Currently, graphite is the predominant anode material for commercial LIBs due to its low cost, availability, superior electrochemical performance, and long cycling stability [3]. LIB electrodes are continuously evolving due to demands for higher energy density, especially coming from the automotive sectors as the energy density increase will help to improve the range of the vehicle while simultaneously allowing the manufacturer to reduce the size and weight of the battery component for vehicle performance [4]. Research initiatives are directed on finding alternative anode materials that can offer a significantly higher theoretical capacity compared to graphite. Table 1.1 summarizes the most promising alloyable metals that are being investigated by researchers due to their advantage in gravimetric capacity. Silicon (Si) stands out as the leading contender because due to its superior gravimetric capacity (~4200 mAh g^{-1}) compared to other elements and graphite anodes (~372 mAh g^{-1}) [5]. Apart from its high theoretical capacity, Si is the second most abundant chemical element on Earth, so Si can address concerns regarding sustainability. Additionally, Tesla's acquisition of SilLion Inc, a startup working on the

development of commercial high-energy density batteries using Si, has fortified that Si will emerge as the next anode material [6]. However, the significant capacity advantage comes at a cost. Si-based electrodes experience rapid deterioration owing to the substantial volume expansion (around 400%) of Si particles during the process of lithiation [7]. This recurrent expansion and contraction cause the fragmentation of Si particles, leading to reduced cycling stability as a result of the particles losing electrical connectivity with the current collector [8]. However, the commercialization of Si for LIB anodes is still a high priority for researchers and industry as the high theoretical capacity can drastically enhance the energy density of LIBs. A vehicle batter typically undergoes more than 1000 charging cycles, an estimated 5-10 years, so cycling stability of the Si material is an important factor in Si anode battery testing [9]. In the early research stages of Si anode testing, electrode half cells are often used as they are easy to make and provide insight on the performance of the Si materials. However, full cell testing is required to evaluate the full cell performance of Si anodes for a more accurate characterization of the material capability. Full cell testing can provide valuable information regarding the battery specific energy, specific power, and energy density.

Table 1.1. Characteristics of lithium-alloying metals from Ref [10].

Elements	**Si**	**Sn**	**Al**	**Ge**	**Bi**	**Sb**
Density (g cm^{-3})	2.3	5.8	2.7	5.3	9.8	6.7
Conductivity (S m^{-1})	1×10^3	9.1×10^6	3.8×10^7	2×10^3	7.7×10^5	2.5×10^6
Gravimetric Capacity (mAh g^{-1})	4200	959	993	1600	385	660

Volumetric Capacity (mAh cm^{-3})	9782	7063	2681	8526	3765	4422
Average potential (V)	0.40	0.50	0.38	0.60	3.3	0.95

However, the sole implementation of Si for LIBs is regarded as impractical due to the swelling of the battery cells during testing [11]. Various strategies have been implemented to suppress the volume expansion of Si materials in pursuit of successful commercialization. However, cost considerations are paramount as some of these methodologies may not be economically viable at scale. It is posited that for the effective incorporation of Si in LIBs, a multifaceted strategy may be adopted to address the challenges posed by volumetric changes. This review seeks to underscore several proposed strategies, such as employing porous Si structures to offer void spaces for accommodating volume expansion, and the combined use of Si with graphite materials. Furthermore, it will delve into the latest advancements in employing Si anodes in full cell evaluations, as part of ongoing efforts to achieve viable commercialization capable of fulfilling the intense energy requisites of the automotive industry.

1.2. Key Objectives

This review aims to highlight the current strategies for the synthesis of 1-dimensional Si structures, detailing the advantages and limitations to each method. Furthermore, examining the benefits of porous Si architectures compared to bulk materials and investigate synthesis methods for producing porous 1-dimensional structures, with a focus on employing environmentally friendly chemical processes. The sol-gel process emerges as a cost-effective and environmentally friendly method to synthesize Si-based materials with distinctive geometries. However, the sol-gel products will require conversion to elemental Si for LIB applications. This review will examine

the prevailing metallothermic reduction technique as a viable method for transforming silica into Si and detailing some of the constraints associated with these processes. The two primary metallothermic reduction pathways will be highlighted and an extensive review will be completed to examine the product performance for LIB applications. Additionally, this review will also explore the current approach for the commercialization of Si materials, which include the application of carbon coating and graphite co-utilization to effectively balance the enhanced capacity with cycling stability. Finally, this review will examine the diffusion kinetics of lithium-ions within 1-dimensional, porous Si architectures. It will outline the prevailing challenges in accurately determining the lithium-ion diffusion coefficients in Si materials, due to the intricate properties of alloyable active materials that undergo phase transformations and significant volume change.

From the literature review, the primary goal of this dissertation is to address the existing research gap in sol-gel science, metallothermic reduction, and electrochemical modeling. The first study aims to introduce a cost-effective and eco-friendly approach for the synthesis of 1-dimensional Si materials through the sol-gel process. Then, this dissertation will explore the challenges and limitations of the metallothermic reduction technique and present a cost-effective solution to produce materials that will preserve their 1-dimensional, porous morphology. Lastly, given the insufficient research on lithium-ion diffusion kinetics within 1-dimensional, porous materials undergoing phase transformations, this work seeks to develop a precise model mirroring experimental observations.

1.3. Si-based Anodes for Lithium-ion Batteries

1.3.1. Methods of Fabricating 1D Si Structures

Numerous techniques exist for creating one-dimensional Si structures suitable for lithium-ion battery applications, each with its own set of pros and cons. Metal-assisted chemical etching (MACE) is a viable method for producing 1-dimensional Si structures. MACE is a popular wet chemical etching method due to its advantages of producing high aspect ratio materials while simultaneously introducing porosity in a single step [12]. The basic operating principles of MACE operates through an initial deposition of metal which is patterned by photolithography for the desired structure onto a Si substrate, followed by the subsequent application of a chemical etchant to selective etch away the metal-deposited regions [13]. However many of these etchants involve combinations of harsh chemicals such as an oxidant (i.e. H_2O_2) with an acid (i.e. HF, HNO_3, or H_2SO_4) which can pose serious safety hazard concerns. To address some of the safety concerns, alkaline etchants (i.e. NaOH, KOH, and LiOH) have been adopted, however these etchants have a significantly slower etching rate compared to acid etchants [14].

The Vapor-Liquid-Solid (VLS) mechanism facilitates the growth of Si nanowires (NWs) through the catalysis of metal droplets, predominantly gold. This process leverages the self-assembly properties of Si vapor, which are drawn to the metallic atoms to form a eutectic liquid phase that subsequently solidifies into NWs [15,16]. VLS is recognized as the principal mechanism for Si NW growth, with several methodologies employing its principles. Among these, Chemical Vapor Deposition (CVD) stands out as a notably prevalent method for NW synthesis, utilizing volatile gaseous Si precursors as the primary material source [17]. Nevertheless, the application of VLS methodologies is not without its drawbacks. The elevated temperatures requisite for these processes can promote Ostwald ripening, leading to the coalescence of smaller particles into larger

aggregates [18]. Such temperatures may also result in the encapsulation of catalytic metal within the Si NW structure, potentially compromising material purity [19,20]. Moreover, the CVD process is critiqued for its environmental and industrial feasibility concerns, primarily due to the substantial generation of solvent waste [21].

Dry etching employs gaseous or plasma-phase etchants, including ions, photons, and electrons, to facilitate material removal through collisions with the substrate within a specialized chamber or vacuum environment [14]. Techniques such as focused ion beam (FIB), wherein gallium ions serve as the etching medium to meticulously sculpt the Si substrate, exemplify this approach [22]. While dry etching presents significant potential for fabricating intricate three-dimensional configurations, its scalability is constrained by extended processing durations for larger structures, thus posing a challenge for broad-scale application.

1.3.2. Methods for Producing Porous Si Materials

The slow diffusion of lithium-ions through solid bulk materials impedes the mass transport of Li-ions, which consequently impacts the rate capabilities of Si materials [23,24]. One effective strategy is to manipulate the morphology of electrode materials. By amplifying the surface area of these materials, there is a consequent increase in the electrode/electrolyte interface, which fosters a greater number of pathways for lithium-ion diffusion. This augmentation in diffusion pathways facilitates lithium ion transfer during charging and discharging, which is pivotal for optimizing battery performance [23]. Furthermore, the ample free volume present within porous materials has the capacity to accommodate the volumetric changes that transpire during the battery's charge and discharge cycles. This not only enhances the efficiency of the battery but also contributes to its structural integrity and cycling stability.

Li et al. investigated the implications of porosity by engineering a large mesoporous Si sponge (MSS) derived from a Si wafer through an electrochemical etching technique [25]. The resultant MSS architecture boasts a highly porous nature, characterized by an average pore diameter of 50 nm, and is encased by slender crystalline Si walls. In-situ TEM experiments were performed to examine the material expansion after full lithiation, shown in Figure 1.1. Following lithiation, the MSS experienced a modest elongation of 7.9% in length and a 13.1% increment in width. When the electrochemical performance of the MSS anode was assessed in juxtaposition with a lithium metal chip serving as the cathode, it was revealed that the battery was capable of delivering a capacity of 750 mAh g-1 and exhibited a capacity retention of 80% over the span of 1000 cycles.

Ge et al. utilized theoretical simulation to better understand the structural stability of Si with porous structures ranging from 1-9 nm in diameter [26]. The authors discerned a pattern, observing that as the size of the prelithiated pores diminished, the stress surrounding these pores escalated, culminating in the fracturing of the material. Through simulations, they deduced that structures with smaller initial pore sizes and a reduced pore volume contribute to the highest degree of material stress. To corroborate the findings from their simulations, they conducted experimental assessments. Porous Si nanowires were fabricated employing a boron-doped Si wafer, which exhibited an average pore diameter of 10.5 nm. The batteries maintained a capacity of 1000 mAh g^{-1} after 2000 cycles at 1 C rate.

Shen et al. conducted a study examining the electrochemical performance of porous Si nanoparticles in contrast to commercially available non-porous Si nanoparticles [27]. They employed in-situ transmission electron microscopy (TEM) to observe changes in material volume post-lithiation. The porous Si nanoparticles underwent a volume change of 145% upon complete

lithiation, in contrast to the substantial volume change of 429% exhibited by the solid Si particles. Furthermore, for the solid Si particles, the nucleation and progression of cracks were evident post-lithiation, while the porous counterparts remained structurally unscathed. Nonetheless, the authors highlighted a drawback associated with high surface area Si nanomaterials, which is the pronounced formation of a solid electrolyte interface (SEI) on the surface. This results in capacity fading, particularly discernible in the early cycles of Si anodes. Due to the SEI formation, porous Si materials should be combined with coatings to mitigate excessive SEI formation.

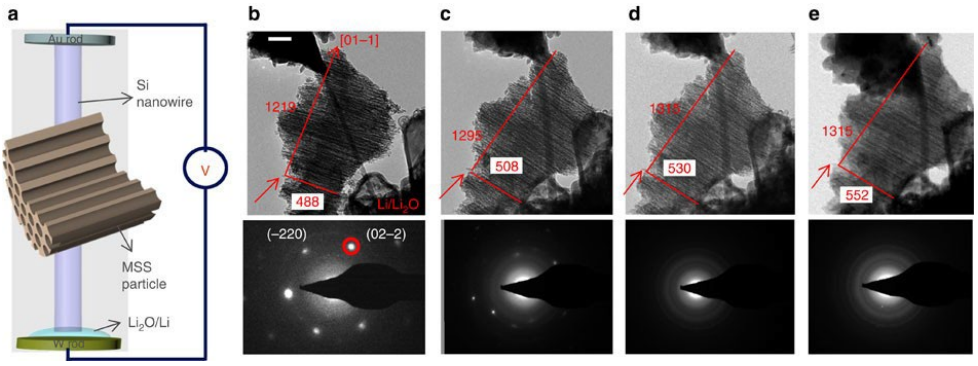

Figure 1.1. In-situ TEM of the lithiation of mesoporous Si sponge material [25]

Although porous structures are beneficial for battery performance and cycling stability, the methodologies currently employed for the creation of these porous materials have elicited safety concerns. Specifically, the utilization of hydrofluoric acid and nitric acid in the synthesis process poses risks due to their corrosive and toxic nature [28–30]. The handling of such chemicals necessitates stringent safety protocols and has the potential for environmental impact. As such, there is a growing demand for alternative, more benign methods of porous material synthesis that circumvent the use of these hazardous substances. The sol-gel process emerged as the prominent technique for the fabrication of materials with organized topologies, through the utilization of templates to guide and shape the resulting morphology [31,32]. The materials

synthesized through the sol-gel method can encompass a diverse array of shapes, sizes, and porosities, with Si dioxide (SiO_2) as their principal chemical composition. However, an imperative step in harnessing SiO_2 materials for such applications is the conversion of SiO_2 to elemental Si, which is achieved through metallothermic reduction.

1.3.3. Metallothermic Reduction of Silica

Within the realm of metallothermic reduction, various methodologies can be discerned, including carbothermic, aluminothermic, and magnesiothermic reduction. [14]. It is crucial to note that carbothermic reduction is encumbered by the requirement of extremely elevated temperatures, often exceeding 1800 °C, for the initiation and sustenance of the pertinent chemical reactions [33]. In contemporary research, the predominant methods for conversion are aluminothermic and magnesiothermic reduction, attributed to the relatively lower temperatures at which these reactions can proceed. These approaches come with both benefits and drawbacks. The aluminothermic reduction method transforms silica into elemental Si with aluminum serving as the reducing agent. Employing metallic aluminum for this reduction necessitates extremely high temperatures (≥700 °C) and often reduction reaction is hindered by the formation of Al2O3 byproduct [34]. To circumvent the challenge of high temperatures, molten salts have been utilized, which can drastically lower the reduction temperature to range from 150 – 300 °C. A detailed finding of Si materials produced via aluminothermic reduction are summarized in Table 1.2.

Table 1.2. Summary of electrochemical cycling performance of Si anodes produced from aluminothermic reduction

Precursor material	Al reduction conditions	Reversible capacity (mAh g^{-1})	Capacity Retention	Ref
Nano silica	Ball mill for 10 h (150 - 180 °C)	1994	40.3% after 400 cycles	[35]
Hollow silica microsphere	270°C	4003	32.9% after 100 cycles	[36]
Porous rice husk	700 °C at a rate of 10 °C/min for 2 h	3096.6	38.9% after 200 cycles	[37]
Porous silica	210 °C for 16 h	2100	76% after 250 cycles	[38]
Porous silica@C	220 °C for 16 h	1950	89% after 250 cycles	
Porous silica nanosheets	350 °C for 12 h	1269	72% after 300 cycles	[39]
Diatomite	250 °C for 12 h	1097.3	80.6% after 200 cycles	[40]
	300 °C for 12 h	1888.7	70.4% after 200 cycles	

The use of aluminum salts as a thermal management strategy in aluminothermic reduction is well-established, with research exploring various salt mixtures, including $ZnCl_2$ [37] $ZnCl_2/AlCl_3$ [38], $NaCl/AlCl_3$ [39], $AlCl_3$ [36,40], and $NaCl/KCl/AlCl_3$ [35]. Research by Ning et al. highlighted that the molten salts serve as a reaction medium facilitating close contact between reactants [41]. Furthermore, the salts can also participate in the reaction process. For procedures where maintaining the original morphology is not essential, high-energy ball milling and elevated

temperature conditions are viable methods for converting silica to Si [35,37]. However, for specifically engineered templated structures, a lower reaction temperature is preferable. Mishra et al. observed morphological decomposition even at a reduction temperature of 210 °C, but this effect was almost entirely mitigated by introducing a carbon pre-coating to the porous SiO_2 (p-SiO2) before the reduction process [38]. Moreover, the battery constructed with the carbon-coated material demonstrated enhanced capacity retention. There appears to be a balance between the extent of conversion, which correlates with the temperature conditions, and the resultant battery performance. Dengke et al. explored two temperature scenarios (250 °C and 300 °C) and discovered that the higher temperature led to a more thorough conversion of silica to Si, as evidenced by XRD analysis [40]. While the material synthesized at the higher temperature exhibited a greater initial capacity, it also experienced a decline in capacity retention.

Alternatively, magnesiothermic reduction has garnered considerable attention within the research community. The Si-based materials synthesized via this particular reduction approach have been subjected to scrupulous investigation pertaining to their performance in batteries. A comprehensive compilation of the findings is encapsulated in Table 1.3. This focus on magnesiothermic reduction signifies its potential importance in the development of high-performance battery materials. The table incorporates an array of mesoporous SiO_2 materials, which are synthesized through sol-gel processes and subsequently converted to Si via magnesiothermic reduction. Numerous reports indicate that the morphological integrity of the initial material remains intact even when subjected to elevated temperatures [42–44]. A detailed investigation by Bao et al. involved examining the morphological features of silica diatom frustules via SEM, followed by assessing the materials post-magnesiothermic reduction at 650 °C

for 2 hours [45]. Their findings reveal minimal morphological deviation from the original structure, most notably the pores remained intact.

Table 1.3. Summary of electrochemical cycling performance of Si anodes produced from magnesiothermic reduction

Starting material	**Mg reduction conditions**	**Reversible capacity (mAh g^{-1})**	**Capacity Retention**	**Ref.**
SBA-15	660 °C for 5 h	350*	50% after 50 cycles*	[42]
SBA-15 coated in carbonized sucrose	660 °C for 5 h	1200*	87.8% after 50 cycles*	
Si nanotube	660 °C for 3 h	1545	65% after 90 cycles*	[43]
SBA-15 coated in carbonized sucrose	660 °C for 5 h	1492	63% after 50 cycles	[44]
Si/SiO_2:C (1:1)	700 °C for 5 h	685.8	75.9% after 50 cycles	[46]
Si/SiO_2:C (1:4)	700 °C for 5 h	438.9	95.5% after 50 cycles	
Silica-gel on Graphene form Si/graphene	675 °C for 8 h	1743	78.8% after 120 cycles	[47]
Silica from rice husk	650 °C for 7 h	2294	57.1% after 100 cycles	[48]
SiO_2 nanosphere	700 °C for 6 h	2980	73.8% after 50 cycles	[49]
SiO_2 (15 nm)	700 °C for 2 h	1866.2	37.2% after 100 cycles	[50]
MCM-41	650 °C for 7 h	1757	68.3% after 100 cycles	[51]
Glass fiber coated with carbon	600 °C for 5 h	1059	47.3% after 150 cycles	[52]

Distinguishing the impacts of magnesium and aluminum reductions proves challenging, as each method presents its own set of compromises. Aluminothermic reduction operates at lower

temperatures yet requires prolonged reaction times, whereas magnesiothermic reduction benefits from markedly shorter reaction durations despite the higher temperatures. Lai et al.'s comprehensive comparative study highlighted significant chemical and physical differences between products obtained via two distinct reduction methods [53]. Intriguingly, when subjected to equivalent processing temperatures, the Si-based materials derived through aluminothermic reduction demonstrated a markedly diminished surface area in contrast to those produced via magnesiothermic reduction, registering surface areas of 6 $m^2 g^{-1}$ and 260 $m^2 g^{-1}$, respectively. This stark contrast in surface area highlights the differential efficacies of the two reduction pathways and offers valuable insights for the strategic selection of reduction techniques. The data presented therein underscores the viability of employing these methodologies as an environmentally friendly and economically feasible avenue for the production of Si materials tailored for use in LIB anodes.

The main challenge with magnesiothermic reduction involves the use of salts, such as NaCl, as heat sinks due to their heat dissipative properties through fusion or melting (ΔH_{fusion} = 28.8 kJ mol^{-1}), which requires very high temperatures up to 800 °C—a condition not typically reached in the conditions outlined in Table 1.3. A notable deficiency in current scholarly understanding pertains to the exploration of heat dissipation mechanisms beyond the conventional reliance on fusion temperatures. This gap in knowledge raises critical questions regarding the potential impact of alternative thermal management strategies on the morphological and compositional attributes of Si-based materials produced via magnesiothermic reduction.

1.3.4. Carbon Coating

Carbon coatings are often applied to help mitigate excessive SEI formation, while simultaneously providing mechanical support and conductivity. There are many approaches to carbon coating including solution-based mixing, hydrothermal carbonization (HTC), chemical

vapor deposition (CVD), and polymer coating [54]. However, due to the various carbon precursor options and treatment methods, the optimization of the carbon outer layer is necessary for commercialization, and a detailed summary of the effects on electrochemical performance is listed on Table 1.4. Xu et al. investigated the performance of commercially available solid Si nanoparticles with and without carbon coating [55]. The carbon layer was achieved by using polyvinylidene fluoride (PVDF) followed by high temperature carbonization at 550, 750, and 950 °C. The carbon coatings treated at 550 and 750 °C resulted in a predominantly amorphous structure, whereas the 950 °C treated carbon possessed a predominantly graphitic structure. The 750 °C treated material and uncoated Si material was investigated using in-situ TEM, shown in Figure 1.2 , where the red arrows indicate the severe cracking of Si nanoparticles in the uncoated Si materials and a more moderate pulverization of the carbon coated Si nanoparticle. Additionally, the in-situ TEM showed that the lithiation occurred faster in the carbon coated structure attributed to the materials increased conductivity. For electrochemical testing, the Si/C-750 electrode has a capacity retention of 84% after 50 cycles; however the long term cycling stability was not considered. When compared to the other materials treated at 550 and 950 °C, the order of increasing battery performance is Si/C-550, Si/C-950, and Si/C-750. However, this study reveals that applying carbon coating techniques alone will not be sufficient to reduce Si pulverization. Additionally, the study also revealed that the carbonization temperature affects the physiochemical properties of carbon and ultimately the battery performance. The same observation was observed in another study with carbon coated commercial Si nanoparticles pyrolyzed at 300, 400, and 500 °C using the spray pyrolysis technique [56]. The discharge capacity after 100 cycles were reported at 10, 288, 1120, and 116 mAh g^{-1} for bare Si, 500, 400, and 300 °C, respectively. The authors

speculate that the 400 °C treatment offers the most optimal carbon weight content, however the coating properties should be explored further.

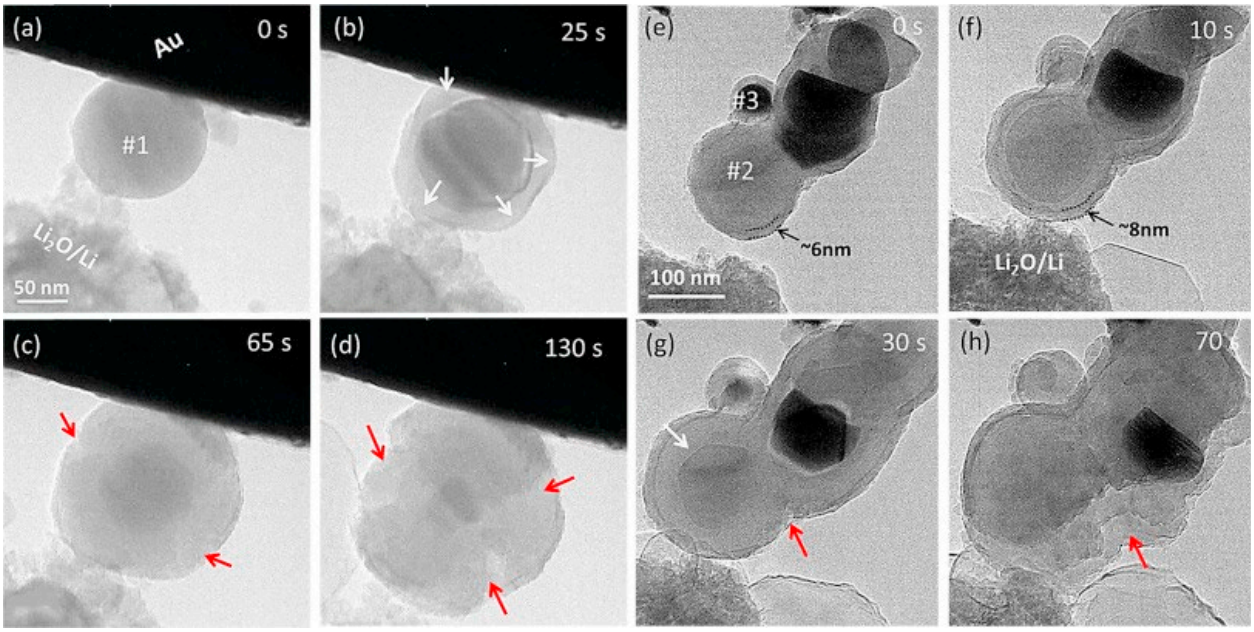

Figure 1.2. In-situ TEM shows the lithiation of bare Si (a-d) and Si with carbonized PVDF coating (e-h). The red arrows indicate crack propagation [55].

Another factor to consider is the type of carbon precursor for the coating. Qi et al. investigated two different types of carbon precursors, pitch and phenolic resin, both carbonized at the same temperature of 900 °C [57]. Despite the same temperature treatment, the carbon obtained from the different precursors are drastically different. After carbonization, the pitch had a carbon content of 25%, while the phenolic resin carbon content was 23%. The carbon layer thickness ranges from 90-180 nm for pitch and 60-170 nm for phenolic resin. The functional groups were analyzed for both coating and concluded that both possess very similar proportions of functional groups. From high resolution TEM images, the pitch carbon structure is comprised of turbostratic short-range ordered carbon, whereas the phenolic resin structure is comprised of amorphous carbon. There is also a drastic difference in surface area: 4.1 $m^2 g^{-1}$ for pitch and 363.8 $m^2 g^{-1}$ for

phenolic resin. From the battery testing results, the capacity of the pitch coated Si was double that of the phenolic resin and the pitch coated Si had superior capacity retention as well. To investigate the failure mechanism, the authors analyzed the electrode thickness after electrochemical cycling, the phenolic resin electrode thickness increased by 140%, whereas the pitch electrode only increased by 88%. Similarly, Lui et al. investigated carbon precursors including pitch, polyethylene glycol (PEO), resin, polyethylene (PE), polyvinyl chloride (PVC), chlorinated polyethylene (CPE), sucrose, and polyvinylidene fluoride (PVDF) [58]. The authors investigated the electrochemical performance of the listed carbon coatings and concluded that the order of increasing capacity retention is resin, sucrose, PVDF, PEO, PE, PVC, and lastly CPE.

Qi et al. investigated the effect of the carbon thickness using commercially available Si nanoparticles [59]. They employed a facile CVD process and used C_3H_6 as the carbon precursor with increasing deposition times (10, 15, 25, 40, and 60 minutes) for increasing carbon thicknesses (0.8, 1, 2.4, 6.07, and 9.73 nm, respectively). The electrochemical performance was analyzed for all carbon thicknesses and determined that the 1 nm carbon coated Si outperformed the other materials, it possessed a specific capacity of 1759 mAh g^{-1} at 0.5 C rate after 500 cycles. The composite material with the largest carbon thickness, 9.73 nm, performed the worst out of all of the materials tested including bare Si. After determining the best performing structure, the Si/C structure with 1 nm carbon coating was evaluated in a full cell configuration paired with an NMC cathode. The full pouch cell achieved a capacity of 32.4 mAh and capacity retention of 68.9% after 500 cycles at 1 C rate. However, the volume expansion of the pouch cell during battery cycling was not investigated by the authors.

Lu et al. explored the electrochemical performance of carbon coated porous Si in the full cell configuration [60]. The authors fabricated porous silica nanoparticles using the cost-effective

Stöber method followed by magnesium reduction to convert the silica to elemental Si, and lastly coated the porous Si with carbon using the CVD method. For half-cell testing, porous Si was compared to carbon coated porous Si, or porous Si/C. The porous Si/C retained a high discharge capacity of 1424 mAh g^{-1} after 600 cycles at 4 A g^{-1}, while the bare porous Si exhibited a gradual capacity fade to 504 mAh g^{-1} after 600 cycles. For full cell testing, the porous Si/C materials showed a discharge capacity of 85 mAh g^{-1} after 200 cycles, which equals to an 88.5% capacity retention. Xu et al. also investigated porous Si/C structures and fabricated their porous Si microspheres using the Stöber method and then applied a carbon coating using CVD [61]. The resulting composite structure was 17.5 wt% carbon. They performed in-situ TEM analysis of their mesoporous Si/C composite materials and reported an 85% increase in volume after lithiation. Additionally, when comparing the in-situ TEM results for commercial Si nanoparticles, commercial Si/C, and mesoporous Si/C, the crack initiation was observed and recorded on Figure 1.3. The crack initiation occurred sooner for the bare commercial Si materials compared to the carbon coated commercial Si. However, even with the carbon coating on the commercial Si, the volume expansion was equal to bare commercial Si. We can conclude that carbon coating methods are only favorable when combined with porous structures.

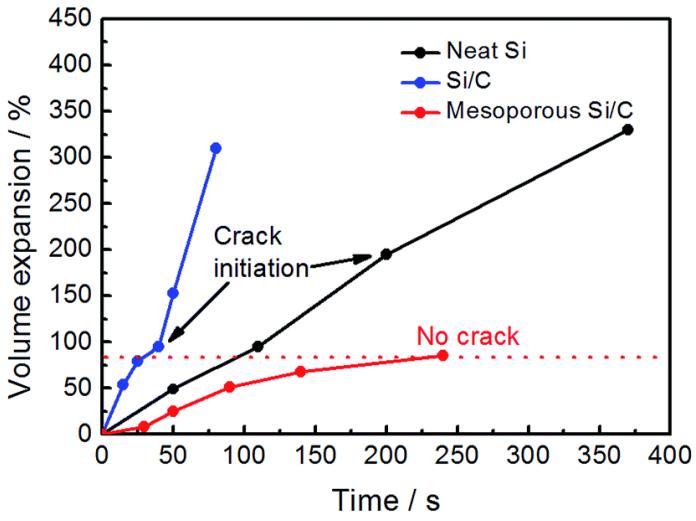

Figure 1.3. The volume expansion of neat commercial Si, commercial Si/C, and mesoporous Si/C observed under in-situ TEM and the recorded crack initiation time [61].

Table 1.4. Summary of Si anode performance with various carbon coating methods on commercial Si nanoparticles and porous Si particles in half cell and full cell configurations.

Active material	**Si source**	**Carbon source**	**Counter electrode**	**Current Density**	**Initial discharge**	**Capacity Retention**	**Ref**
Si/C	Commercial nps	PVDF (750 °C)	Li metal	1C	2382 mA h g^{-1}	84% after 50 cycles	[55]
Si (100 nm)	Commercial nps	none	Li metal	0.2 A g^{-1}	3229 mA h g^{-1}	~39% after 500 cycles	[59]
Si/C (3.68 C wt%)	Commercial nps	C_3H_6 (CVD)	Li metal	0.2 A g^{-1}	2929 mA h g^{-1}	61% after 500 cycles	
Si/C (3.68 C wt%)	Commercial nps	C_3H_6 (CVD)	NMC662	1 C	47 mAh	68.72% after 500 cycles	
Porous Si/C	Stöber method	none	Li metal	4 A g^{-1}	~1250 mA h g^{-1}	40.3% after 600 cycles	[60]
Porous Si/C	Stöber method	Acetylene (800 °C, CVD)	Li metal	1 A g^{-1}	1102 mA h g^{-1}	89.84% after 1000 cycles	[61]
Si/C	Commercial nps	Grafted-PAA	NMC811	0.1 C	2.34 mAh cm^{-2}	70% after 100 cycles	[62]
Porous Si/C	Stöber method	resorcinol formaldehyde (800 °C)	Li metal	50 mA g^{-1}	1637 mA h g^{-1}	64.4% after 100 cycles	[63]
Porous Si/C	Stöber method	C_2H (800 °C, CVD)	Li metal	4 A g^{-1}	~2000 mA h g^{-1}	71.2% after 600 cycles	

Porous Si/C	Stöber method	C_2H (800 °C, CVD)	LFP	1 C	95.8 mA h g^{-1}	88.5% after 200 cycles	
Si	Commercial nps	none	Li metal	2.6 A g^{-1}	3250 mA h g^{-1}	0% after 200 cycles	[64]
Porous Si/C	Stöber method	2,3-dihydroxynaphthalene (800 °C)	Li metal	2.6 A g^{-1}	1467	83% after 370 cycles	

1.3.5. Graphite Utilization

Due to the volume expansion of the Si material during lithiation, implementing a high mass loading of Si as the primary active material is still not possible without severe battery swelling. Most Si anodes tested without graphite co-utilization have not shown high areal capacity or volumetric capacity, primary attributed to the volume change leading to the loss of electrical contact [65]. To fabricate graphite/porous-Si anodes researchers have investigated many fabrication processes. Li et al. fabricated graphite/Si anodes by applying the primary design goals: improve specific capacity (>372 mAh g^{-1}), achieve long-term cycling stability (targeting >80% capacity retention after 500 cycles), improve volumetric capacity (550 mAh cm^{-3}), and suppressed electrode swelling to 10% [66]. The porous Si materials were prepared by chemical etching of Si wafter, followed by carbon coating using CVD method. The porous Si/C to graphite ratio in the slurry was maintained at 1:2 and 1:3. Better cycling stability was observed for the Si/C:graphite (1:3) with a capacity retention of 87% after 450 cycles and 83% after 535 cycles. The Si/C:graphite (1:2) areal capacity was 16.67% greater compared to the ratio of 1:3. The swelling of the (1:2) electrode was observed under SEM before and after cycling. The Si/C:graphite (1:2) electrode swelled 20% after lithiation. They also observed that the standard calendaring process, applied to most slurry coatings to increase density, does not affect the structural stability of the porous Si/C materials. The Si/C:graphite (1:2) anodes were demonstrated in a full cell battery using NMC as the cathode. The full cell did not meet their capacity retention goal with 84% after 300 cycles, but the swelling of the pouch cells was not investigated. It is noteworthy that analogous strategies, involving the utilization of graphite, have been investigated and integrated with porous Si-based materials in an effort to enhance both the capacity and capacity retention of batteries. A

compilation of these findings is systematically presented in Table 1.5. It can be asserted that the synergistic integration of carbon coatings, porous electrode architectures, and amalgamation with graphite manifests in a marked enhancement in the capacity retention of LIBs, as compared to the standalone Si-based anodes depicted in Table 1.4.

Table 1.5. Electrochemical performance of composite Si/graphite anodes in half cells and full cells

Active material	**Si (wt%)**	**Mass loading (mg cm^{-2})**	**Counter electrode**	**Mass loading (mg cm^{-2})**	**Reversible capacity (mAh g^{-1})**	**Capacity retention**	**Ref**
CVD of Si on graphite nps then coated with acetylene	7.6	-	NMC	18.5	~10 mAh	81.9% after 200 cycles	[67]
CVD of Si on graphite nps then coated with pitch	6.9				~10 mAh	66% after 200 cycles	
Commercial Si (300 nm) and Graphite	15	1.2	Half cell (Li chip)		709	68% after 50 cycles	[68]
Graphite/Si nps/Amorphous C (72/10/18)	8	0.85	Half cell (Li chip)		542.9	94.9% after 100 cycles	[69]
Porous Si coated with Carbon (sucrose) mixed with graphite (1:1)	13.5	1.65	Half cell (Li chip)		985.7	75% after 50 cycles	[70]
Porous Si (etched wafer) coated with Carbon (CVD) mixed with graphite (1:2)	33	~2	Half cell (Li chip)		650	82% after 450 cycles	[66]
Porous Si (etched wafer) coated with Carbon (CVD) mixed with graphite (1:3)	25				610	87% after 450 cycles	
Porous Si (etched wafer) coated with Carbon (CVD) mixed with graphite (1:2)	33		NMC	-	~3 mAh (~1500 mAh/g)	84% after 300 cycles	

Boron doped porous Si /CNTs then ball milled with graphite (10 wt% Si/CNT)	8.5	5.1	Al-doped LCO	12	180	82.5% after 300 cycles	[71]
Silica nanotube (CVD)	-	1.0	Half cell (Li chip)		3247	89% after 200 cycles	[72]
CNT@Si@C from Al reduction	66	-	Half cell (Li chip)		~1900	87% after 1500 cycles	[73]
CNT@Si@C from Al reduction	66	-	NMC	-	2850	92% after 500 cycles	
Nano-Si (50 nm) and graphene composite made by GO suspension	100	-	Half cell (Li chip)		3170	13% after 30 cycles	[74]
	55	-			~3100	~26.1% after 30 cycles	
	45	-			~2530	70% after 30 cycles	
	40	-			~2380	78% after 30 cycles	

Sung et al. investigated Si coated graphite particles in pouch cells and larger prismatic cells [75]. Si was coated onto graphite via CVD followed by another carbon coating on the surface and the resulting material has a Si weight loading of 63.1%. The electrochemical performance of the pouch cell and prismatic cell is summarized in Figure 1.4. From the pouch cell results, the graphite/Si/C (carbon coated) achieved superior cycling retention of 80.3% after 500 cycles compared to the non-coated graphite/Si with only 57.6% retention after 500 cycles. In the 110 Ah prismatic cell, the graphite/Si/C materials was able to provide a 91.24% capacity retention after 2875 cycles. The graphite/Si/C pouch cell reported a volume expansion of 13.8% at the first cycle, however the volume expansion was not reported for the prismatic cell.

Fortunately, Chae et al. investigated the swelling of the pouch cell stack with increasing Si loading [11]. Shown in Figure 1.5, are the extent of pouch swelling and the linear relationship between swelling, energy density, and specific capacity. Ideally, swelling should be reduced in order to prevent the bulging of the battery pack. However, there are many factors to consider with electrode swelling. Different active materials may provide porosity to accommodate the swelling. Additionally, the swelling becomes more pronounced in the full cell.

Profatilova et al. investigated the impact of the calendaring process on graphite/Si anodes containing 7 wt.% Si [76]. Composite anodes denoted as 30% “porosity” has a density of 1.55 g cm^{-3} and 40% “porosity” has a density of 1.3 g cm^{-3}. The calendared anodes were tested using a 18650 cylindrical cell. The capacity retention for 30% porosity is 95% after 225 cycles, and 84% capacity retention after 225 cycles for 40% porosity. Additionally, the 40% porosity battery experienced a swelling of 21% after 347 cycles. Similarly for other full cell testing, Lee et al. observed a 16% volume change for graphite/Si/C anodes containing 10 wt.% Si [77], and Jia et al.

reported a 20% initial volume change in graphite/Si/CNT anodes containing around 19 wt.% Si [73].

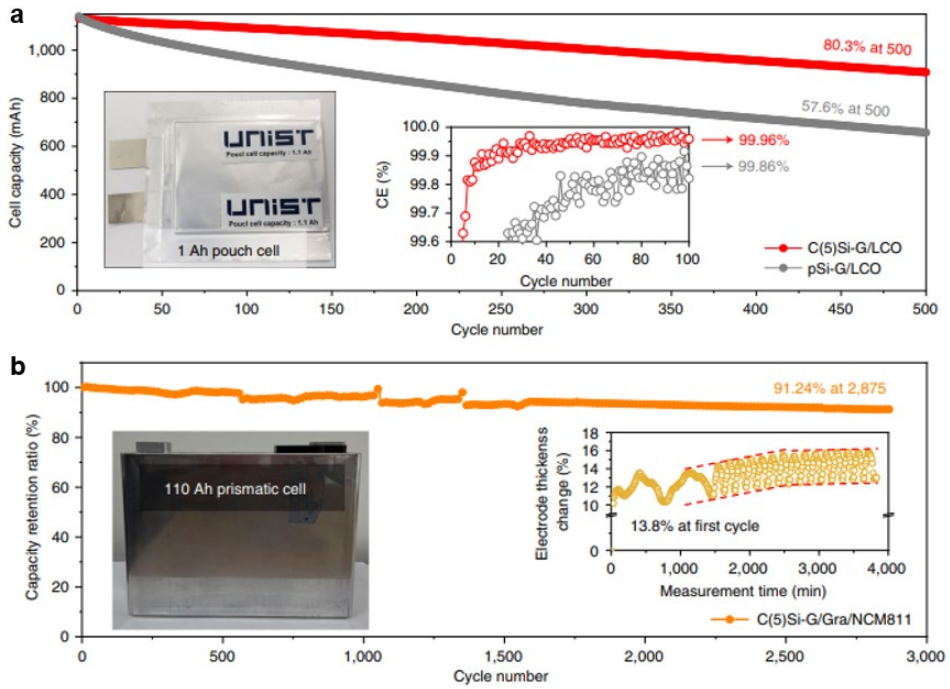

Figure 1.4. Electrochemical performance of graphite coated with Si layer in pouch cell and prismatic cell [75]

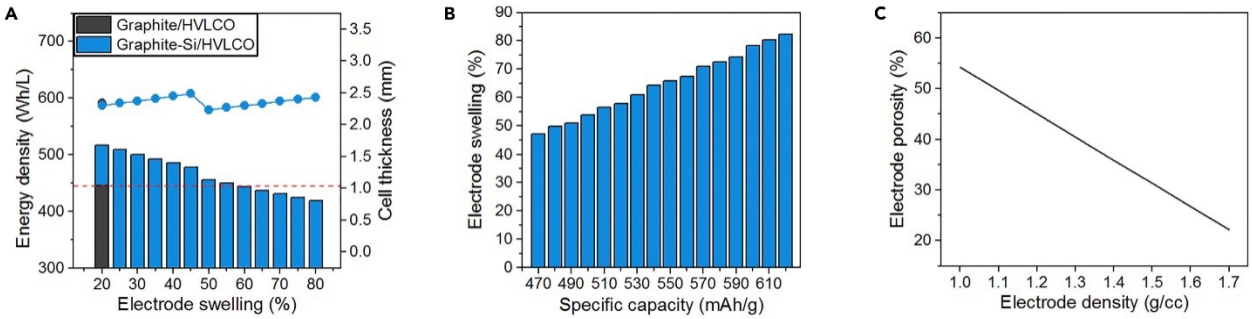

Figure 1.5. Electrode swelling with increasing Si weight fraction [11]

1.3.6. Lithium ion Diffusion Kinetics

Graphite was first introduced as the primary anode material for LIBs in 1983, as documented by Yazumi and Touzain [78]. The electrochemical process facilitating lithium-ion de-/intercalation within graphite is highlighted in Figure 1.6. The graphite provides a stationary carbon framework of graphene layers stacked in the typical ABABA configuration, which can accommodate lithium-ions to achieve the maximum configuration of one lithium-ion for six carbon units (LiC6) equivalent to a theoretical capacity of 372 mAh g^{-1} or a volumetric capacity of 850 mAh cm^{-3} [79]. Intercalation-type materials offer a highly stable capacity with minimal volume expansion (<10%), and the first cycle irreversibility remains relatively low [80,81]. However, the main disadvantage of intercalation-type host materials is the capacity, which is limited due to the number of available interstitial sites for lithium ion accommodation [82].

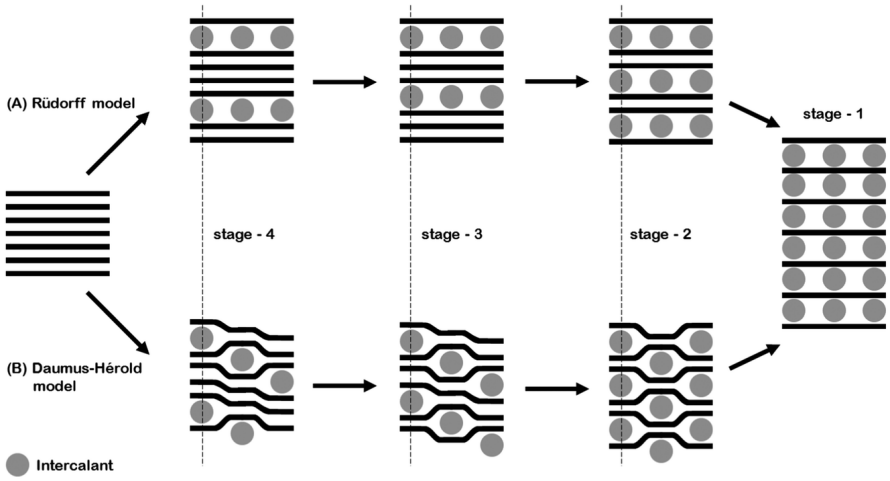

Figure 1.6. Schematic of the primary models of lithium intercalation: (a) Rudorff model and (b) Daumus-Herold model [83]

Alternatively, alloying materials are not constrained by the host's atomic framework to that of intercalation materials. Alloying materials, popularly Si, undergoes drastic structural and phase change when accommodating the Li host allowing for higher lithium concentration of $Li_{22}Si_5$ equating to a theoretical capacity of 4200 mAh g^{-1} [84]. Li-Si alloying involves a chemical reaction and undergoes a phase transformation, converting crystalline Si into an amorphous Li_XSi phase resulting in approximately a 310% volume change [85]. This substantial alteration in volume is a crucial factor to consider when analyzing the structural integrity and performance durability of Si-based anodes. An in-situ analysis showing this phase transformation can be seen in Figure 1.7, the delineation between lithium-free phase (α phase) and the Li-Si phase (β phase) are separated by a moving boundary (represented similarly as the dotted line in the figure) [86]. The lithium ions will diffuse into the interior of the Si particle, continuing their diffusion path until reaching the particle's center. This significant volume change is a crucial aspect to assess when evaluating the structural stability and longevity of Si-based anode materials in lithium-ion batteries.

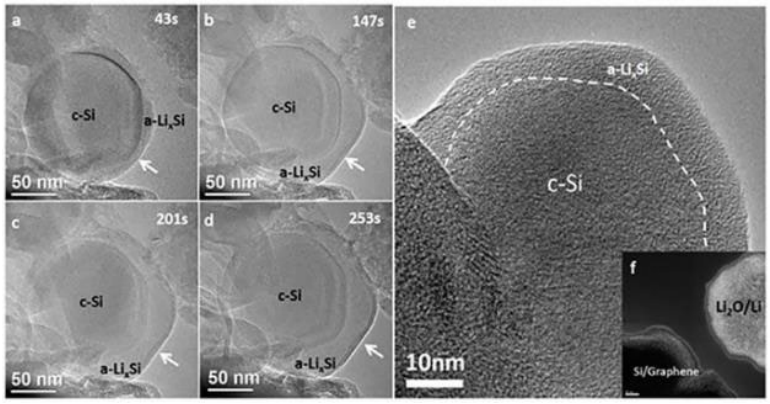

Figure 1.7. Lithiation of crystalline Si nanoparticle, showing the transition from crystalline phase (c-Si) to amorphous Si phase (a-Li$_X$Si) [87]

Important note for host materials for lithium de-/intercalation is the evaluation of a materials electroactive transport characteristics, specifically the kinetics of lithium ion diffusion

[88]. The galvanostatic intermittent titration technique (GITT), a highly regarded and extensively employed electrochemical analysis method, plays a pivotal role in studying the kinetics of lithium ions in LIBs [89]. The GITT method involves applying successive current pulses interspersed with periods of relaxation. The schematic figure in Figure 1.8 details the process, where the assembled battery begins at equilibrium (showing constant voltage) followed by an applied current pulse (labeled b in the image) in which the corresponding voltage response (labeled c in the image) is recorded. The battery is subjected to a series of current pulses until fully discharged and charged.

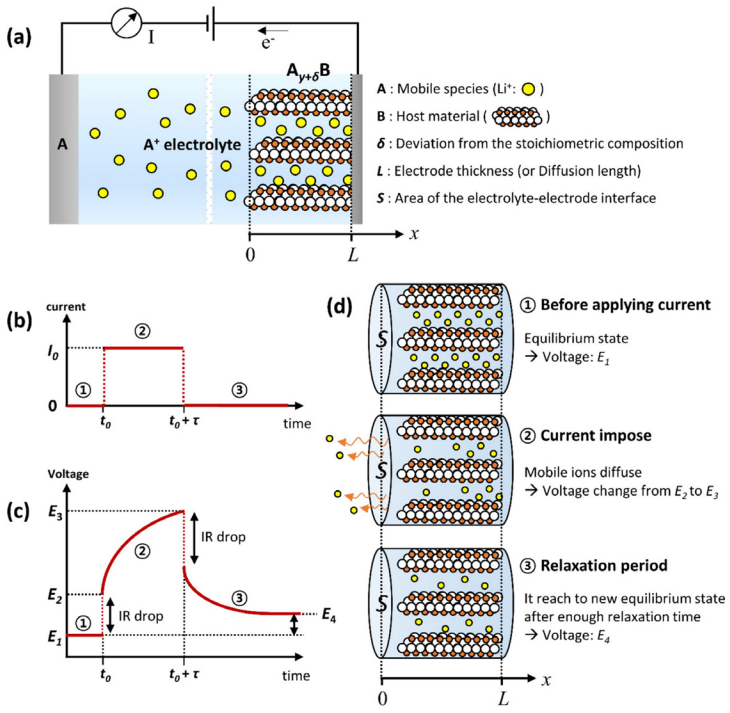

Figure 1.8. Schematic diagram of the GITT procedure showing the current pulse, the corresponding voltage response, and illustrations detailing the movement of ions in the battery [89]

The experimental data derived from GITT necessitates the formulation of mathematical models and equations for interpretation in order to elucidate the kinetics of lithium ion diffusion.

The mechanisms governing electrochemical reactions can all be tied to Fick's law of diffusion [90,91]:

$$J = -D\,\nabla C \tag{1}$$

$$D_S = \frac{4}{\pi}\left(\frac{IV_m}{FS}\right)^2\left(\frac{\frac{dU^0}{dy}}{\frac{dV}{d\sqrt{t}}}\right)^2 \tag{2}$$

where I is the current pulse magnitude, V_m is the molar volume of the active material, F is Faraday's constant, S is the active area of the electrode, U^0 is the open circuit potential, y represents the state of charge, V is the voltage during the current pulse, t is time or length-scale of the current pulse, R is the diffusion length, and lastly $S, \frac{dU^0}{dy}, and \frac{dV}{d\sqrt{t}}$ are obtained from experimental data [90]. The modified diffusion coefficient equation is frequently cited in literature for evaluating lithium kinetics through electrode materials as summarized in Table 1.6. However, this diffusion equation should not be used for Si materials because the equation was derived for one-dimensional diffusion and fails to account for phase transformation, multi-dimensional diffusion paths, and stress related factors [91]. It is crucial to acknowledge that for Si materials, considerations must extend to phase transformations during lithiation and delithiation processes, as well as mechanical stresses associated with significant volume expansion. These aspects are intended for exploration in a future chapter.

Table 1.6. Summary of lithium ion diffusion calculation approaches

Anode material	Diffusion Calculation	Modeling Approach	Ref
SiO nanoparticles (<80 nm)	Eq. 1	-	[92]
Si nanoparticles	Eq. 1	-	[93]
Si nanoparticles	Eq. 1	-	[94]
Si nanoparticles (50 -100 nm)	Eq. 1	-	[95]
Porous 3D Si	Eq. 1	-	[96]
LFP	Mix control phase transformation equation	Phase change and interfacial moving boundary	[91]
NMC	Eq. 1	Mechanical stress effect	[97]
LFP	Mix control phase transformation equation	Mechanical stress effect	[98]

1.4. Summary

This review detailed the current strategies for the synthesis of 1-dimensional Si structures, emphasizing the sol-gel process as a cost-effective and environmentally friendly method to synthesize Si-based materials with distinctive geometries. Then examining the two primary metallothermic reduction pathways. Followed by an investigation into lithium-ion diffusion kinetics within 1-dimensional, porous Si architectures. Furthermore, the review accentuates strategies for commercializing Si materials, particularly focusing on the integration of carbon coatings and the co-utilization of graphite to balance the increased capacity with cycling stability.

An analysis of carbon coating techniques and graphite co-utilization revealed that these methods are essential for the commercial success of Si anodes. Building on this insight, these approaches will be applied in this dissertation to study the electrochemical performance using the methods established at Argonne National Laboratory [99].

From the literature review of Si anodes for LIBs, there are three key research gaps highlighted in the above text. This review provided a detailed examination of various fabrication techniques for 1-dimensional Si structures and assesses their respective advantages and limitations. A central goal is to identify a method that significantly lowers the initial industrial costs and employs safer, less toxic chemical processes. The investigation into the processes spotlighted the current capabilities of sol-gel synthesis for LIB applications. There is a research gap in the understanding of the key parameters within the sol-gel process that led to a high surface area and porous silica materials utilizing bio-templates, specifically CNCs. This dissertation aims to pioneer an environmentally friendly production of 1-dimensional Si structures from CNCs, to address the significant issue of volume expansion inherent to these materials. An essential part of this investigation involves examining the transformation of silica into elemental Si through metallothermic reduction. There is a research gap in heat dissipation strategies for magnesium reduction and how these strategies influence the morphological and compositional characteristics of the resulting Si-based products. This dissertation will conduct a comprehensive investigation into the structural and chemical properties of Si materials obtained through magnesiothermic reduction utilizing graphite as a heat sink due to their superior thermal diffusivity [100]. The goal of this study is to maintain the templated morphology from the sol-gel process. Furthermore, this study delves into evaluating the electrochemical performance of these Si materials, focusing on their integration in conventional battery architectures (i.e. graphite co-utilization). Lastly, an in-

depth understanding of lithium-ion kinetics within the novel Si structures produced in this dissertation is required due to the absence of an accurate electrochemical models for 1-dimensional, porous Si architectures. There is a research gap in the GITT modeling approach due to the absence of an electrochemical model that factors in material geometry, mechanical stress arising from volume alterations, and Si phase transformation. This comprehensive approach aims to enhance our understanding of Si-based materials' behavior in battery applications, ultimately improving their performance and sustainability.

Chapter Two : EXPERIMENTAL MATERIALS AND METHODS

2. Materials and Method

2.1. Experimental Materials

Cellulose nanocrystals (CNCs) in the form of 10 wt.% aqueous dispersion were kindly provided by the USDA Forest Products Laboratory (Madison, WI, USA). Absolute ethanol (200 proof, CAS Number 64-17-5, Fisher Chemical) was purchased from Fisher Scientific (Hampton, NH, USA). Hexadecyltrimethylammonium bromide (CTAB, CAS Number 57-09-0, ≥98%), tetraethyl orthosilicate (TEOS, CAS Number 78-10-4, ≥99%), lithium hexafluorophosphate ($LiPF_6$, CAS Number 21324-40-3, battery grade, ≥99.99%), lithium hydroxide (LiOH, CAS Number 1310-65-2, 98%), N-Methyl-2-pyrrolidone (NMP, CAS Number 872-50-4, ≥99.5%), fluoroethylene carbonate (FEC, CAS Number 114435-02-8, 99%), poly(acrylic acid) (PAA, CAS Number 9003-01-4, average M_w ~450,000), poly(vinylidene fluoride) (PVDF, CAS Number 24937-79-9), ethylene carbonate (EC, CAS Number 96-49-1, >99%), dimethyl carbonate (DMC, CAS Number 616-38-6, >99.9%), and a solution of 1M $LiPF_6$ in EC/diethyl carbonate (DEC) with EC:DEC volume ratio of 50:50 were purchased from Sigma Aldrich (St. Louis, MO, USA). Ammonium hydroxide (NH_3, CAS Number 1336-21-6, 28–30% ACS) was acquired from VWR International (Radnor, PA, USA). Magnesium powder (CAS Number 7439-95-4, 99+%, pure) was obtained from Acros Organics. Commercial Si (spherical, 100 nm, >97%), Carbon black (SuperP, CAS Number 1333-86-4) and Li chip (99.9% purity, 16-mm diameter, and 600-micron thickness) were acquired from MTI Corporation (Richmond, CA, USA). Mesocarbon microbeads (MCMB) synthetic graphite (spherical, 9-14 μm) was purchased from MSE Supplies (Tucson, AZ, USA). Lastly, multi-walled carbon nanotube buckypaper (60 GSM) was purchased from Nanotech Labs (Yadkinville, NC).

2.2. Experimental Methods

2.2.1. SilicaNQ Synthesis

The parameters governing the sol-gel process perform a pivotal role in manipulating the characteristics of the final products. Consequently, an exhaustive strategy was derived to meticulously scrutinize the influence of sol-gel parameters on the morphological evolution of SilicaNQ. The quantities of sol-gel parameters in this study are presented in Table 2.1. The standard procedure for our synthesis process initiates with the creation of an aqueous solution containing CNCs and water, which is sonicated to ensure uniform dispersion. A blend of deionized water, ethanol, ammonia, CNCs, and CTAB is prepared, and then subjected to 10 minutes of sonication to ensure a homogenous dispersion. Thereafter, the solution is kept under constant stirring at 350 rpm while TEOS is incrementally introduced through a syringe pump at a flow rate of 0.224 μL/min. Gentle stirring is maintained throughout the predetermined reaction time, during which a milky suspension begins to form in the solution. After the completion of the reaction period, the colloidal SilicaNQ products are separated from the liquid via vacuum filtration. Subsequently, the product undergoes a series of three washes with deionized water to ensure the elimination of any lingering reactants. The products are freeze-dried in a Labconco FreeZone unit at -84°C at 0.01 mbar to remove water from the products.

Table 2.1. The list of investigated sol-gel parameters

Sol-Gel Parameter	**Studied Values**	**Constant Parameters**
Ethanol content	0, 5, 10, 20, 30, and 40 vol.%	CNC: 0.02 wt% CTAB: 0.02 wt% Ammonia: 22.4 mol/L TEOS: 25.1 mmol/L

		Reaction time: 2 h
Ammonia content	2.8, 5.6, 11.2, 22.4, and 44.8 mol/L	CNC: 0.02 wt% CTAB: 0.02 wt% Ethanol: 20 vol.% TEOS: 25.1 mmol/L Reaction time: 2 h
CTAB content	0, 0.01, 0.02, and 0.04 wt%	CNC: 0.02 wt% Ethanol: 20 vol.% Ammonia: 22.4 mol/L TEOS: 25.1 mmol/L Reaction time: 2 h
Reaction time	0.5, 1, 2, and 4 hours	CNC: 0.02 wt% CTAB: 0.02 wt% Ethanol: 20 vol.% TEOS: 25.1 mmol/L Ammonia: 22.4 mol/L

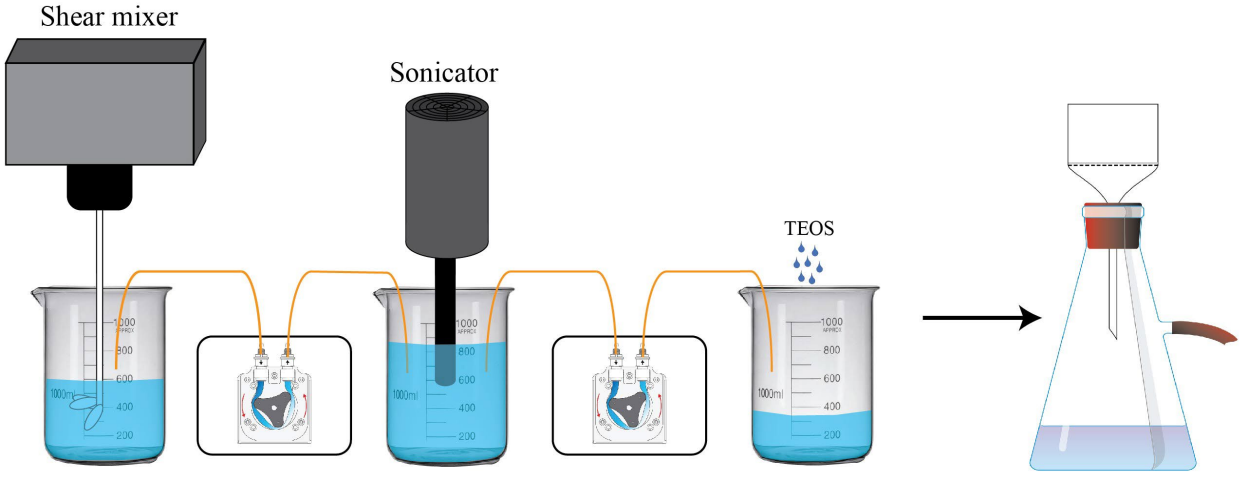

Figure 2.1. Schematic of scaled-up process for continuous synthesis of SilicaNQ.

The optimized formulation of sol-gel solution consists of deionized (DI) water (800 mL), ethanol (200 mL), ammonium hydroxide (4 mL), CNCs (200 mg, dry content), and CTAB (200 mg) to yield a 1L solution. The CNC and water dispersion requires sonication for five minutes prior to the addition of the remaining chemicals. The schematic showing the continuous synthesis process is shown in Figure 2.1. The resulting solution is first subjected to continuous stirring via shear mixer set at 350 rpm. Then a peristaltic pump will move the liquid solution to the beaker equipped with the sonicator. The sonication will commence when the beaker contains enough sol-gel solution to cover the sonicator tip. During the sonication, the next peristaltic pump will transport the solution to the final collection beaker. Both peristaltic pumps are operating at the same time moving liquid at a rate of 50 mL min^{-1} and constantly operating to ensure that the beakers in the setup do not overflow. This cycle continues seamlessly; when the shear mixer's beaker empties, it is immediately replenished with a fresh 1L batch of solution, maintaining a continuous operation. This method enables many 1L beakers of sol-gel solution to be produced, which will then follow the traditional method of TEOS introduction The final grown silicate-gel is collected via vacuum filtration which significantly speeds up the process compared to the previous centrifuge method. Moreover, we explored extending the reaction time beyond the initial two-hour limit to address constraints on batch size production. The previous TEOS amount of 1100 μL ensures sufficient TEOS in the system, but the reaction must be collected after 2 hours to stop the sol-gel reaction. To remove the 2-hour constraint, we produced silicate materials with 300, 400, 500, 600, 700, 900, and 1100 μL of TEOS, considering a 48-hour reaction time, while all other sol-gel parameters were kept constant.

2.2.2. Synthesis of SilicaNQ@C

To synthesize the carbon-coated SilicaNQ, the freeze-dried silicate-gel NQ underwent pyrolysis within an inert atmosphere, resulting in the conversion of CNCs into carbon. The freeze-dried silicate-gel NQ was positioned at the center of a tube furnace and subjected to a temperature of 600 °C at a ramp rate of 5°C/min for a span of 6 hours. Argon gas was introduced into the system 30 minutes before the onset of pyrolysis, at a flow rate of 200-300 sccm, and this flow was maintained throughout the pyrolysis process. The final product comprised a SilicaNQ framework incorporating carbon derived from the residual CNCs, and is denoted as SilicaNQ@C.

2.2.3. Synthesis of SiNQ

In an argon-filled glove box, SilicaNQ and magnesium powder are combined in a weight ratio of 1:0.8 (corresponding to a molar ratio of 1:2 silica to magnesium). This blend was then transferred to a cylindrical graphite crucible equipped with a screw-on lid. Electrical tape was employed to seal the crucible securely, inhibiting oxygen ingress into the system. Subsequently, the hermetically sealed reactor was positioned inside a tube furnace, and argon was flowed through the tube at a rate of 200 sccm for a duration of 30 minutes prior to initiating the heating process. The loaded crucible was then heated to 650 °C, with a ramp rate of 5 °C/min, for a total duration of 6 hours. During this time, the furnace tube was rotated to a complete 360 degrees every 30 minutes until the end of the run.

Due to the formation of Mg-based products, chemical etching is required. A 2M hydrochloric acid solution was employed to dissolve the magnesium oxide and silicide by-products. The material was introduced into the HCl solution, which was maintained under constant agitation for a duration of 48 hours. This was succeeded by multiple washes with deionized water until a neutral pH was achieved.

2.3. Characterization

2.3.1. Electrochemical Characterization

Electrode Preparation

Two types of electrodes were produced for electrochemical characterization: ion permeable bucky paper-based (comprising a mat of carbon nanotubes) and conventional copper foil-based. The bucky paper electrodes were produced utilizing SilicaNQ and SilicaNQ@C as the active materials. The slurry employed for the coating on the bucky paper was a combination of the active material, Super P serving as a conductor, and polyvinylidene fluoride (PVDF) as a binder. These components were combined in a weight ratio of 60:20:20, respectively, and were dispersed in N-methyl-2-pyrrolidone (NMP) solvent. The slurry was coated on the bucky paper substrates using a doctor blade coater achieving a mass loading of 1 $mg.cm^{-1}$.

The slurry for application on copper foil was formulated using a blend of MCMB graphite and SiNQ as the active materials, lithiated polyacrylic acid (LiPAA) as the binder, and Super P as the conductive agent. These components were combined in a precise weight ratio of 73:15:10:2, with water serving as the dispersion medium. The LiPAA was prepared by a dissolution of 5 wt.% of PAA in water, succeeded by a gradual addition of lithium hydroxide until the pH of the solution equilibrated at 7. The slurry was coated onto copper foil, targeting a cumulative active material mass loading of 3.5 $mg.cm^{-1}$.

Coin Cell Assembly and Testing

All electrode coatings are dried in a 100°C vacuum oven for 12 hours guaranteeing the complete elimination of solvent prior to battery fabrication. 2032-type coin cells are constructed in an argon-filled glove box with oxygen levels not exceeding 0.1 ppm. Each coin cell was

assembled in the following order: metal spacer, Lithium metal chip counter electrode, polypropylene separator (Celgard), 50 μL of electrolyte solution (1 M LiPF6 in ethylene carbonate/dimethyl carbonate (EC/DMC) in 1:1 ratio + 10 vol% fluoroethylene carbonate), Si-based electrode, metal spacer, and spring. All SilicaNQ bucky paper-based coin cells were subjected to a formation cycle of 0.05C followed by cycling at 0.1C (1C = 1965 mA g^{-1}) over the potential range of 0.01V – 1.0V at room temperature. The SiNQ and MBMB graphite copper foil-based coin cells were subjected to a formation cycle of 0.05C followed by cycling at 0.1C (1C = (0.73 x 370 mA g^{-1}) + (0.15 x 4200 mA g^{-1})) over the potential range of 0.005V – 1.5V at room temperature. The MCMB batteries were tested at a current rate of 370 mA g^{-1} for 1C. The SiNQ copper foil-based coin cells are subjected to cycling at a 0.1C current rate (with 1C defined as 4200 mA g^{-1}), operating within a voltage range of 0.01 - 1.0V.

Galvanostatic charge/discharge experiments were performed using an Arbin battery analyzer (LBT Series). Cyclic voltammetry measurements are performed on 17% c-Si/MCMB and 17% SiNQ-g/MCMB anodes at scan rates ranging from 0.1 to 2.0 mV s^{-1}. Electrochemical impedance spectroscopy evaluation is performed on 17% c-Si/MCMB and 17% SiNQ-g/MCMB anodes at room temperature over a frequency range of 100 kHz to 0.01 Hz. Cells were measured in the fully lithiated state (*i.e.*, 0.005 V) after the 5^{th} and 25^{th} cycles to ensure identical conditions. All CV and EIS experiments were carried out using a Gamry Reference 3000 potentiostat.

Galvanostatic intermittent titration technique (GITT) experiments were conducted using the Gamry Reference 3000 unit. Batteries, once freshly assembled, underwent a stabilization period of no less than 5 hours to attain an equilibrium voltage. Subsequently, the cells were subjected to a 30-minute current pulse, approximately ~200 mA g-1, succeeded by a 6-hour resting phase to allow the equilibrium potential to be established. This cycle of current pulses followed by

rest intervals was repeated until the defined voltage thresholds were met for Si-based anode batteries, employing cutoff voltages of 0.01 and 1.0 V.

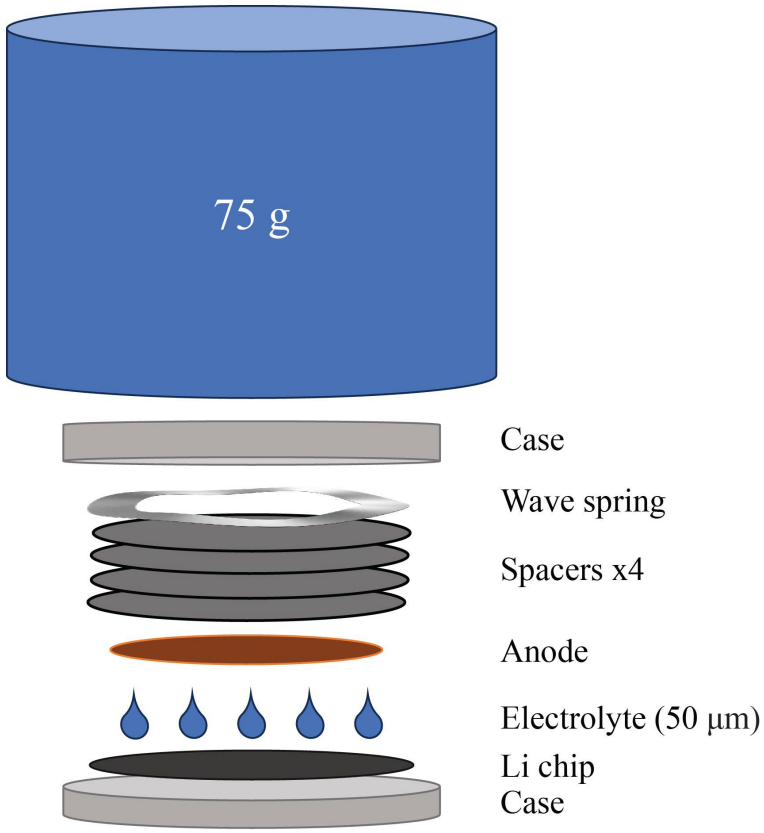

Figure 2.2. Schematic diagram of prelithiation technique used in our studies

Pre-lithiation was performed on 17% SiNQ-g/MCMB electrodes following the short-circuit electrochemical method reported by Bai *et al* [101]. Briefly, the 17% SiNQ-g/MCMB electrode was put under direct contact with a Li chip and soaked in 50 µL of electrolyte (1M $LiPF_6$ EC/DEC (50:50) and 10% FEC additive). The assembly (shown in Figure 2.2) was placed under ~5.5 kPa compressive pressure to secure optimal contact between the electrode and the Li chip. A range of pre-lithiation durations (*i.e.*, 0, 3, 5, 7, 10, and 15 min) were considered. After pre-lithiation, each electrode was paired with a fresh Li chip in the CR2032 coin cell with 50 µL of the same electrolyte and cycled between 1.5-0.005 V to evaluate the initial Coulombic efficiency.

2.3.2. Chemical

XPS data was collected using a PHI VersaProbe III with a monochromatic Al Kα X-ray source (hν = 1486.6 eV) and an Al anode powered at 25 W and 15 kV. The system was calibrated to both Ag and Au metallic binding energy. All data was calibrated to adventitious C 284.8 eV. The system base pressure was maintained at 1 x 10^{-6} Torr or better. Samples were prepared by pressing powders into a disc and then adhering samples to the platen using 3M double-sided tape. Analysis area was set to 500 x 500 μm^2 and a beam diameter of 100 μm. XPS survey data was collected using 3 sweeps, a pass energy of 224 eV, and a step size of 0.8 eV. High resolution spectra for C, O, and Si were collected at 45 degrees with 3 sweeps, a pass energy of 69 eV, and a step size of 0.125 eV. Argon etching was used for depth profiling of the samples. Peak fitting parameters were set for Si and Si oxides using a Shirley baseline with an FWHM of 1.2 and 2.1 eV, respectively. All peaks were fit with a G/L 60. All Si binding energies were constrained to 99.8 ± 0.25 eV. Si suboxide (SiO_x) peaks were identified at 101.2 ± 0.5 eV. Si dioxide (SiO_2) was constrained to 103.93 ± 0.25 eV. All peak fitting was done in Casa XPS.

Fourier-transform infrared (FTIR) spectroscopy was executed on solid specimens utilizing a ThermoFisher Nicolet iS50 spectrometer, featuring a diamond attenuated total reflectance (ATR) accessory. Raman spectroscopic measurements were applied to powder samples through a Renishaw inVia Raman microscope employing a 532 nm laser for excitation and a 10× objective for beam focusing. To ensure representativeness, a minimum of five spectra were acquired from distinct areas on each sample, with a 30-second integration time per spectrum, subsequently averaged for analysis. The determination of the specific surface area and total pore volume for the materials was carried out with a Quantachrome Autosorb iQ gas sorption analyzer, employing nitrogen gas.

To particle size distribution, solutions are initially passed through a 0.45 μm syringe filter and then left to stand until fully settled. Subsequently, the prepared solution is transferred into a pristine cuvette, which is then inserted into the Malvern Zetasizer Nano ZS for evaluation. Each sample undergoes three independent DLS measurements. For zeta potential measurements, the solution is introduced into a specialized capillary cell and loaded into the Malvern Zetasizer Nano ZS for analysis.

2.3.3. Thermal

Thermal gravimetric analysis (TGA) was conducted using a TA Instruments Q5000. 5-10 milligrams of material is placed onto the TGA pan and heated under air to measure the weight contribution from carbon. The furnace was programed to ramp at a rate of 5°C/min until it reached 700°C. Air was continuously purged through the sample chamber at a rate of 20 mL/min.

2.3.4. Microscopy

To evaluate the microstructure of silicate NQ, SilicaNQ and SiNQ products, transmission electron microscopy (TEM), scanning transmission electron microscopy (STEM), and scanning electron microscopy (SEM) employed. Specimens for TEM and STEM analysis were prepared by dispensing 10 μL of a diluted suspension of materials dispersed in DI water onto a copper TEM grid. STEM analysis was performed using a Hitachi SU9000 microscope with accelerating voltage of 30 kV. TEM analysis was performed using the Hitachi S9500 high-resolution microscope with an accelerating voltage of 300 kV. SEM analysis was performed using the Hitachi Regulus 8230 with an accelerating voltage ranging from 5 – 30 kV.

Transmission electron microscopy studies were carried out using a Hitachi T9500 high-resolution TEM at 300 kV with the selected area electron diffraction (SAED). Scanning TEM

examinations were conducted using a Hitachi SU9000 ultra-high-resolution SEM at 30 kV with energy-dispersive X-ray spectroscopy (EDS). Dimensional analysis of microstructural features in TEM or S-TEM images was performed using ImageJ software.

Chapter Three : CELLULOSE NANOCRYSTALS AS BIO-TEMPLATE FOR SILICA FORMATION*

3. Synopsis

Advancements in sol-gel technology have led to substantial progress in the development of mesoporous silica materials, which are characterized by their distinctive morphological features and customizable properties. These breakthroughs have broadened the range of potential applications of mesoporous silica, extending from biomedical technologies and water purification systems to rechargeable batteries [102,103]. The advent of dual-templating methodologies has further advanced the fabrication of mesoporous silica architectures, enabling the creation of sophisticated core-shell [104] and multi-shell [105] structures. The incorporation of biobased materials such as poplar catkin, [106] nanocellulose, [107] and chitosan [108] as sacrificial templates in sol-gel processing has introduced novel silica nanostructures that are intrinsically influenced by their biological origins. Among these bioderived species, cellulose nanocrystals (CNCs) are characterized by their one-dimensional (1D), needle-like morphology. They offer adaptable surface chemistry, non-toxicity, and rigidity [109]. It has been shown that under particular processing conditions (i.e., temperature, pH, surface charge, etc.), CNCs can self-assemble in aqueous solutions, resulting in the suspension of 3D networks composed of distinct, individualized CNC particles [110].

In this study, we leveraged this self-assembling behavior of CNCs and engineered a 3D mesoporous silica nanostructure resembling porcupine quills, leading us to call this porous Si dioxide product silica nano-quill (SilicaNQ). This highlights the synergy between biomimicry and advanced material synthesis in the pursuit of environmentally friendly and functional

* This work was supported by the US Endowment for Forestry and Communities [Contract No. 20–00082]

nanomaterials. The SilicaNQ material exhibits distinct porous tubular morphology, with the potential to reach an exceptional surface area and pore volume. However, a systematic analysis of sol-gel parameters, including co-solvent addition, catalyst concentration, templating strategy, precursor amount, and reaction time, is necessary to identify the optimal synthesis conditions. A significant element of this study is the introduction of a facile carbon coating technique via annealing the silicate gel (i.e., sol-gel product) under an inert atmosphere. Unlike conventional carbon coating processes that necessitate multiple steps, our strategy allows for the direct transformation of CNC templates into a conformal carbon coating on the surface of SilicaNQs to produce a SilicaNQ@C black powder. Following the synthesis and carbon coating stages, our investigation extends to a detailed evaluation of SilicaNQ and SilicaNQ@C materials. Ultimately, we present a case study that assesses the potential application of these unique materials in lithium-ion batteries (LIBs), showcasing the practical implications of our findings in energy storage applications.

3.1. Investigation of Sol-gel Parameters

Exploring the sol-gel parameters is crucial for obtaining defect-free, optimal silica structures. The sol-gel process, instrumental in generating silica from a silicate precursor in an aqueous medium, is principally governed by hydrolysis and condensation reactions, as elucidated by the subsequent chemical equations [102]:

Hydrolysis:

$$\equiv Si - OR + H_2O \rightarrow \equiv Si - OH + ROH \quad (3)$$

Alcohol Condensation:

$$\equiv Si - OH + RO - Si \equiv \rightarrow \equiv Si - O - Si + ROH \quad (4)$$

Water Condensation

$$\equiv Si - OH \; + \; HO - Si \equiv \; \rightarrow \; \equiv Si - O - Si \; + \; H_2O \qquad (5)$$

Hydrolysis initiates when the nucleophilic oxygen atoms in water molecules target and interact with the alkoxide (R: C_xH_y) groups in the silicate precursor [111]. The condensation reactions are categorized into alcohol and water condensation. Under most reaction conditions, the initiation of condensation hinges on the formation of siloxane bonds (Si–O–Si) [112]. Due to the hydrophobic nature of the silicate precursors, an alcohol is essential as the co-solvent to aid the dissolution and homogeneous distribution throughout the sol-gel medium [113]. Water plays a crucial role in the system, facilitating hydrolysis reactions and influencing the extent of these reactions, which subsequently affects the rate of condensation [111,114]. The presence of the catalyst not only accelerates the hydrolysis reactions, but also determines the reaction kinetics and particle interactions in the solution [112]. Following the hydrolysis and condensation stages, the inorganic polymerization of siloxane networks culminates in the creation of silicate gel.

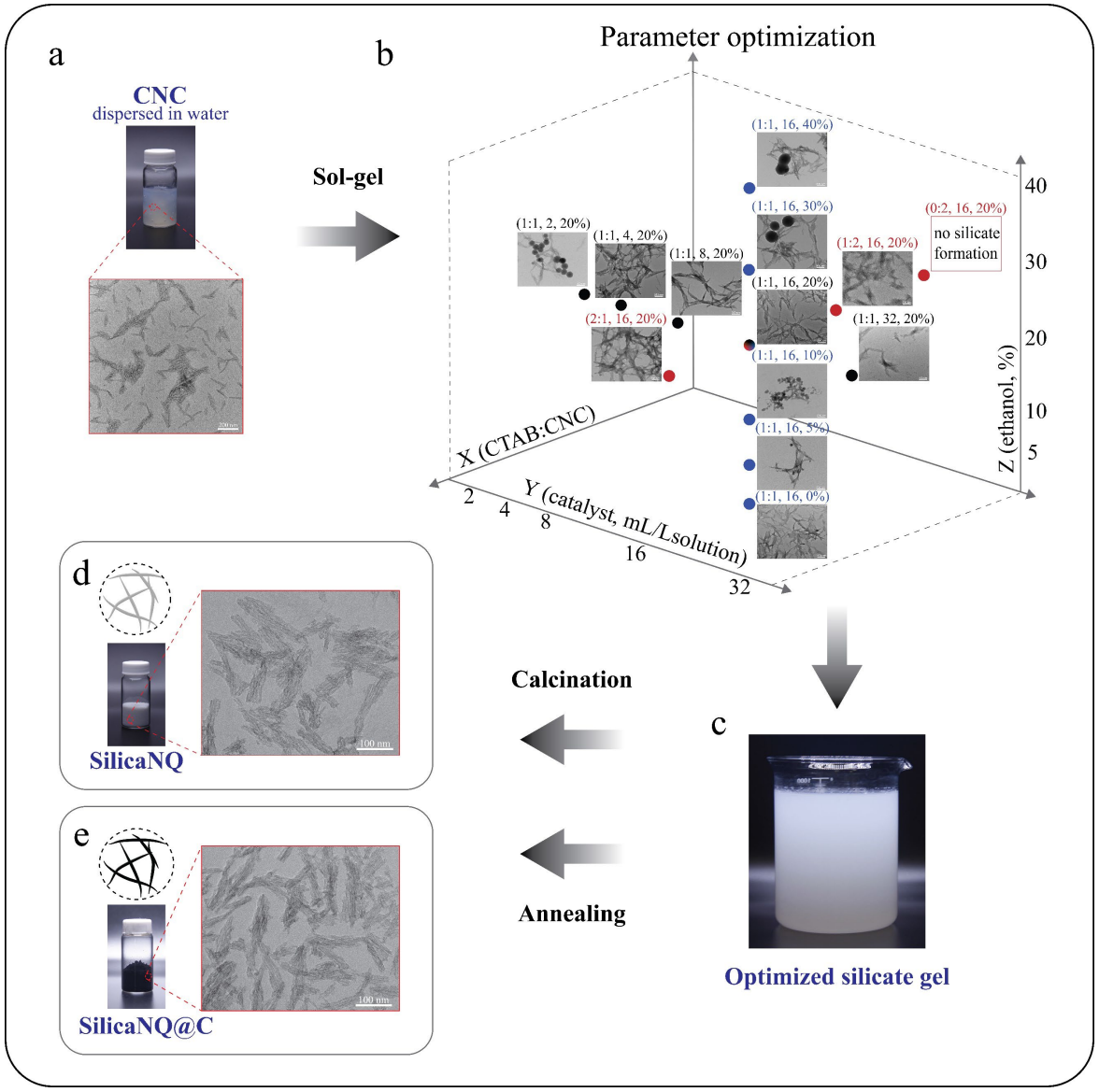

Figure 3.1. SilicaNQ process flow for the production of hollow and mesoporous silica nano-quills from CNCs beginning with the (a) stable suspension of 10 wt% CNCs in water, (b) parametric investigation of sol-gel variables impacting silica morphology, as evidenced by TEM micrographs, with the x-axis representing CTAB to CNC ratio, y-axis indicating catalyst amount, and z-axis detailing ethanol ratio, (c) optimized sol-gel solution containing grown silica-gel, (d) removal of CNC template via calcination to reveal the highly porous and hollow silica nano-quills, or (e) pyrolysis of CNCs for a facile carbon coating technique to form carbon coated silica nano-quills.

The preparation of silica-based materials using CNC templating approach in this study is outlined in Figure 3.1. Initially, CNCs (in the form of uniform dispersion in water, Figure 3.1a) are utilized to prepare a silicate gel. The sol-gel process involves introducing the silicate precursor (tetraethyl orthosilicate, TEOS) into a mixture, comprising of a solvent (DI water), co-solvent (ethanol), catalyst (NH_4OH), surfactant (Hexadecyltrimethylammonium bromide, CTAB), and CNCs. Proceeding the reaction, the silicate gel (Figure 3.1c) is collected, freeze dried and subsequently calcined to remove the templates and form a porous silica powder (Figure 3.1d), or alternatively annealed in an inert atmosphere for simultaneous silica formation and carbon coating (Figure 3.1e).

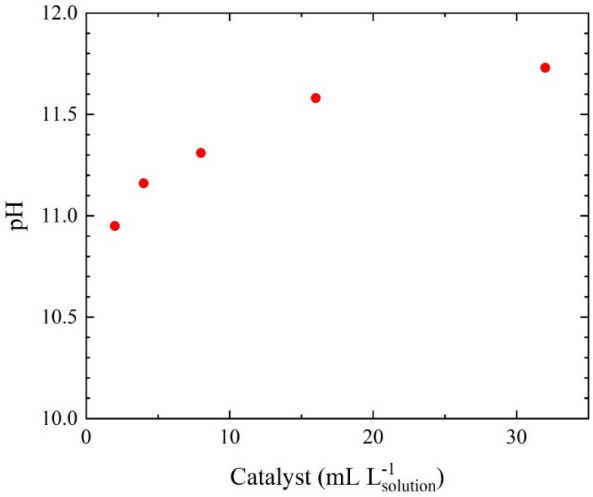

Figure 3.2. pH measurements of sol-gel solutions with varying concentrations 2, 4, 8, 16, and 32 mL $L^{-1}_{solution}$ of ammonium hydroxide catalyst.

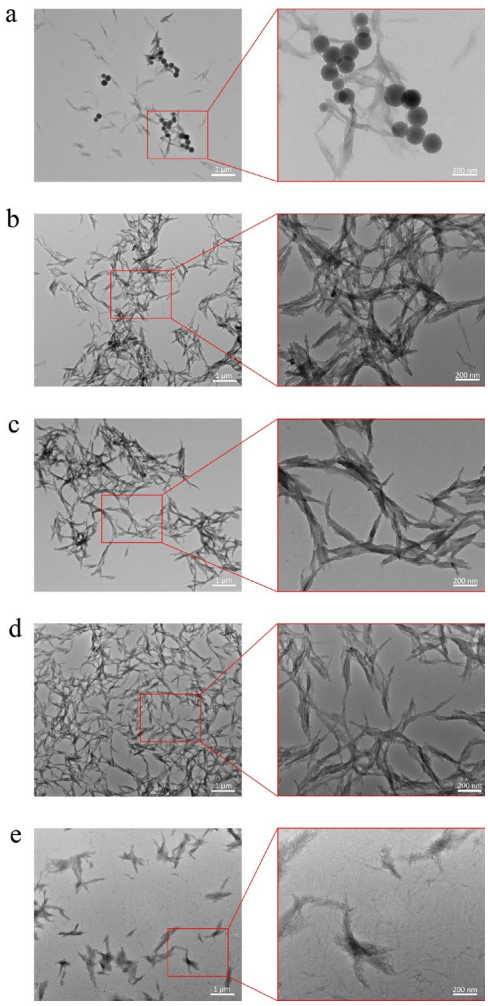

Figure 3.3. TEM micrographs illustrating the morphology of silicate-gel products synthesized at different catalyst concentrations: (a) 2, (b) 4, (c) 8, (d) 16, and (e) 32 mL $L^{-1}_{solution}$ of ammonium hydroxide (scale bar shows 1μm in low-magnification and 200nm in high magnification images).

We explored the role of three major parameters in the evolution of silicate gels: catalyst concentration, co-solvent addition, and surfactant-to-CNC ratio. A collective view of the effects of these three sol-gel parameters on the morphology of silicate gels is illustrated in Figure 3.1b. The catalyst content distinctively influences sol-gel reaction mechanisms [115]. When the catalyst concentration changes from 2 to 32 ml $L^{-1}_{Solution}$, the pH of water-ethanol-ammonia solution varies from 10.9 to 11.8 (Figure 3.2), with an apparent plateau forming at around 16 ml $L^{-1}_{Solution}$

concentration. With ammonia content of 2 ml $L^{-1}_{Solution}$, which is the least basic condition in this study, secondary spherical particles form within the silicate gel network (Figure 3.3a). As the ammonia concentration increases, particle aggregation diminishes in the silicate gel network and spherical particle growth is suppressed (Figure 3.3b-e). This phenomenon is linked to accelerated hydrolysis rates with higher catalyst. At ammonia concentration of 2 ml $L^{-1}_{Solution}$, slow hydrolysis fails to offset condensation rates, causing agglomeration and condensed species [112]. On the other hand, with excessive ammonia (32 ml $L^{-1}_{Solution}$) in the solution, the resulting gel is composed of many small silicate moieties, as seen in Figure 3.3e. Excessive catalyst brings more electron withdrawing groups (–OH) into the system, while condensation remains largely unaffected by the catalyst [116–118]. Consequently, a lower molecular weight gel product is expected to form.

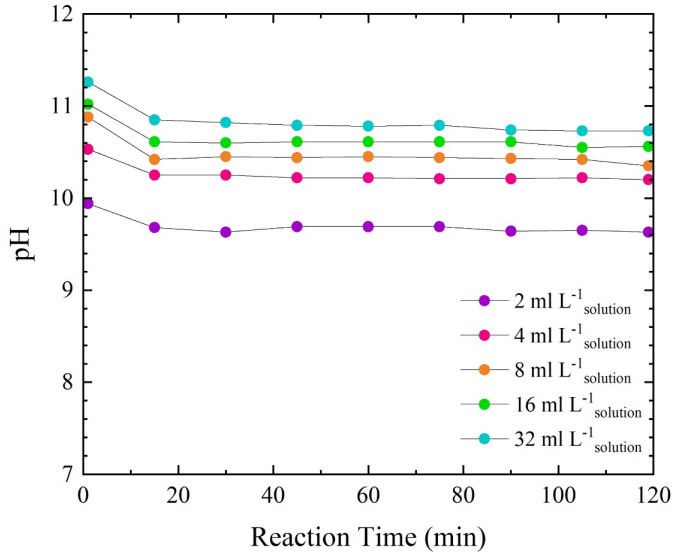

Figure 3.4. pH measurements over a 2-hour reaction period corresponding to catalyst content in Figure 6 showing 2, 4, 6, 8, 16, and 32 mL $L^{-1}_{solution}$.

In literature, catalytic reaction conditions are categorized by pH levels, where each region is distinguished by its dominating reaction mechanism [111]. The pH measurements of our water-ethanol-ammonia solutions reveal that the pH value consistently exceeds 10 throughout the 2-hour

reaction period Figure 3.4. Increasing the concentration of ammonia, as catalyst in our study, will increase the hydrolysis rate due to the increase in electron withdrawing groups (–OH), while the condensation of silanol groups are less affected by the presence of a catalyst [111,116,117,119]. The addition of ammonia leads to a faster interaction with silanol groups, however the condensation of hydrolyzed species are still slow, as defined by the following reactions [120]:

$$RO - Si(OH)_3 + OH^- \overset{fast}{\longleftrightarrow} RO - Si(OH)_2O^- + H_2O \quad (6)$$

$$RO - Si(OH)_3 + RO - Si(OH)_2O^- \overset{slow}{\longleftrightarrow} RO - Si(OH)_2 - O - Si(OH)_2OR + OH^- \quad (7)$$

With the increase in ammonia, the density of the silica surrounding the CNCs decrease as the network becomes more loosely structured. This is related to the redistribution reactions that occur in basic conditions, as described by the following [111]:

$$2\ dimers \underset{MeOH}{\overset{OH^-}{\leftrightarrows}} trimer + unhydrolyzed\ monomer \quad (8)$$

The bond breakage and reformation of siloxane groups leads to the continuous restructuring of polymers ultimately resulting in the trend we observe in Figure 3.3a-e.

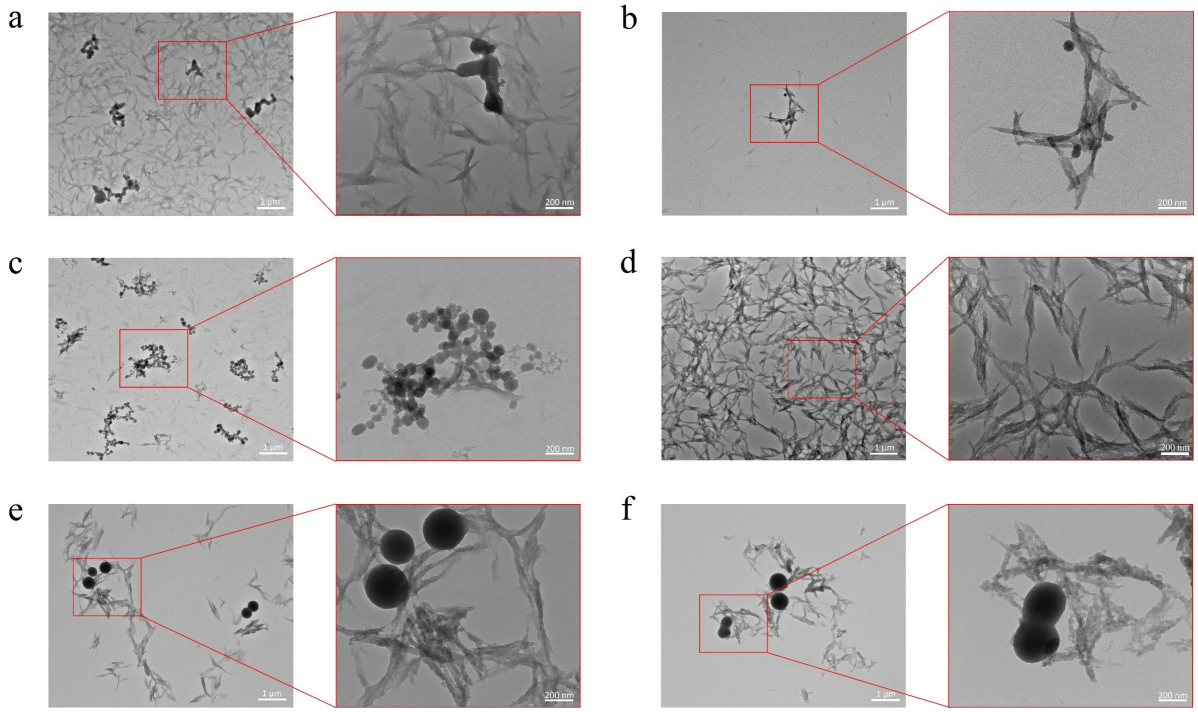

Figure 3.5. TEM micrographs of as-grown SilicaNQs with (a) 0 vol.%, (b) 5 vol.%, (c) 10 vol.%, (d) 20 vol.%, (e) 30 vol.%, and (f) 40 vol.% ethanol; other sol-gel parameters are constant (scale bar shows 1μm in low-magnification and 200nm in high magnification images).

When investigating the ethanol content during sol-gel reactions, there are two important factors to consider: the water/Si ratio and TEOS miscibility. Ethanol is required to homogenize the solution, otherwise TEOS would be insoluble in water leading to phase separation. At lower ethanol ratios, the structuring mechanism is largely affected by the miscibility of TEOS in the aqueous solution. Without any ethanol, TEOS forms immiscible clusters, giving rise to spherical secondary particles (Figure 3.5a). In scenarios where the ethanol concentration is insufficient to stabilize the TEOS emulsion, the instability of TEOS droplets within the emulsion system leads to the formation of solid silica spheres [113]. This indicates that 5 vol% (Figure 3.5b) and 10 vol% (Figure 3.5c) is still insufficient to solubilize the TEOS and suppress the growth of spherical particles. As the water/Si ratio decreases, the hydrolysis rate decreases. As a consequence,

unhydrolyzed precursor sites are incorporated into growing clusters resulting in a silica gel network with incomplete conversion of silanol and organosilane groups [111]. At ethanol concentrations of 30 vol.% (Figure 3.5e) and 40 vol.% (Figure 3.5f), the formation of micron-sized spherical particles within the silica structure is observed, indicating a decreased hydrolysis rate and a shift towards condensation reactions [111]. The increase in size of undesired particles with increasing ethanol content was also supported in the literature [121]. Ethanol's impact extends to silica arm morphology; 20 vol.% ethanol yields smooth surfaces (Figure 3.5d), whereas higher concentrations cause serrated textures (Figure 3.5f). Optimal conditions at 20 vol% ethanol avoid spherical silica growth, balancing TEOS miscibility and hydrolysis, key for achieving the targeted silica structure in our sol-gel approach.

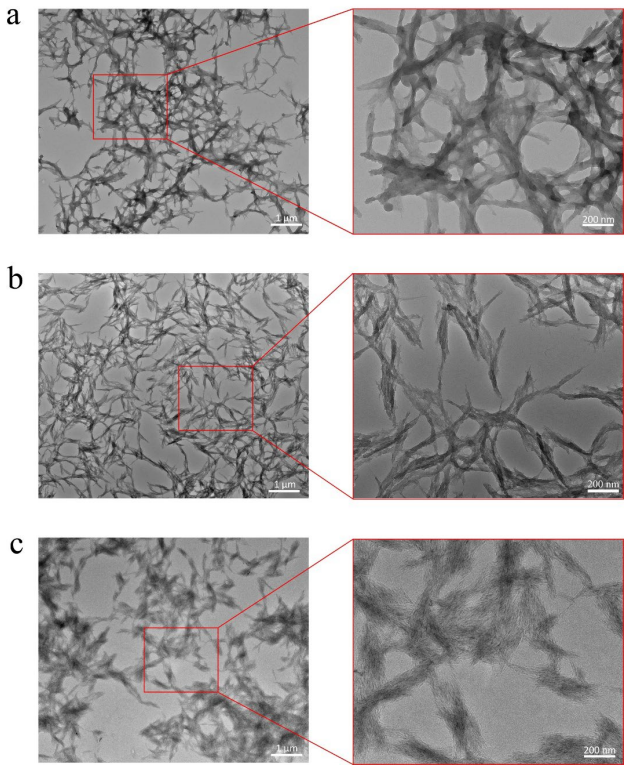

Figure 3.6. TEM micrographs illustrating the morphology of silicate-gel products synthesized with different CTAB to CNC ratios: (a) 2:1, (b) 1:1, and (c) 1:2 CTAB:CNC ratio in the sol-gel solution (scale bar shows 1μm in low-magnification and 200nm in high magnification images).

Surfactant interaction and packing in the aqueous solution is influenced by the surfactant concentration. The critical micelle concentration (CMC) is achieved when CTAB concentration is sufficient for its hydrophobic carbon chain to form a charge-matching environment enabling the cationic head (hydrophilic) to interact with water [122,123]. The surfactant micelles carry a positively charged surface thus also attracting anionic silanol species ($Si\text{-}O^-$). Under alkaline conditions (pH > 7) (Figure 3.2), the assembly of silicates with high negative charge density occurs through electrostatic interactions with cationic species [124]. Hence, the presence of CTAB within the system is essential, as evidenced by examining the ratio of CNC to CTAB (Figure 3.6). At a CTAB:CNC ratio of 2:1, the resulting silicate gel network exhibits a web-like morphology (Figure 3.6a), whereas a ratio of 1:2 leads to the formation of significantly more diffused particles (Figure 3.6c). The optimal CTAB:CNC ratio was established to be 1:1 (Figure 3.6b), favored for its capacity to generate a network of 1D silicate arms.

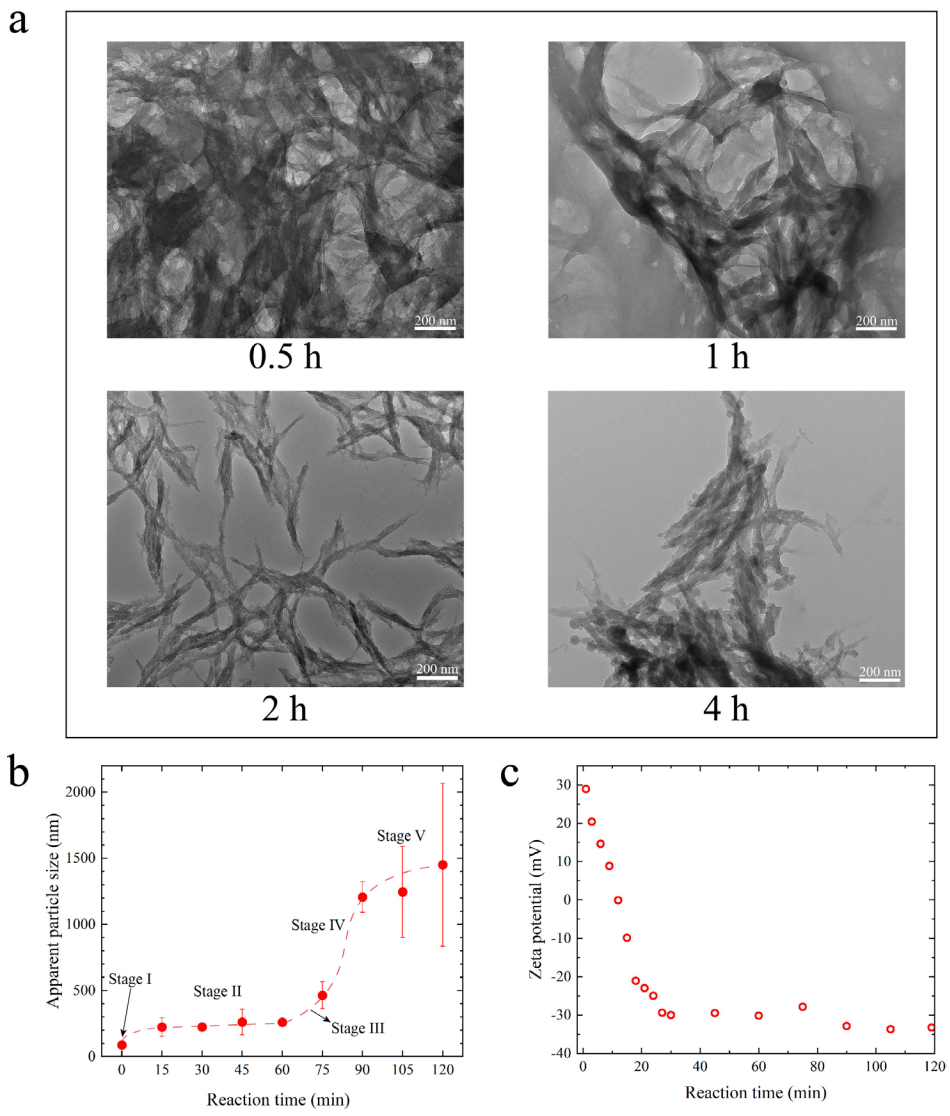

Figure 3.7. Morphological progression of silicate-gel observed over time intervals of (a) 0.5, 1, 2, and 4 hours, (b) silicate-gel particle size evolution over 2-hour reaction time, and (c) zeta potential measurements (scale bar shows 200nm).

During hydrolysis and condensation reactions, silicate evolution progresses sequentially from monomers to higher-ordered structures, eventually forming a densely packed silicate gel network that, in our case, is templated on the CNCs [118,125]. Moreover, alkaline sol-gel conditions tend to facilitate the aggregation of silicate species, a phenomenon detected through our

TEM imaging (Figure 3.7a) and corroborated by dynamic light scattering (DLS) (Figure 3.7b), which tracks silicate gel suspension size over time. After reacting for 0.5 hours, the dispersed silicate entities are predominantly comprised of lower molecular weight products from TEOS hydrolysis. With the progression of the reaction time, these silicate species continue to undergo condensation, resulting in the formation of more complex, higher-ordered silicate network. After 4 hours, the formation of secondary spherical particles and excess thickening of the silicate arms may suggest excess TEOS concentration, a hypothesis that will be examined later in the study. While rod-like structures cannot ascertain the particle length or cross-section by DLS, a hydrodynamic ‘‘apparent particle size’’ can be determined to qualitatively assess dispersion and track the relative state of aggregation if consistent materials and protocols are used [126]. Significantly, our measured apparent particle size prior to reaction (Figure S5b) is consistent with that reported for well-dispersed CNCs (~80 nm),[127] suggesting that any CTAB interaction has not adversely affected dispersion in the initial mixture. Our DLS results also align well with previously reported sol-gel growth stages [128]. The progression of sol-gel particle growth have been detailed previously and are categorized by their growth stages [128]. The early phase of the process involves dispersed colloidal particles, and their subsequent aggregation, as indicated by the horizontal plateau in the initial stages of the reaction (0 – 60 minutes). This phase, marked as stage I (colloidal particles) and stage II (particle aggregation), is then followed by a notable uptick in particle size, signifying stage III, where cluster growth occurs (60 – 75 minutes). The formation of the gel network is indicated by the sharp incline in the data signifying the progression of stage IV (75 – 90 minutes). Lastly, culminating in a plateau that marks stage V, the gel point (90 – 120 minutes). To understand the assembly process of silicate gel, Zeta potential measurements were conducted over time. Initially, the positive Zeta potential reflects the presence of CTAB micelles

with positively charged surfaces (Figure 3.7c). The extensive hydrolysis of TEOS forms anionic silanol species,[129] which is evident by a sharp drop of Zeta potential to negative values after 11 minutes of reaction. The Zeta potential then reaches a plateau at around -30 mV, indicating the stable suspension of surfactant-silicate composites [124]. A second plateau at Zeta potential of -35 mV is formed after 75 minutes of reaction, which coincides with *stage IV* of the particle growth.

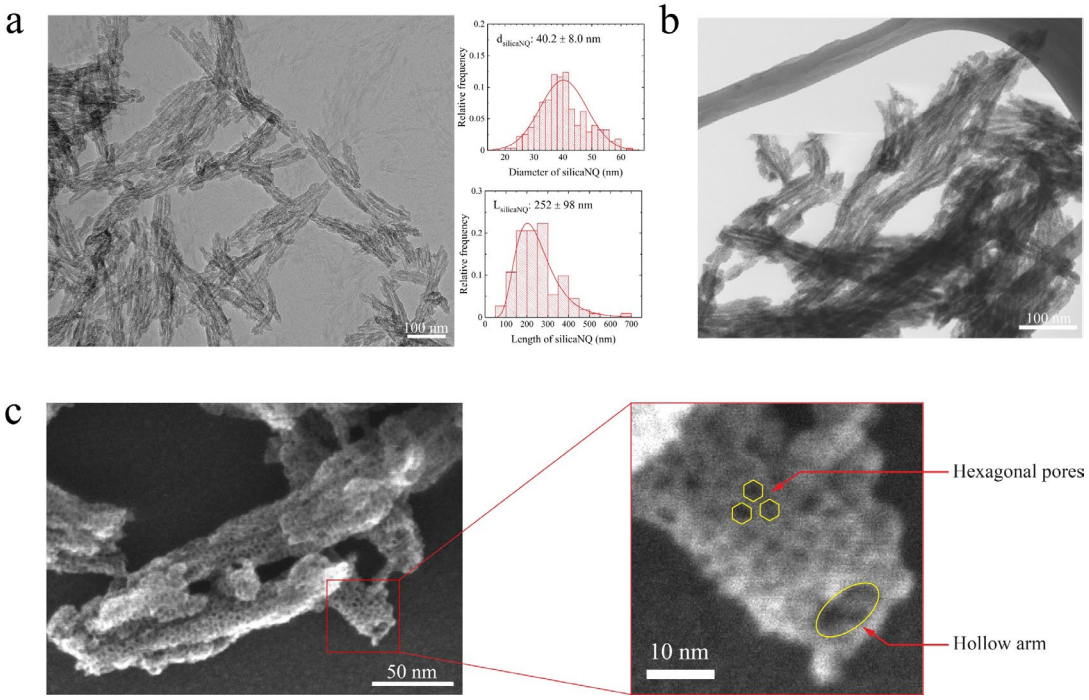

Figure 3.8. EM micrographs showcasing the optimal SilicaNQ morphology: (a) SilicaNQ products from calcination showing an average length of 252 nm and width of 40.2 nm, (b) bright-field S-TEM micrograph revealing the hollow channels within SilicaNQ network, and (c) an S-TEM micrograph showing the hexagonal pore features.

Through our parametric analysis, we determined that the most optimal sol-gel parameters results in a material morphology comprising of one-dimensional individualized structures within a three-dimensional network. This ideal configuration is achieved with the product formed from 20 vol% ethanol, 1 to 1 CTAB to CNC ratio, 16 ml $L^{-1}_{Solution}$ of catalyst, and 2 hour reaction time.

Following air calcination to remove the bio-template, the SilicaNQ particles display an average length of 252 nm and a width of 40.2 nm (Figure 3.8a). The distribution of particle lengths does not adhere to a normal Gaussian distribution, exhibiting a minor skew towards larger particle sizes. S-TEM imaging provided a more detailed view of the SilicaNQ structures. The bright-field S-TEM images highlight the hollow interior of the SilicaNQ, showcasing its continuous structure throughout the interconnected network (Figure 3.8b). High-resolution S-TEM imaging further unveils the surface characteristics of the SilicaNQs, revealing walls adorned with hexagonal-shaped pores (Figure 3.8c). Porosimetry analysis demonstrates that the SilicaNQ material features an exceptionally high BET surface area of 1265 $m^2 g^{-1}$, a total pore volume of 1.25 $cm^3 g^{-1}$ (Figure 3.9). This notable surface area and pore volume surpass those of commercially available mesoporous silica materials including SBA-15, MCM-41, MCM-48, and MSNR, as well as those derived from soft and bio-based templating methods, detailed in Table 3.1.

Table 3.1. Summary of mesoporous silica that are commercially available and also unique mesoporous silica utilizing bio-based template.

Template Material	**Morphology**	**BET ($m^2 g^{-1}$)**	**BJH ($cm^3 g^{-1}$)**	**Ref**
SilicaNQ	porous nanotube	1265	1.25	**This work**
SBA-15	mesoporous	605	0.49	[130]
MCM-41	mesoporous	995	0.75	[131]
MCM-48	mesoporous	1002	-	[132]
MSNR	mesoporous nanorod	907	0.82	[133]
Bacterial cellulose	nanotube	177.1	0.4	[134]
Citric acid	nanotube	40.85	-	[135]
Sodium bicarbonate	nanotube	44.46	-	
Phenolic resin	yolk-shell	736	1.79	[136]
SWCNT	nanotube	360	0.948	[137]
Chitosan	mesoporous	351	0.78	[138]
Nanocellulose	mesoporous	535	0.32	[139]
Manchurian ash	mesoporous	290.12	0.47	[140]
Mango lignin	mesoporous	286.77	0.45	

3.2. Facile One-step Carbon Coating

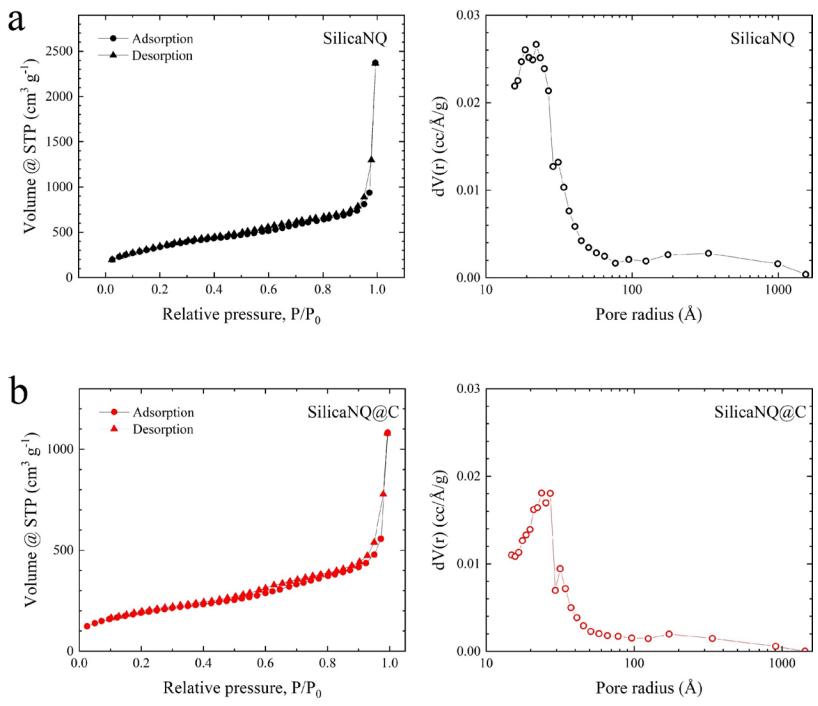

Figure 3.9. Nitrogen adsorption-desorption isotherms and pore size distribution of (a) SilicaNQ and (b) SilicaNQ@C.

Beyond removing the CNC template, it can be converted to carbon via pyrolysis, enabling a straightforward, single-step carbon coating process without the need for extra chemicals or synthesis stages. The pyrolyzed silica materials are referred to as SilicaNQ@C. Further comparative analysis was conducted on these two materials to distinguish their distinct physical attributes. The porous nature of calcined SilicaNQs was examined through nitrogen adsorption/desorption techniques (Figure 3.9). This analysis revealed that the optimized SilicaNQ material exhibits a BET surface area of 1265 m^2 g^{-1}, a total pore volume of 1.25 cm^3 g^{-1}. The pore size distribution of SilicaNQ (Figure 3.9a) is characterized by two peaks: a sharp peak with an average pore diameter of ~4.0 nm, which corresponds to hexagonal surface pores (as presented in Figure 3.8e) originated from CTAB micelles; and a broad peak with an average pore diameter of

18.9 nm, which is related to open tunnels from CNC template removal (Figure 3.8b). Pyrolyzed SilicaNQ@C revealed a BET surface area of 671 m^2 g^{-1}, a total pore volume of 0.74 cm^3 g^{-1}, and a bimodal pore distribution with pore sizes of 4.7 nm and 6.3 nm. Pyrolyzing the bio-template led to a reduction of almost 50% in the original BET surface area. S-TEM micrograph of SilicaNQ@C (Figure 3.10a) show the presence of carbon overlapping the regions where the silica is detected. TGA was performed in open air to burn off the organic content, revealing the presence of approximately 18 wt% carbon on the material (Figure 3.10b).

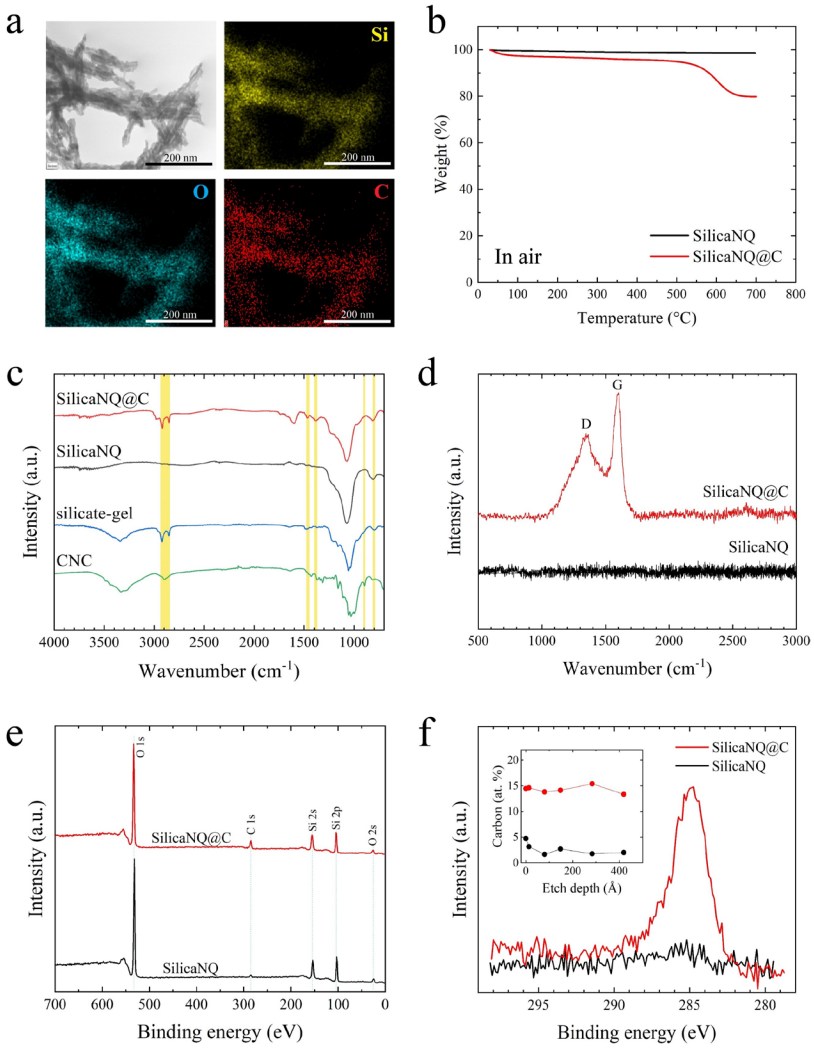

Figure 3.10. Elemental analysis of (a) SilicaNQ@C via EDS mapping. (b) TGA of SilicaNQ and SilicaNQ@C in open air, (c) FTIR spectra of CNCs, synthesized silicate-gel, SilicaNQ and SilicaNQ@C, (d) Raman spectroscopy, (e) XPS survey spectra of SilicaNQ and SilicaNQ@C, and (f) carbon XPS spectra and depth profiles of both materials.

Fourier-transform infrared (FTIR) spectra of Si-based materials in this study are shown in Figure 3.10c. The IR analysis of the silicate-gel reveals two salient peaks in the 2800 – 3000 cm^{-1} range, ascribed to aliphatic carbon groups from CTAB [141]. The IR spectra for CNCs contain a small peak around 885 cm^{-1} corresponding to the β-glycosidic linkage in the cellulose molecule [142]. This feature also appears as a small peak on the grown silicate-gel IR spectra. After calcination and pyrolysis, the β-glycosidic linkage peak has completely diminished. A distinctive broad peak, appearing at 1250 cm^{-1}, present for SilicaNQ and SilicaNQ@C is indicative of amorphous silica [143]. Both silica materials also exhibits the 1090 cm^{-1} peak for asymmetric Si–O–Si vibrations, while the symmetric counterpart of these vibrations is present at 795 cm^{-1} [144]. The two distinct peaks observed in SilicaNQ@C can be ascribed to C=C bond stretching, ranging from 1675-1500 cm^{-1} is associated with carbonized cellulose [145]. The Raman spectra of SilicaNQ@C (Figure 3.10d) reveal the characteristic D and G bands, indicative of the presence of amorphous carbon [146]. X-ray photoelectron spectroscopy (XPS) reveals a markedly higher surface concentration of carbon in the SilicaNQ@C material, as depicted in Figure 3.10e and f. Carbon analyses of both SilicaNQ and SilicaNQ@C predominantly show C-C and C-H bonds (284.8 eV), while the Si analysis for both samples indicates a surface composition chiefly of Si dioxide (103.5 eV). To assess changes in species and atomic concentrations, the samples underwent etching through the top 400 Å. This process demonstrated that SilicaNQ@C maintains a consistent carbon concentration of 14.3 at.% across the etched surface (Figure 3.10f, inset),

significantly higher than SilicaNQ's carbon concentration of about 2.2 at.%, where a considerable amount of carbon detected was adventitious carbon rapidly etched away. Despite no species changes detected in the carbon spectrum through either sample's depth, minor variations in Si suggest the existence of suboxides, though both samples primarily consisted of Si dioxide.

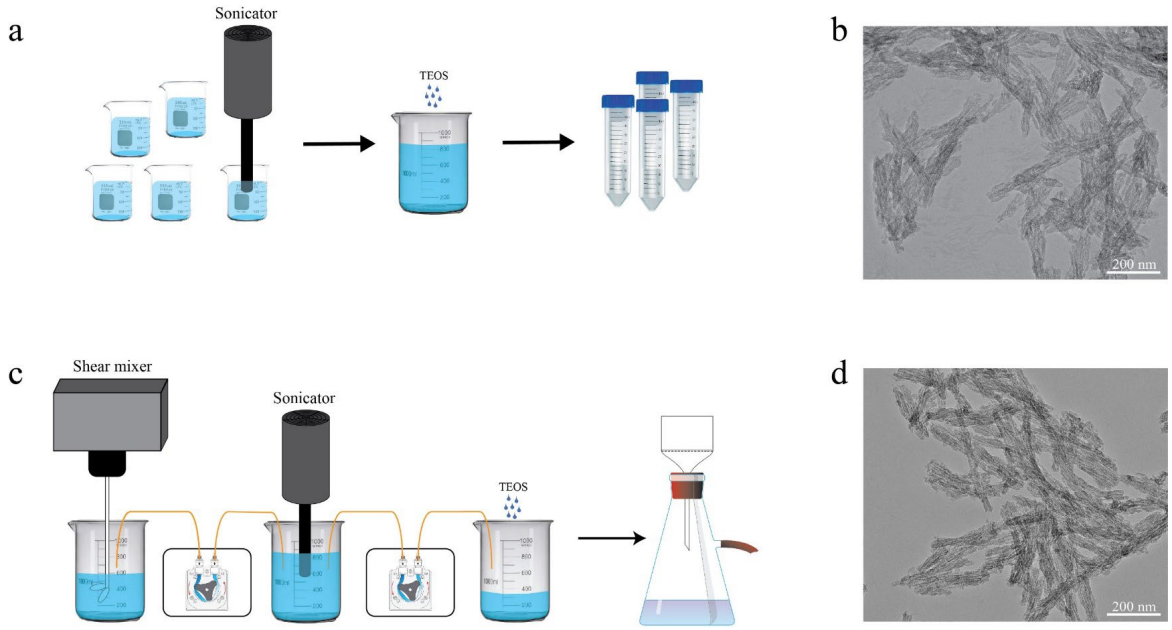

Figure 3.11. Schematic of (a) laboratory-scale setup of SilicaNQ production and (b) TEM micrograph of SilicaNQ products compared to schematic of (c) scaled-up setup of continuous SilicaNQ production process and resulting (d) TEM micrograph of resulting products (scale bar shows 200nm).

Until now, the synthesis of these unique materials has been limited to small quantity batches. Our objective was to explore the feasibility of scaling up the synthesis process while preserving their unique morphology. Through extensive experimentation, the most effective method for large-scale production was identified. The optimal setup for scaling up (Figure 3.11d) begins with the shear mixing of the prepared sol-gel solution, which is then pumped through a sonication stage and subsequently directed to the final collection station. The small-scale synthesis (Figure 3.11a)

previously yielded around 200 mg of material per trial. Post-scaling, the production increased significantly, enabling the generation of several grams per trial as the scaled-up process facilitates continuous fabrication. To verify the preservation of the unique silica morphology during the scale-up, the produced materials were examined under TEM, where the SilicaNQ morphology produced from the large-scale production (Figure 3.11d) is comparable to the product from lab-scale (Figure 3.11b). Another challenge faced in scaling up involves the 2-hour reaction time. This duration posed homogeneity issues in larger batches, given the constraints of the TEOS feed rate into the system. To optimize the reaction process for larger scale production, extended reaction times of approximately 48 hours were explored. The objective was to ensure complete hydrolysis and condensation reactions for the silicate precursor. To accommodate these prolonged reaction durations, the quantity of TEOS was carefully adjusted to avoid excessive amounts in the system. Varying volumes of TEOS—300, 400, 500, 600, 700, 900, and 1100 μL—were analyzed over a 48-hour period. Statistical analysis was then conducted on the resulting structures to precisely measure the width of the silica particles (c). The materials investigated via TEM that facilitated the statistical measurements exhibit the nano-quill-like structure, characteristic of the original morphology (Figure 3.12a and b). The particle width of the silica exhibits a distinct trend, progressively increasing with the amount of TEOS used. From 300 to 600 μL of TEOS, there's a gradual increase in particle width, ranging from 21 to 23.5 nm. A notable spike occurs at 700 μL, where the width jumps to 26 nm, eventually stabilizing around 32 nm for the higher TEOS concentrations. In addition, nitrogen adsorption desorption isotherm was employed to investigate the BET surface area (Figure 3.12d) and the total BJH pore volume (Figure 3.12e). Both surface area and pore volume displayed a similar pattern, peaking at 300 μL and diminishing at 900 μL.

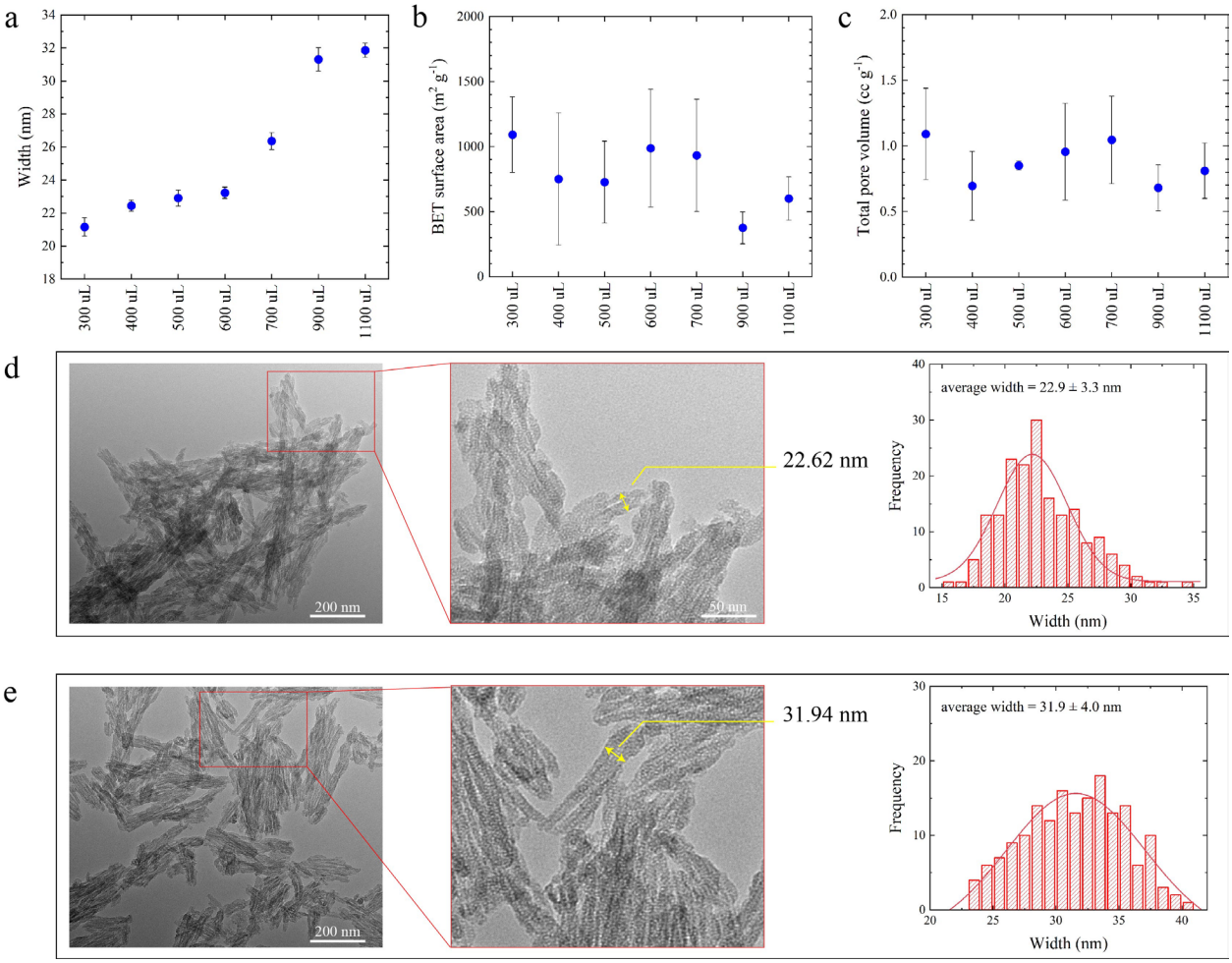

Figure 3.12. Structural characteristics of SilicaNQ products from continuous process and 48 hours of reaction: (a) particle width, (b) BET surface area, (c) BJH total pore volume. TEM micrographs of SilicaNQs after introducing (d) 500 µL and (b) 900 µL of TEOS into the continuous production process (scale bar shows 200nm in low-magnification and 50nm in high magnification images).

3.3. Electrochemical Performance of Silica and SilicaNQ@C

In the lithium-ion battery (LIB) sector, the quest for enhanced anode energy density is critical, driven by the surging global demand for LIBs in electric vehicles. Our unique silica structures, born from CNC templating, emerge as potential game-changers for LIB anodes. Silica-

based anodes, characterized by a higher theoretical capacity (1965 mAh g^{-1}) in comparison to traditional graphite anodes, face challenges associated with volume expansion, approximately 160% [147]. In this context, SilicaNQs, distinguished by their unique hollow and porous architecture, provide an innovative solution. These structures offer ample free space to accommodate material expansion during lithiation, potentially addressing a critical limitation in silica-based anode materials.

In this case study, we delved into the potential applications of materials developed in our research. Buckypaper, selected as the current collector for its three-dimensional structure, which facilitates the absorption of the wet slurry, enabling higher mass loadings compared to conventional Cu foil collectors [148]. The electrochemical impedance spectroscopy (EIS) profiles of both materials were examined after the 5th, 10th, and 25th cycles to identify electrochemical performance variations (Figure 3.13a and b). For all examined cycles, the SilicaNQ@C anode exhibits a smaller series resistance (R_S) compared to the SilicaNQ anode. Furthermore, a smaller charge-transfer resistance (R_{CT}) is detected for the SilicaNQ@C anode, likely due to the presence of conductive carbon coating (from CNC annealing) and suggests an improved lithium-ion mobility after successive cycles [149].

The long-term cycling performance of batteries with calcined SilicaNQs and SilicaNQ@C were assesed, and the results are presented in Figure 3.13e. The battery with SilicaNQ provided a high initial reversible capacity of 0.565 mAh cm^{-1}, which gradually increased to 0.748 mAh cm^{-1} after 200 cycles, a ~33% increase. The battery with SilicaNQ@C provided a high initial reversible capacity of 0.797 mAh cm^{-1}, which gradually increases and peaks at 1.292 mAh cm^{-1}, a ~55% increase before a gradual decrease and stabilizing around 1.015 mAh cm^{-1}. This characteristic behavior observed in SiO_X batteries is the 'capacity climbing' phenomenon. The lithiation reaction

of SiO_2 triggers the formation of electrochemically active Si out of the original material through the following reactions [150]:

$$SiO_2 + 4Li \rightarrow Si + 2Li_2O \quad (9)$$

$$2SiO_2 + 4Li \rightarrow Si + Li_4SiO_4 \quad (10)$$

This phenomenon is observed mainly in the initial cycles as the capacity-voltage curves demonstrate the consistency in capacity values between the 100th and 200th cycles, indicating minimal change over these cycles (Figure 3.13c and d). A pivotal breakthrough of our approach is the streamlined one-step carbon coating process, which significantly elevates the specific capacity, underscoring the effectiveness in enhancing battery performance.

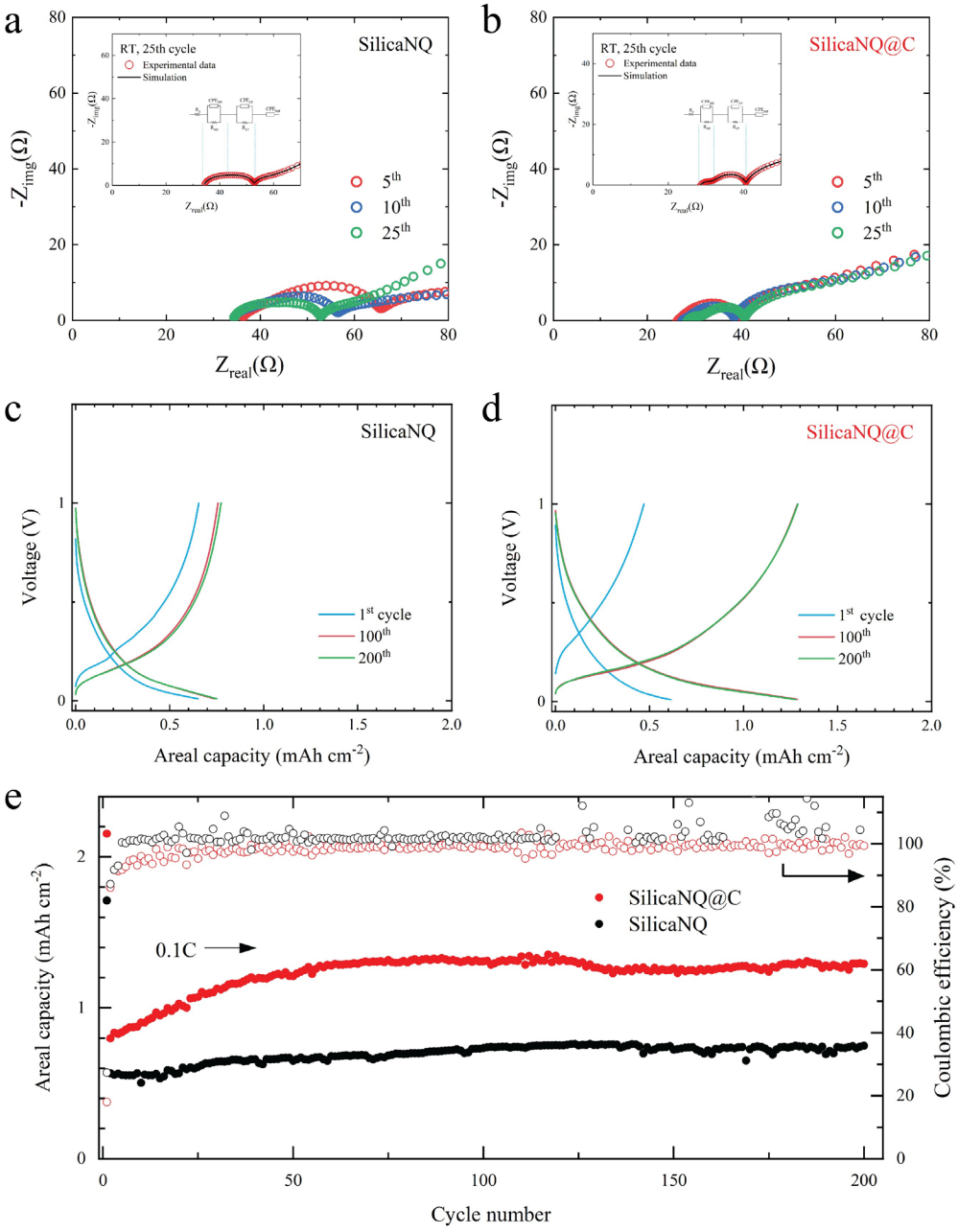

Figure 3.13. Nyquist plot of (a) SilicaNQ and (b) SilicaNQ@C electrodes after 5th, 10th, and 25th cycle. Electrochemical performance of SilicaNQ-based electrodes: charge-discharge profiles of (a) SilicaNQ and (b) SilicaNQ@C, and (c) cycling performance of SilicaNQ-based anodes. All SilicaNQ-based half cells were cycled between 1.0 and 0.01 V (1C = 200 mA g^{-1}).

Chapter Four : MAGNESIOTHERMIC REDUCTION FOR FORMATION OF SI-BASED MATERIALS[†‡§]

4. Synopsis

The sol-gel method of synthesizing silica materials offers a pathway for creating specifically templated silica architectures. To enhance electrochemical performance, our objective is to transform the silica into Si, as Si boasts a markedly higher theoretical capacity of 3600 mAh g^{-1}, in contrast to silica's 1965 mAh g^{-1}. Metallothermic reduction presents a feasible pathway for the transformation of SiO_2 to elemental Si [14]. There is an array of burgeoning alternatives for metallothermic reduction, such as carbon, aluminum, and magnesium. Nevertheless, each approach has its own set of benefits and drawbacks. For instance, carbothermic reduction necessitates extremely elevated temperatures (in excess of 1800°C), which would obliterate the templated morphology.

Aluminum and magnesium have garnered attention as the most promising candidates for the metallothermic reduction of silica to Si, due to their proficiency at comparatively lower temperatures. Comparative studies have been to analyze these two approaches [53]; nevertheless, the findings indicate that aluminothermic reduction remains inferior to magnesiothermic reduction in respect to both the yield of Si conversion and the surface area of the final materials.

[†] Chen, N.; Sabet, M.; Sapkota, N.; Parekh, M.; Chiluwal, S.; Koehler, K.; Clemons, C.; Ding, Y.; Rao, A. M.; Pilla, S. Bioderived Silicon Nano-Quills: Synthesis, Structure and Performance in Lithium-Ion Battery Anodes. *Green Chem.* **2024**. https://doi.org/10.1039/D4GC00498A

[‡] This work was supported by the US Endowment for Forestry and Communities [Contract No. 20–00082]

[§] The authors also acknowledge financial support through Clemson University's Virtual Prototyping of Autonomy Enabled Ground Systems (VIPR-GS), under Cooperative Agreement W56HZV-21-2-0001 with the US Army DEVCOM Ground Vehicle Systems Center (GVSC)

Using commercial Si products in LIB anodes poses several technical challenges, specifically the significant volume changes of Si during (de)lithiation [151], which can result in loss of electrical contact and capacity fade over the operational lifetime. To mitigate the volume change issue, Si nanostructures with several morphologies have been proposed, among which 1D tubular structure is proven to effectively mitigate mechanical failure by relieving mechanical stresses in the material [84,152–154]. Moreover, pore generation can enhance Li-ion (Li^+) diffusion through Si structure and improve its charge storage capabilities [155,156]. However, the synthesis methods commonly employed for fabricating porous tubular Si nanostructures frequently use hazardous chemicals, demand considerable financial investment, and give rise to safety issues [157,158]. This motivates our investigation into the use of templated hollow and porous SilicaNQ as a basis for Si conversion, to assess the preservation of the structure during this process.

In this study, employing the SilicaNQ materials synthesized as detailed in Chapter 3, the objective is to convert these templated structures to Si while preserving the original morphology to the greatest extent possible. To address the challenges posed by the exothermic nature of the metallothermic reduction process, various heat scavenging materials will be utilized with the aim of absorbing the excess heat generated during the reaction. This is pivotal for maintaining the structural integrity of the templated silica materials. In this segment of the study, the focus is on investigating the optimal container for housing the silica materials during the conversion process. Two types of crucibles, alumina oxide and graphite, will be employed. It is noteworthy that the graphite crucible boasts a thermal diffusivity that is 10x higher than its alumina counterpart, shown in Figure 4.1a and b [100,159]. Following the conversion process, comprehensive characterization will be undertaken to elucidate the structural and chemical variations between the samples prepared using different crucibles. Subsequently, an assessment of the electrochemical

performance of the resulting materials will be conducted to understand the implications of the choice of crucible on the practical applications of these materials.

One of the defining attributes of SiNQs is their water dispersibility, enabling the use of water-based slurries in lieu of the standard N-Methyl-2-pyrrolidone (NMP)-based mixtures, which are necessary for conventional Si-based slurry compositions due to the hydrophobic nature of commercial Si (c-Si). Notably, NMP introduces undesirable occupational and environmental challenges, encompassing risks of human exposure, reproductive toxicity, and consequentially rigorous EU regulations [160]. Leveraging water-dispersible materials mitigates these risks and presents potential economic advantages by lowering production costs due to diminished hazardous waste management requirements.

4.1. Si Products Formed from Mg Reduction

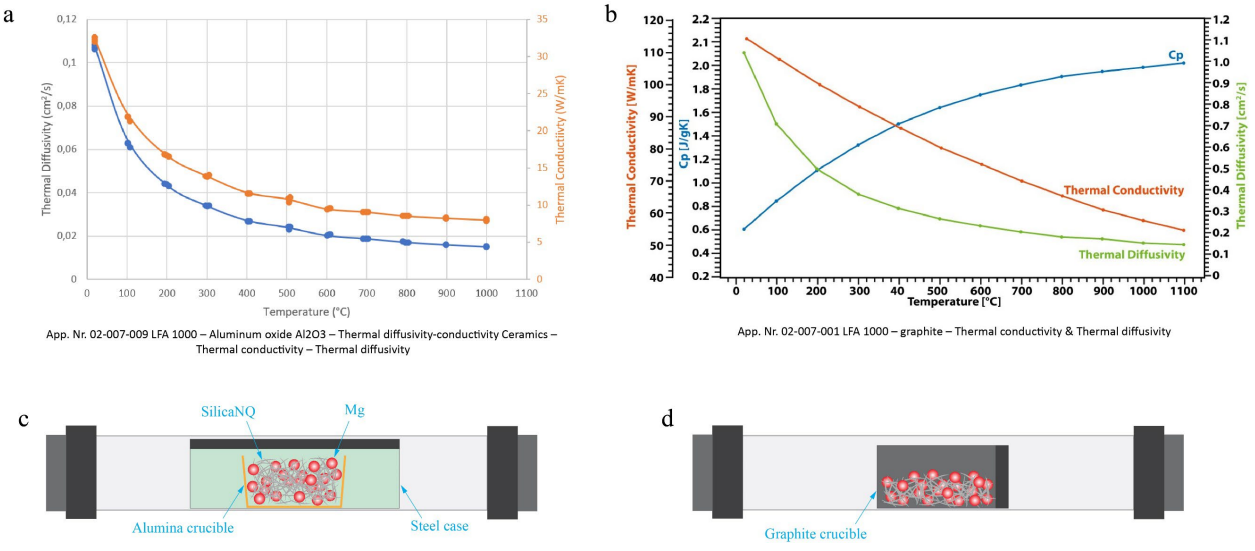

Figure 4.1. Thermal diffusivity of (a) graphite and (b) alumina as a function of temperature (reproduced with permission from Linseis) [100,159]. *Schematic setup for magnesiothermic reduction of SilicaNQ using (c) an alumina boat and (d) a cylindrical graphite crucible.*

Magnesiothermic reduction was used to convert silica to Si. Upon exposure to gaseous magnesium (Mg) and diffusion of Mg molecules into the surface of silica particles, elemental Si and Mg byproducts are formed. Subsequently, the solid state diffusion process enables the transportation of Mg deeper into the material, thus leading to the following chemical reactions throughout the material [161]:

$$Si(s) + 2Mg(g) \rightarrow Mg_2Si(s) \quad (11)$$

$$Mg_2Si(s) + SiO_2(s) \rightarrow 2MgO(s) + 2Si(s) \quad (12)$$

Magnesiothermic reduction generally proceeds as an exothermic reaction, where Si is formed progressively from the surface to the core [162]. The heat generated during this process can lead to significant temperature increases, potentially causing local melting and distortion of the Si product [161]. It is a standard approach in scientific studies to perform magnesiothermic reduction within ceramic crucibles, which are characterized by their low thermal diffusivity at elevated temperatures. For example, the thermal diffusivity of alumina at 650 °C is ~0.02 $cm^2\ s^{-1}$ [159]. At the same temperature, the thermal diffusivity of graphite is ~0.2 $cm^2\ S^{-1}$ [100]. The significantly higher thermal diffusivity of graphite makes it a better crucible for dissipating the heat generated during reduction reactions. To verify this, we conducted SilicaNQ reductions in both alumina boat crucible loaded into an airtight steel container, and a graphite cylindrical crucible with airtight screw on lid, shown in Figure 4.1c and d.
The powders, after reduction, underwent a mild hydrochloric acid treatment to eliminate magnesium-related byproducts, yielding the final SiNQ product. Consequently, the SiNQ variant produced in an alumina crucible and subsequently purified with HCl is denoted as SiNQ-a, whereas the SiNQ product derived from a graphite crucible and treated with HCl is labeled SiNQ-g.

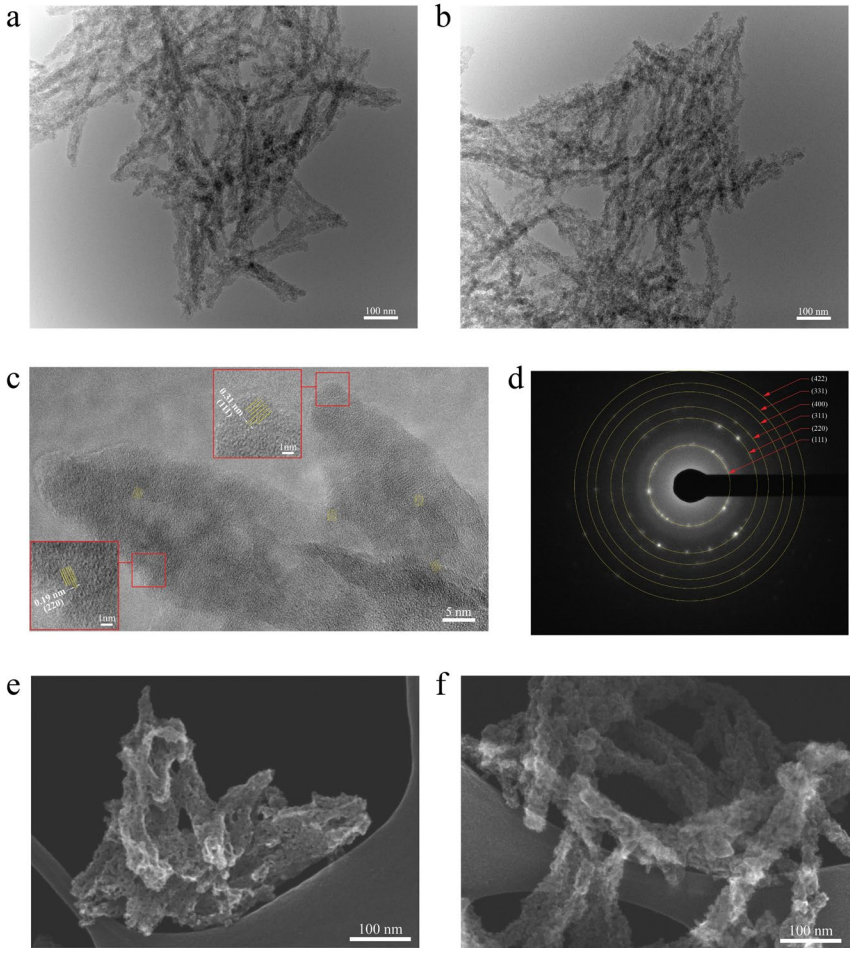

Figure 4.2. Electron microscopic studies of SiNQs; (a) TEM micrographs of SiNQ-a, (b) TEM micrographs of SiNQ-g (scale bar shows 100nm), (c) high-resolution TEM micrograph of SiNQ arms revealing crystalline pockets distributed in an amorphous matrix (scale bar shows 50nm), (d) electron diffraction patterns show the presence of major crystal systems of elemental Si in the structure of SiNQ material, (e) STEM micrographs of SiNQ-a, and (f) STEM micrographs of SiNQ-g surface features (scale bar shows 100nm).

The microstructural characteristics of SiNQ materials were studied to identify the effects of heat accumulation during the reduction process. The TEM micrographs of SiNQ-a and SiNQ-g are presented in Figure 4.2a and b. The 1D morphology of SilicaNQ arms was conserved after reduction in both crucibles. An in depth view of surface morphology (Figure 4.2e and f) reveals

that both materials are porous. However, SiNQ-a arms appear more flattened and fused together, in contrast to SiNQ-g arms, which maintained an individualized tubular geometry with less fusing. Gas physisorption measurements were performed on both SiNQ materials, and the results are presented in Figure 4.3. Previously reported, the SilicaNQ material has a BET specific surface area of 1266 $m^2 g^{-1}$, with a BJH total pore volume of 1.25 $cm^3 g^{-1}$. The adsorption-desorption isotherms show an apparent hysteresis (Figure 3.9), indicating the existence of mesopores in the material structure [163]. After reduction to SiNQ-a, the surface area and total pore volume decreased to 232 $m^2 g^{-1}$ and 0.42 $cm^3 g^{-1}$, respectively. While the surface area and total pore volume of SiNQ-g material were measured to be 400 $m^2 g^{-1}$ and 0.64 $cm^3 g^{-1}$, respectively. The lower surface area and pore volume of SiNQ-a, compared to SiNQ-g, implies a considerable fusion and distortion of the material during reduction in the alumina crucible. Hysteresis is present in isotherms of SiNQ-a (Figure 4.3a) and SiNQ-g (Figure 4.3c), implying that mesopores are preserved during the reduction of SilicaNQ using either crucible. However, multiple peaks with pore diameter of <10 nm appear in their pore size distribution graph (see Figure 4.3b and d). For example, SiNQ-a shows mesopores with diameters of 3.5, 4.4, 6.3, and 7.5 nm, and SiNQ-g has mesopores of 3.7, 4.5, 5.8, and 9.0 nm. Although SiNQs maintain surface mesopores, these results show that the geometry of surface pores was altered during SilicaNQ reduction. In addition, we identified a peak with a pore diameter of >20 nm from BJH pore size analysis of SiNQs. This peak, with an average diameter of ~25 nm, corresponds to the presence of a hollow core within SiNQ arms. The presence of a hollow interior, along with mesopores on the surface, is designed to mitigate volume fluctuations during the lithiation and delithiation cycles. We hypothesized that the morphological variances between SiNQ-a and SiNQ-g materials will influence their capacity for charge storage during interactions with lithium ions.

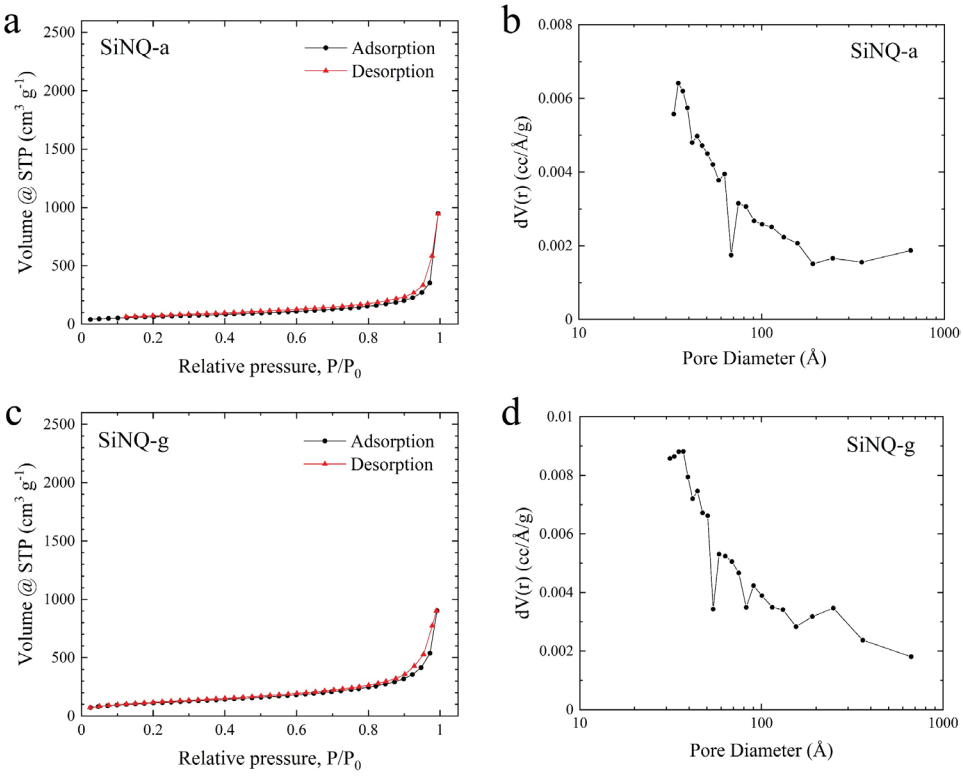

Figure 4.3. BET surface area and BJH pore volume of (a, b) SiNQ-a, and (c, d) SiNQ-g.

High-resolution TEM of SiNQs was performed to reveal the material's phase composition after thermal reduction. The resulting structure is characterized by randomly distributed crystalline pockets in an amorphous matrix, as shown in Figure 4.2c. Majority of crystalline pockets show interplanar spacing of 0.31 nm and 0.19 nm. The former corresponds to Si(111) planes, and the latter corresponds to Si(220) planes [164]. Moreover, electron diffraction patterns of SiNQs (see Figure 4.2d) reveal the presence of other Si crystal planes, including (311), (400), (331), and (422).

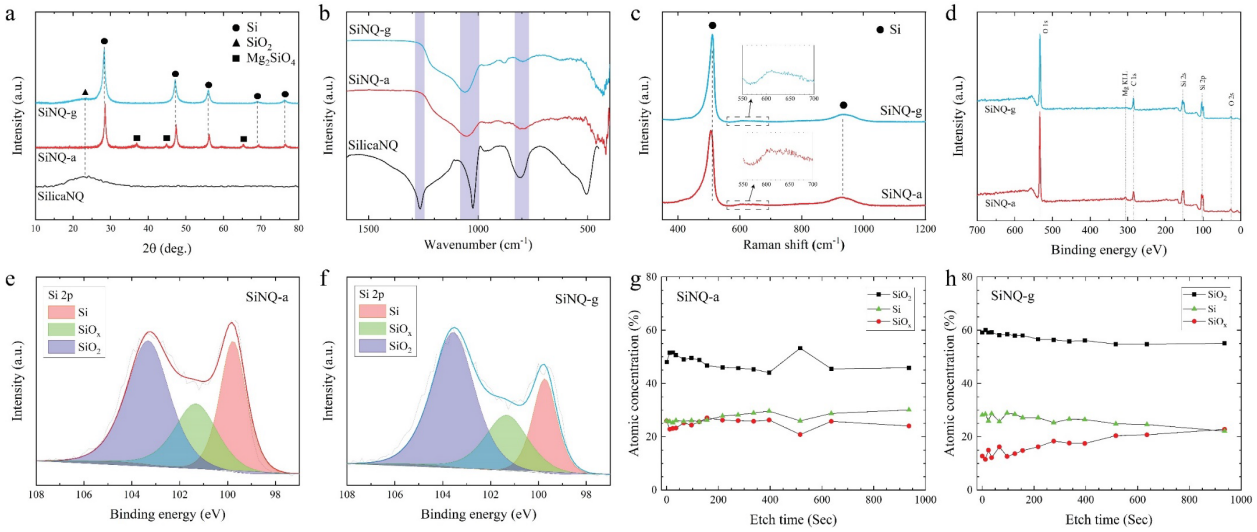

Figure 4.4. Characterization of Si-based materials in this study; (a) XRD spectra of SilicaNQ and both SiNQs, (b) FTIR spectra of SilicaNQ and both SiNQs, (c) Raman spectra of both SiNQs, (d) XPS survey spectra of both SiNQs, and high-resolution Si spectra of (e) SiNQ-a and (f) SiNQ-g materials after 936 seconds of etching, and atomic concentration of different Si-containing species in (g) SiNQ-a and (h) SiNQ-g materials as a function of XPS etch time. Peak fitting is used to calculate the distribution of Si, SiO_x, and SiO_2 species.

The phase evolution from SilicaNQ to SiNQ-a or SiNQ-g was also evaluated through X-ray diffraction (XRD) analysis, and the results are shown in Figure 4.4a. The XRD spectrum of SilicaNQ displays a broad band centered at around $2\theta = 23°$, corresponding to amorphous silicon oxide [165]. Upon reduction of SilicaNQ using both crucibles, the characteristic peaks of crystalline Si appear in XRD patterns of SiNQs, supporting the results from electron diffraction patterns (see Figure 4.2d). In addition, both SiNQ-a and SiNQ-g materials show the band for amorphous silicon oxide. This indicates a partial conversion from silica to Si and the presence of Si oxides in the as-reduced materials. However, the band for the amorphous phase is more noticeable for SiNQ-g material, implying a lower degree of conversion when using a graphite

crucible. It is noted that characteristic peaks of magnesium orthosilicate (Mg_2SiO_4) are detected in the XRD spectrum of SiNQ-a, despite both materials undergoing identical purification procedure using hydrochloric acid solution. We repeated acid treatment of SiNQ-a, but Mg_2SiO_4 peaks persisted. This can be due to structural collapse/fusing of as-reduced material in alumina crucible because of local temperature rise and trapping of Mg_2SiO_4 byproduct within the SiNQ-a structure.

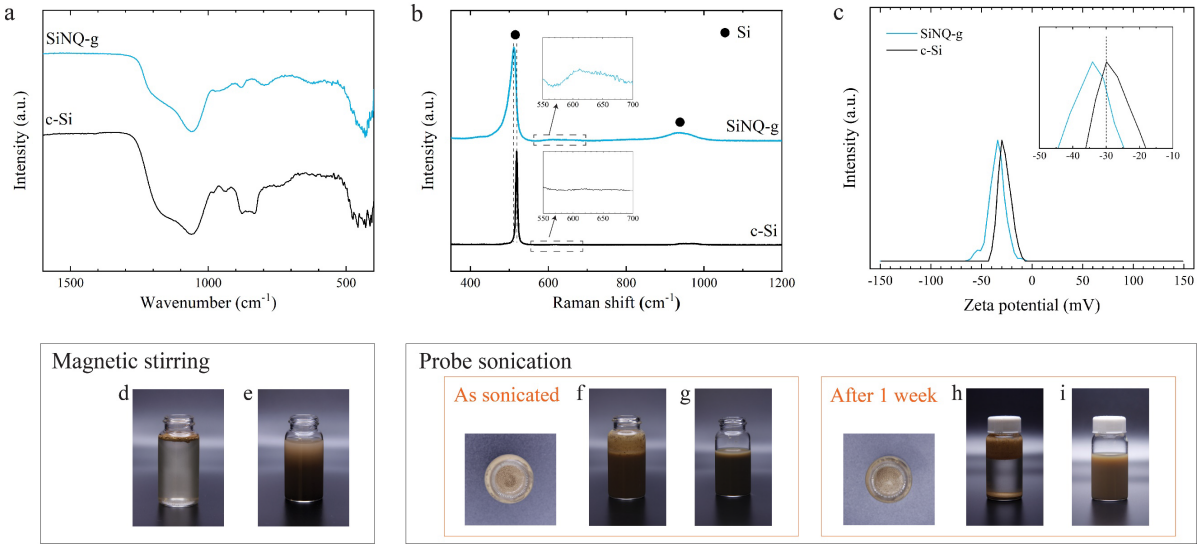

Figure 4.5. (a) FTIR and (b) Raman spectra of SiNQ-g and c-Si materials. Characteristic peaks show the presence of surface functional groups for SiNQ-g, which are absent for c-Si. (c) Zeta potential results of as-sonicated SiNQ-g and c-Si powders in DI water. Dispersion of SiNQ-g and c-Si in DI water using magnetic stirring and probe ultrasonication methods shows that (d) c-Si cannot be dispersed by stirring, while (e) SiNQ-g is easily dispersed after stirring for a short period. Probe sonication of (f) c-Si results in a partial dispersion (remaining c-Si float on top of the water), but (g) SiNQ-g is uniformly dispersed in water after a few seconds of probe sonication. After one week, (h) as-sonicated c-Si gets separated entirely, and (i) SiNQ-g suspension remains stable.

Fourier-transform infrared (FTIR) spectra of Si-based materials in this study are shown in Figure 4.4b. For comparison, the FTIR spectrum of commercial Si (c-Si, crystalline Si nanoparticles with spherical shape and average size of 100 nm) is illustrated in Figure 4.5a. A distinctive broad peak, appearing at 1250 cm^{-1}, in the spectrum of SilicaNQ is indicative of amorphous silica [143]. SilicaNQ also exhibits the 1090 cm^{-1} peak for asymmetric Si–O–Si vibrations, while the symmetric counterpart of these vibrations is present at 795 cm^{-1} [144]. These two peaks are also visible but at a lower intensity for SiNQ-a and SiNQ-g materials. The presence of O in thermally reduced materials is evident from S-TEM elemental maps (Figure 4.6). The c-Si material also shows 1090 cm^{-1} peak for its native silica surface layer. Raman spectra of SiNQs are presented in Figure 4.4c. The ~520 cm^{-1} peak is the characteristic feature of crystalline Si. However, when compared to c-Si, the Si peak in SiNQs exhibits a slight shift towards lower wavenumbers and an increased peak width (see Figure 4.5b). These peak shift and peak broadening effects are attributed to the inclusion of silicon oxides in the material composition [166]. The presence of the peak at approximately 920 cm^{-1} in the second-order Raman spectrum of silicon (Figure 4.4c and Figure 4.5b) typically indicates a two-phonon scattering process, which is inherent to Si-based materials [167]. Additionally, a peak at 630 cm^{-1}, attributed to the wagging vibrations of Si–H bonds, is observed for both SiNQ-a and SiNQ-g materials [168,169]. This peak is absent for c-Si material. The presence of Si–H bonds in SiNQs can promote their dispersibility in water-based slurries. We dispersed a similar amount of SiNQ-g and c-Si powders in DI water using magnetic stirring (Figure 4.5d and e) and ultrasonication methods (Figure 4.5 f and g) to assess this. SiNQ-g material can readily disperse in DI water and create a stable suspension for up to one week, as shown in Figure 4.5h and i, while c-Si is hardly dispersed in DI water. Even after ultrasonication, a large portion of c-Si gets separated and floats on top of the water. The zeta potential measurements of dispersions

of SiNQ-g and c-Si prepared using ultrasonication also verify the stability of SiNQ-g dispersion, showing a zeta potential below -30 mV (Figure 4.5c). We attribute such excellent dispersibility of SiNQ-g in aqueous solution to the presence of Si–H bonds.

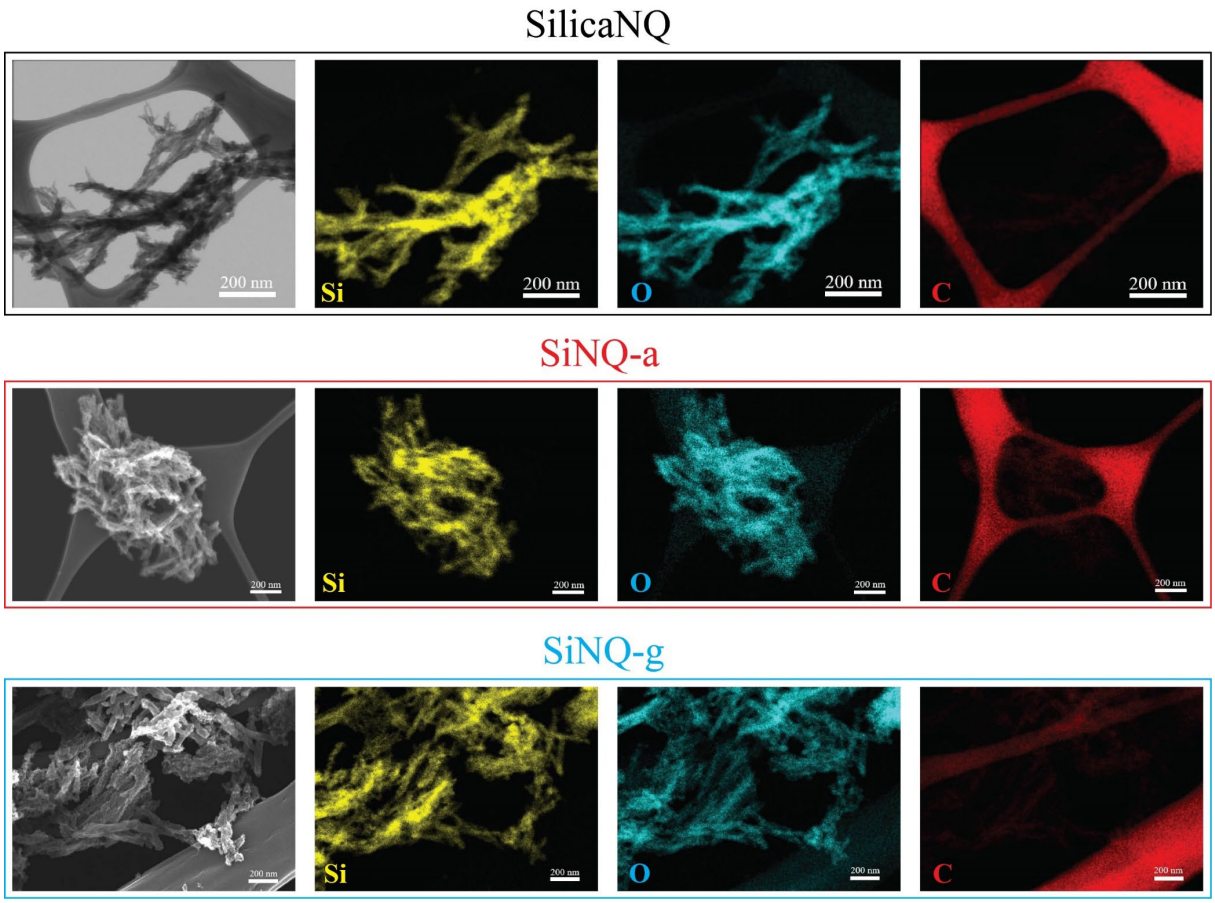

Figure 4.6. S-TEM elemental mapping of nano-quill materials in this study. The elemental maps related to Si, O, and C are illustrated here. The carbon maps are from the lacey carbon structure from the TEM grid.

XPS spectra were analyzed to identify and quantify the presence of different silicon species in SiNQ-a and SiNQ-g materials. The XPS survey spectra in Figure 4.4d show C, O, and Si as expected. The SiNQ-a material contained trace amounts of aluminum and magnesium (0.34 and 0.22 atomic percent, respectively). The presence of aluminum can be attributed to residual

contamination originating from the alumina crucible employed during reduction. The detected magnesium by XPS corresponds to Mg_2SiO_4 byproduct trapped within the SiNQ-a structure (as revealed by XRD results, Figure 4.4a). On the other hand, SiNQ-g material demonstrated no such traces, confirming the absence of thermo-reduction byproducts. High-resolution Si2p spectra of SiNQs are presented in Figure 4.4e and f. Peak fitting of Si2p spectra provides further insight into the distribution of Si (red), SiO_x suboxides ($x < 2$, green), and SiO_2 (purple) species. Argon etching was also used to collect depth profiles for each material to understand how the ratio of these species changed from the surface to the bulk. As seen in Figure 4.4g and h, SiNQ-a has a very inconsistent ratio of SiO_2 and SiO_x, while SiNQ-g is consistent throughout the depth profile. This consistency in Si-based species for SiNQ-g is likely a result of more homogenous reduction, which implies a more effective heat dissipation because of using graphite crucible instead of alumina during exothermic reduction reactions. The $Si:SiO_x:SiO_2$ atomic ratio was estimated over 936 seconds of argon etching, and average atomic ratios of 27:25:48 (for SiNQ-a) and 27:16:57 (for SiNQ-g) were obtained. The higher $SiO_x:SiO_2$ atomic ratio of SiNQ-a material can be attributed to the local temperature rise in the alumina crucible during reduction, leading to a higher degree of conversion from SiO_2 to SiO_x.

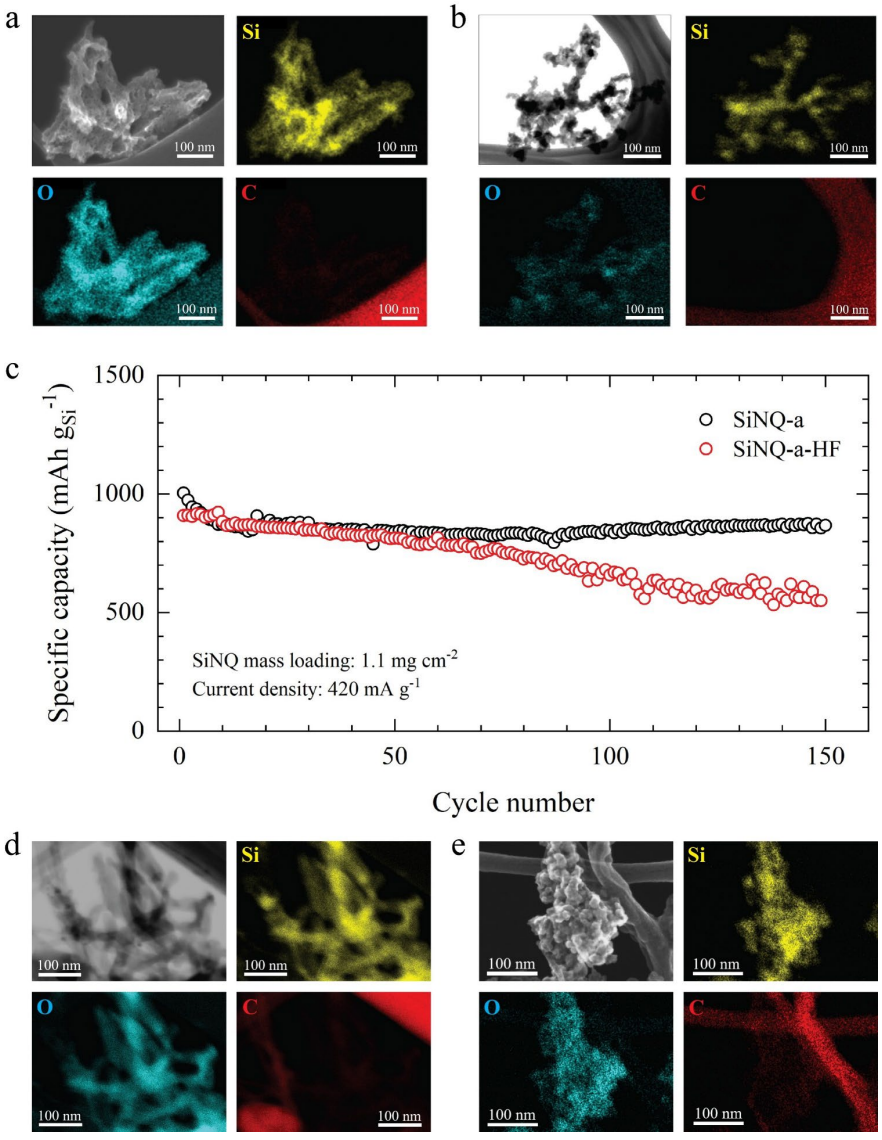

Figure 4.7. STEM micrograph comparing morphological structure of (a) HCl-etched SiNQ-a to (b) HF-etched SiNQ-a. (c) Electrochemical cycling results of anodes prepared using SiNQ-a (HCl etched) vs. SiNQ-a-HF (HCl and HF etched) active material. The delivered capacity was normalized by the mass of active material. (d) STEM micrograph with their respective elemental maps of SiNQ-a anode after 150 cycles, and (e) STEM micrograph with their respective elemental maps of SiNQ-a-HF anode after 150 cycles. It is evident that HCl-treated SiNQ maintained its 1D morphology after cycling.

Efforts were made to eliminate silicon oxides from the HCl-treated SiNQ to derive a material predominantly composed of silicon and evaluate its electrochemical performance. For this purpose, we chose SiNQ-a and subjected it to hydrofluoric acid (HF) etching. The STEM elemental mapping of HF-etched product (*i.e.*, SiNQ-a-HF) confirmed the removal of O-containing species (Figure 4.7b). However, HF etching adversely affected the original tubular morphology of the nano-quills, transforming it into a configuration resembling interconnected spherical clusters. The structure of the nano-quill arms, initially comprising crystalline silicon encased within an amorphous silicon oxide framework, underwent significant alteration. The HF etching process effectively dissolved the amorphous matrix, leaving a sequential arrangement of crystalline silicon entities.

The electrochemical cycling performance of anodes containing SiNQ-a with and without HF treatment is presented in Figure 4.7c. The electrodes were fabricated by casting a slurry of the respective active material onto a conductive Bucky Paper current collector. Half cells were assembled and cycled between 1.0 V and 0.01 V at 0.1C. At a current density of 420 mA g^{-1}, initial reversible capacities of 1003 mAh g^{-1} (for SiNQ-a) and 910 mAh g^{-1} (for SiNQ-a-HF) were acquired. Both anodes exhibited a similar cycling performance up to about 30 cycles. Afterwards, the anode with SiNQ-a-HF showed a capacity decay, and its specific capacity reached 550 mAh g^{-1} at the 150^{th} cycle, while the delivered capacity of SiNQ-a anode remained stable at around 875 mAh g^{-1}. We disassembled the cycled batteries and investigated the active materials using STEM. The acquired elemental mapping for Si, O, and C in cycled active materials is presented in Figure 4.7d and e. The cycled SiNQ-a preserved its 1D morphology without noticeable pulverization or swelling. In contrast, the cycled SiNQ-a-HF is characterized by swollen particles and clear pulverization. This suggests that the unique composition of SiNQs with a silicon oxide

matrix, may significantly contribute to mitigating volume expansion and preserving the integrity of the particles throughout cycling, resulting in remarkably stable cycling performance. Thus, in further work, we utilized SiNQs without HF treatment for preparing Si-graphite composite anodes.

4.2. Electrochemical Performance of SiNQ-a and SiNQ-g

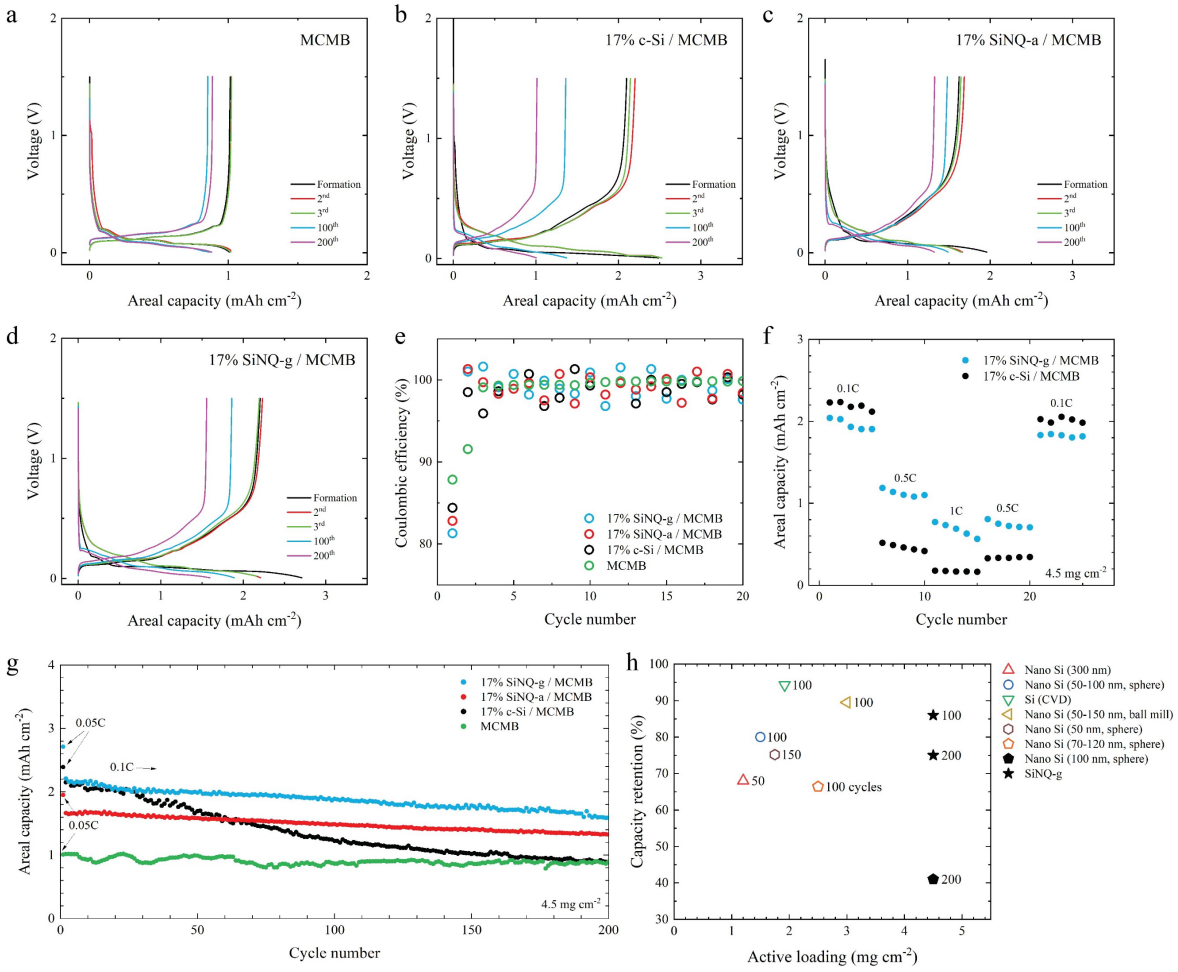

Figure 4.8. Charge-discharge profile of anode half cells with active material comprising (a) pure MCMB graphite, (b) 17% c-Si/MCMB, (c)17% SiNQ-a/MCMB, (d) 17% SiNQ-g/MCMB, and (e) their corresponding Coulombic efficiency for the first 20 cycles, (f) rate performance comparison of composite electrodes containing 17% SiNQ-g and 17% c-Si, (g) cycling

performance of composite electrodes containing 17% c-Si, 17% SiNQ-a, or 17% SiNQ-g, and lastly (h) a literature survey of capacity retention vs. active mass loading for water-based Si-graphite anodes.

Recent developments in commercial LIB anodes for electric vehicles (EVs) have demonstrated that Si-graphite composite materials are promising candidates for efficient lithium storage, leveraging the high capacity of Si-based materials with the ultrahigh stability of graphite [170,171]. the proportion of silicon-based materials in these commercial Si-graphite electrodes for EV batteries usually remains low (<10 wt.%) [172,173]. The Si content is adjusted depending on the targeted balance between increased energy density and cycling stability. In the current study, we followed the slurry composition reported by researchers at the Oak Ridge National Laboratory and Argonne National Laboratory, where 17 wt.% of the graphite is replaced with Si-based materials [99,174]. We combined SiNQ-a or SiNQ-g with conventional mesocarbon microbead (MCMB) graphite to explore the potential performance enhancement derived from our newly developed Si-based nano-quills. We prepared 17% SiNQ-a/MCMB and 17% SiNQ-g/MCMB electrodes coated on a copper foil current collector. Commercial Si (100-nm dia.) was also used to make a 17% c-Si/MCMB electrode for comparison of commercial Si materials to SiNQs. An MCMB electrode (without Si addition) was also prepared for comparison of electrode performance before Si is incorporated. The active mass loading in each of the four electrodes ranged from 3.5 – 4.5 mg cm^{-2}.

All graphite and Si-containing anodes were subjected to a formation cycle at 0.05C followed by cycling at 0.1C for 200 cycles. A current density of 900 mA g^{-1} was designated as the equivalent to 1C derived from multiplying the weight proportion of Si with 4200 mAh g^{-1} and the weight portion of graphite with 372 mAh g^{-1} . The charge-discharge profiles of the anodes and

their corresponding Coulombic efficiency values for the first 20 cycles are plotted in Figure 4.8a-d. The MCMB anode shows an initial Coulombic efficiency (ICE) of 88%. The incorporation of SiNQ-g, SiNQ-a, and c-Si shifts the ICE to 81.3, 82.8, and 84.4%, respectively. At 0.1C, the MCMB anode exhibits a stable capacity of around 0.9 mAh cm^{-2} over 200 cycles (Figure 4.8g). Both 17% SiNQ-g/MCMB and 17% c-Si/MCMB anodes deliver an initial reversible capacity of 2.2 mAh cm^{-2}, which is around 2.5 times the capacity of pure MCMB anode. Notably, this achievement is particularly impressive for anodes containing SiNQ-g, given its composition is comprised primarily of silicon oxides, yet manages to deliver a capacity on par with commercial Si products, which are almost entirely made of elemental Si. After 200 cycles, a distinct divergence occurs, where the 17% c-Si/MCMB anode shows a capacity drop to 0.9 mAh cm^{-2}, corresponding to a capacity retention of 36%. While the 17% SiNQ-g/MCMB anode delivered a capacity retention of 75%. The 17% SiNQ-a/MCMB anode delivers an initial reversible capacity of 1.65 mAh cm^{-2} and a capacity retention of 81% after 200 cycles. In the context of rate performance, the 17% SiNQ-g/MCMB anode outperforms the 17% c-Si/MCMB anode at higher examined current rates, as illustrated in Figure 4.8f. The anode with c-Si exhibits a huge capacity drop from 0.1C to 1C, while the 17% SiNQ-g/MCMB anode delivers a high capacity when subjected to fast charging-discharging at 1C. We conducted a literature survey for water-based graphitic anodes in which 14 – 17 wt.% of the active material consists of Si-based materials (see Table 4.1) and presented a comparative graph in Figure 4.8h. The 17% SiNQ-g/MCMB anode outperforms the others by combining a high active mass loading (4.5 mg cm^{-2}) and decent capacity retention (75%, 200 cycles).

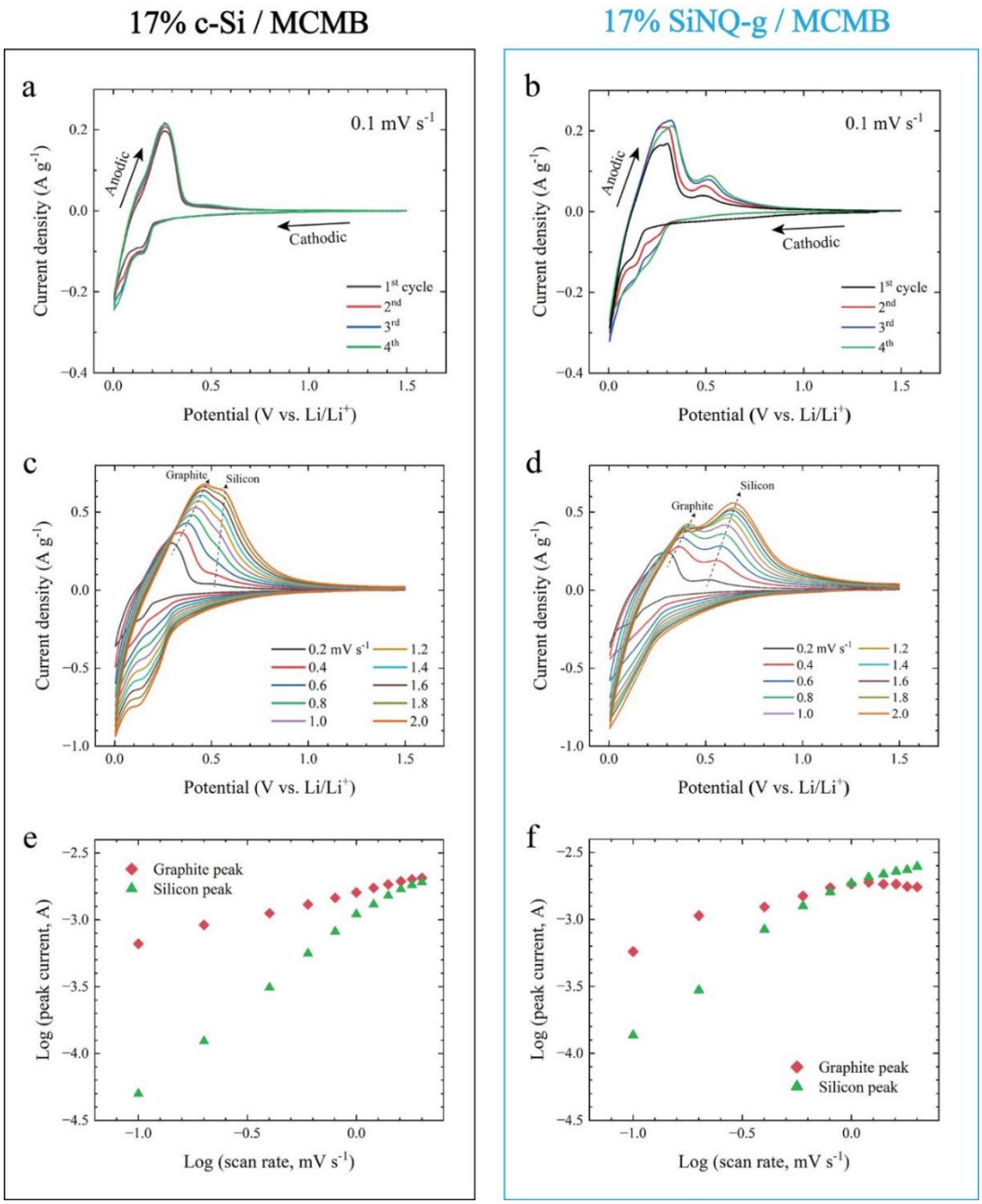

Figure 4.9. Cyclic voltammetry of 17% c-Si/MCMB and 17% SiNQ-g/MCMB anodes. The anodic scan at 0.1 mV s^{-1} is characterized by graphite delithiation peak at around 2.5-3.0 V and silicon delithiation peak at around 0.5 V. These two peaks are evolving at higher scan rates, with different behaviors for c-Si and SiNQ-g.

Utilizing cyclic voltammetry, we investigated the behavior of 17% c-Si/MCMB and 17% SiNQ-g/MCMB electrodes through cathodic and anodic scans, and the results are presented in Figure 4.9. Within the cathodic scan (Figure 4.9a and b), characteristic peaks around 0.03, 0.10, and 0.17 V represent graphite lithiation to form intercalated LiC_x phases [175]. These peaks coalesce with the cathodic signature of Li_xSi alloying observed at 0.18 V [176,177]. In the anodic scan, subtle peaks at 0.25 and 0.29 V denote the progressive delithiation mechanism transitioning from the LiC_6 phase to intermediary species [175]. An additional anodic peak, discernible at approximately 0.5 V, is attributable to the dealloying process of Li_xSi [177]. Cyclic voltammetry measurements were conducted from 0.1 to 2.0 mV s^{-1} scan rate to elucidate the battery reaction kinetics. In the context of 17% SiNQ-g/MCMB anode, the anodic peaks signatures corresponding with LiC_x delithiation (0.25 and 0.29 V) are prominent at lower scan rates. However, at scan rates higher than 0.8 mV s^{-1}, the graphite peaks are overtaken by the anodic peak of Li_xSi (Figure 4.9d). Conversely, for 17% c-Si/MCMB anode, the anodic peak associated with graphite delithiation remains pronounced up to 2 mV s^{-1}, where the peak currents for graphitic and Si delithiation peaks remain in consistent proportions throughout the scans (Figure 4.9c). The ratio of graphitic peak current to Si peak current decreases with increasing scan rate, as shown in Figure 4.9e and f. Thus, at scan rates above 2 mV s^{-1}, the delithiation peak current attributed to Si is projected to exceed that of graphite, including configurations with c-Si. Although the scan rate at which the dominant peak shifts from graphite to Si will differ for the c-Si and SiNQ-g materials studied. The phenomenon, wherein the dominant peak transitions at elevated scan rates, manifests as a recurrent observation for both c-Si and SiNQ-g materials, subverting conventional expectations that Li (de)intercalation from graphite should precede the phase-change governed delithiation of Si-based materials.

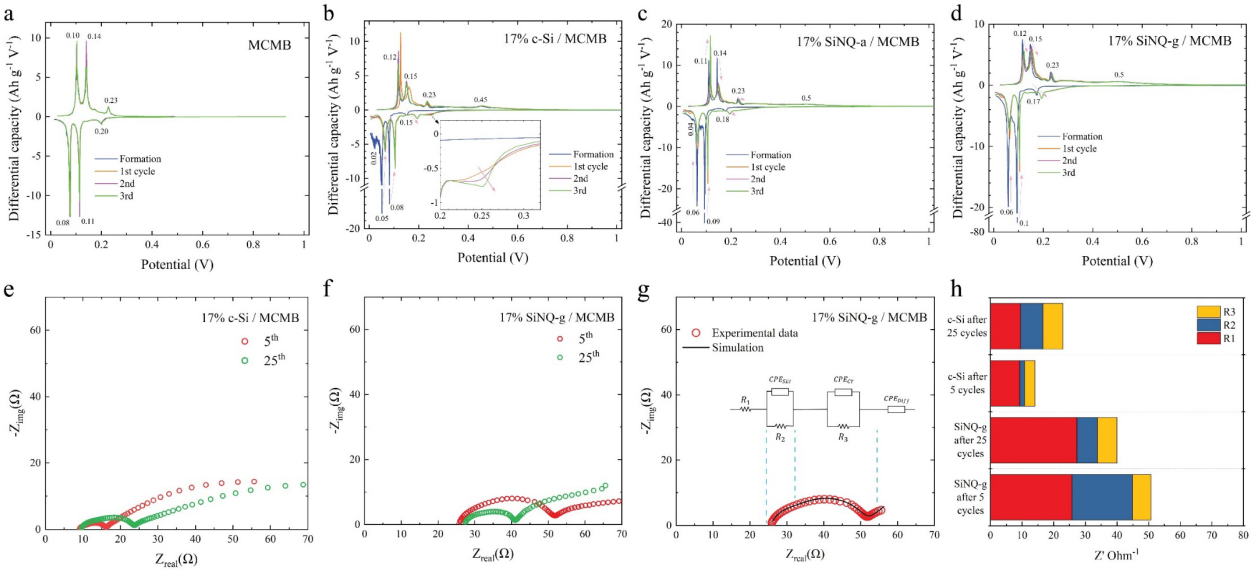

Figure 4.10. Differential capacity plots for all studied anodes: (a) pure MCMB graphite, (b) 17% c-Si/MCMB, (c)17% SiNQ-a/MCM), and (d) 17% SiNQ-g/MCMB (The characteristic peaks in anodic and cathodic curves are marked). Electrochemical impedance spectroscopy results; Nyquist plots of (e) 17% c-Si/MCMB and (f) 17% SiNQ-g/MCMB electrodes after cycles 5 and 25. The equivalent Randles circuit used for modeling the EIS spectra is presented in (g) as an example of an experimental and simulated Nyquist plot. Impedance values derived from fitting models are plotted in (h).

The differential capacity plots (Figure 4.10) display prominent peaks that correspond with the observations identified from the charge-discharge curves. The MCMB anode exhibits characteristic delithiation peaks at approximately 0.11, 0.16, and 0.24 V, in addition to characteristic lithiation peaks around 0.08, 0.11, and 0.20 V, which correspond to the voltage plateaus resulting from lithium-graphite (de)intercalation [178,179]. All composite electrodes with Si-based materials consistently exhibit a lithiation peak at the endpoint of <0.05 V. This peak indicates a phase transition from amorphous to crystalline structures, aligning with the $Li_{15}Si_4$ stoichiometry [87]. Additionally, a broad delithiation peak observed between 0.25 – 0.4 V suggests

the reformation of amorphous Si [180]. Furthermore, a significant delithiation peak appearing near 0.5 V signifies a two-phase reaction, highlighting the conversion from crystalline $Li_{15}Si_4$ to amorphous Li_xSi species [180,181]. Following the formation cycle, a subtle peak emerges at approximately 0.25 V during the lithiation of the 17% c-Si/MCMB anode, as shown in the inset of Figure 4.10b. This peak becomes more pronounced in later cycles. Conversely, this voltage level does not display a noticeable peak for the MCMB, 17% SiNQ-a/MCMB, or 17% SiNQ-g/MCMB anodes.

The emergence of an additional lithiation peak at 0.25 V for the 17% c-Si/MCMB electrode suggests electrolyte decomposition. To delve deeper, electrochemical impedance spectroscopy (EIS) analyses were conducted on both 17% SiNQ-g/MCMB and 17% c-Si/MCMB electrodes at the 5^{th} and 25^{th} cycles. The Nyquist plots (presented in Figure 4.10e and f) were analyzed based on the Randles circuit model shown in Figure 4.10c, and the series resistance (R_1), the SEI resistance (R_2), and the charge-transfer resistance (R_3) values were estimated. The R_1, R_2, and R_3 variations are depicted in Figure 4.10d. Notably, the 17% SiNQ-g/MCMB anode exhibited higher series resistance, potentially due to its greater porosity and consequent higher internal impedance compared to c-Si. Across 25 cycles, R_1 remained relatively unchanged for both anodes, but a marked increase in R_2 and R_3 was observed in the 17% c-Si/MCMB anode, contrasting with a decrease in R_2 and stable R_3 for the 17% SiNQ-g/MCMB anode. The rising R_2 and R_3 values in the 17% c-Si/MCMB electrode, coupled with the additional lithiation peak (inset, Figure 4.10b) , indicate side reactions likely stemming from c-Si particle pulverization during the charge-discharge cycles and electrolyte breakdown on newly exposed Si surfaces [182]. These phenomena underscore the cycling stability challenges faced by the 17% c-Si/MCMB.

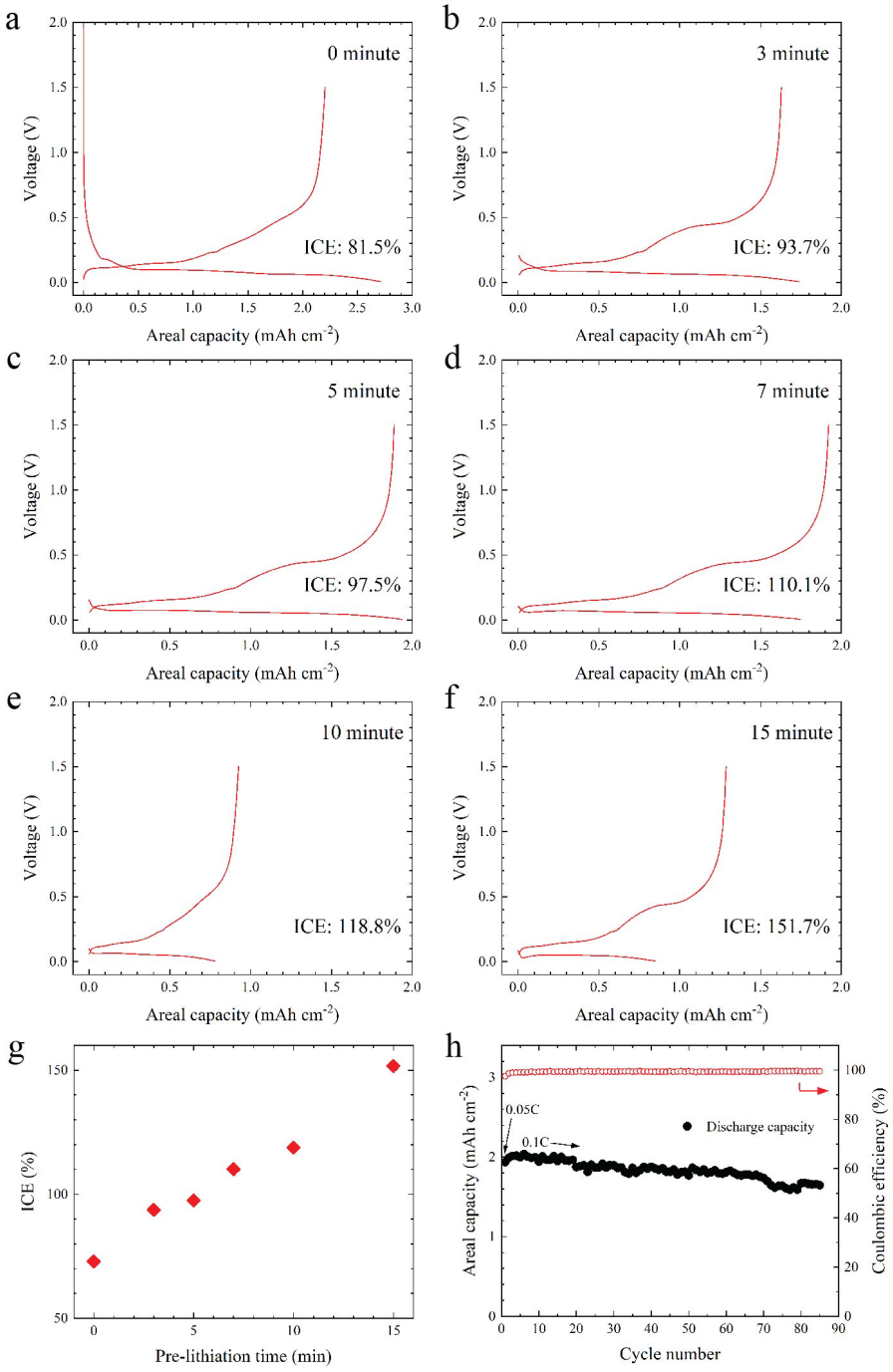

Figure 4.11. Initial charge-discharge profiles for 17% SiNQ-g/MCMB anodes pre-lithiated for (a) 0, (b) 3, (c) 5, (d) 7, (e) 10, and (f) 15 minutes. Summary of (a) ICE outcomes after pre-lithiating and (b) cycling behavior of the optimal pre-lithiated electrode for 5 minutes between 1.5 V and 0.005 V (1C = 900 mA g^{-1}).

As previously demonstrated, the 17% SiNQ-g/MCMB anode exhibits an ICE of 81.3% (Figure 4.8e). The loss of active Li in the first cycle impacts the specific energy density of full cells, where this anode is paired with a cathode containing a limited Li inventory. As such, we conducted a systematic pre-lithiation study to efficiently preset Li^+ ions in the anode active materials and compensate for the initial Li loss. The utilized pre-lithiation process entails direct contact between the 17% SiNQ-g/MCMB electrode and a Li chip under pressure while both of them are immersed in an electrolyte for a specified duration. The charge-discharge profiles of 17% SiNQ-g/MCMB electrodes pre-lithiated for 0, 3, 5, 7, 10, and 15 minutes are summarized in Figure 4.11g. We noticed that the ICE increases monotonically with the pre-lithiation time. An ICE of 97.5% is achieved following a 5-minute pre-lithiation, and thus, it is considered as the optimal pre-lithiation condition. The optimally pre-lithiated electrode was subjected to cycling at 0.1C. As seen in Figure 4.11h, a stable cycling with an average CE of 99.4 % was achieved.

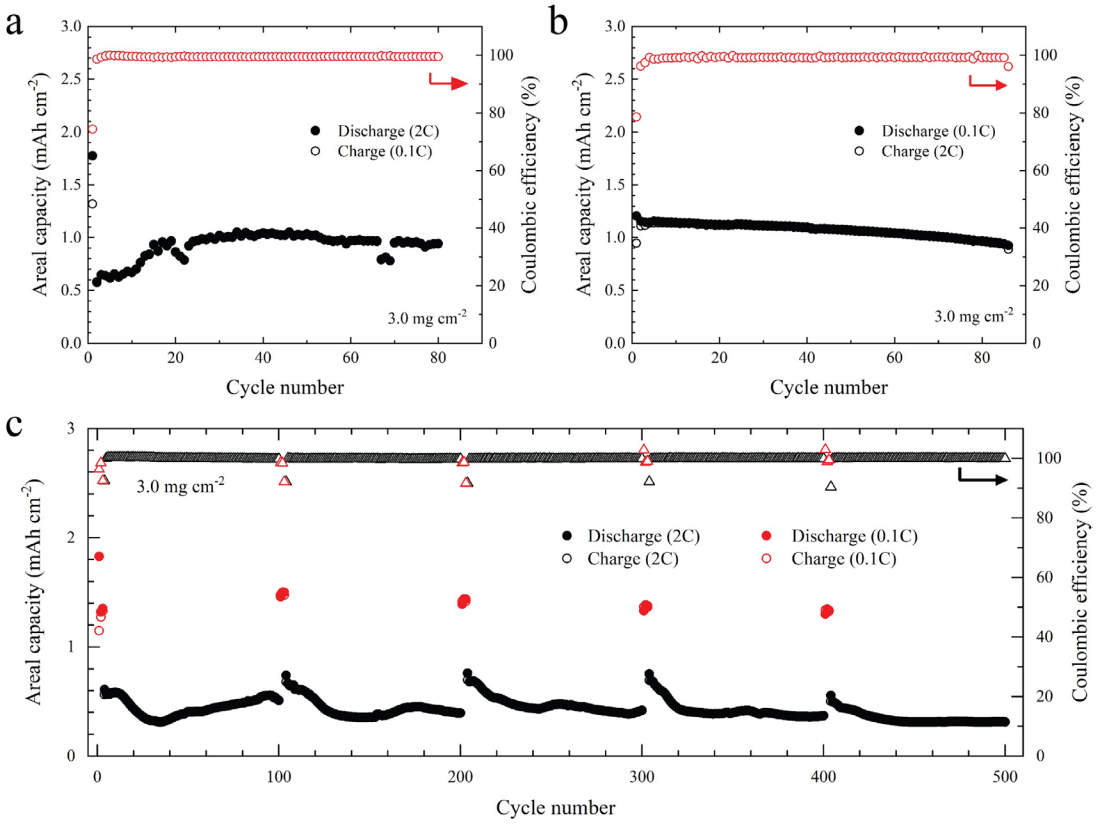

Figure 4.12. Electrochemical cycling of 17% SiNQ-g/MCMB electrodes at high current densities. (a) discharging at 0.1C and charging at 2C, (b) discharging at 2C and charging at 0.1C, and (c) discharging at 2C and charging at 2C. Half cells were cycled between 1.5 V and 0.005 V (1C = 900 mA g^{-1}). The formation cycle was performed at 0.05C.

Fast charging and discharging batteries enhance the versatility of EVs, making the latter suitable for various applications, from long-distance travel to urban commuting. These capabilities would reduce the time required to replenish the vehicle's energy and facilitate features such as regenerative braking and rapid acceleration, improving the overall performance of EVs. To enable fast charging/discharging batteries, Si-graphite anodes must demonstrate enhanced kinetics during both lithiation and delithiation at high current densities. To examine this, we cycled 17% SiNQ-g/MCMB electrodes (with active mass loading of 3.0 mg cm^{-2}) under three different conditions: (*i*) continuous cycling with lithiation at 0.1C (0.27 mA cm^{-2}) and delithiation at 2C (5.4 mA cm^{-2}) in each cycle, (*ii*) continuous cycling with lithiation at 2C and delithiation at 0.1C in each cycle, and (*iii*) alternative cycling in which the anode underwent 3 cycles at 0.1C followed by 97 cycles at 2C, and this process was repeated 5 times (*i.e.*, a total of 500 cycles). The results from these three testing conditions are presented in Figure 4.12.

The battery subjected to lithiation at 0.1C and delithiation at 2C (*case i*) demonstrated a reversible discharge capacity of 1.21 mAh cm^{-2}, maintaining stability in subsequent cycles and achieving a CE of >99% after three cycles (Figure 4.12a). The battery cycled at 2C lithiation, and 0.1C delithiation (*case ii*) delivered a stable capacity of 0.64 mAh cm^{-2}, with a CE of >99% after the second cycle (Figure 4.12b). To assess the anode's recuperative performance following periods of rapid cycling, we subjected the anode to the cycling conditions referenced in *case iii*. As presented in Figure 4.12c, the battery demonstrated an initial reversible discharge capacity of

1.32 mAh cm^{-2} at 0.1C. Following cycles of high current rate exposure (at 2C), the battery's capacity exhibited a notable recovery, achieving values of 1.46, 1.39, 1.33, and 1.30 mAh cm^{-2}, respectively, during each subsequent cycling interval (at 0.1C) interspersed within the test regimen.

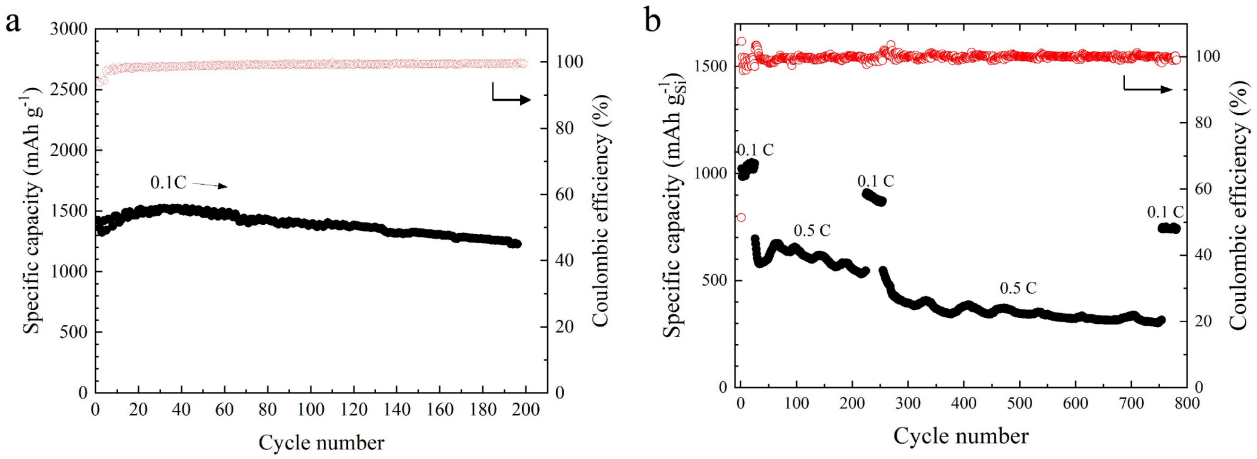

Figure 4.13. Cycling performance of electrode containing only SiNQ-g under (a) constant cycling at 0.1C, and (b) alternative cycling in which the anode underwent 25 cycles at 0.1C followed by 200 cycles at 0.5C followed by 25 cycles at 0.1C then 500 cycles at 0.5C and lastly 25 cycles at 0.1C. Battery half-cell in this study is cycled between 1.0 V and 0.01 V (1C = 4200 mA g^{-1}), and the formation cycle was performed at 0.05C.

We conducted a high current rate cycling experiment on a battery, utilizing solely SiNQ-g as the active material, at approximately 2000 mA g^{-1}. This was done to assess the battery's performance and facilitate a comprehensive comparison with materials previously reported in the literature, as illustrated in Figure 4.13. The battery, subjected to continuous cycling at a rate of 0.1C, exhibited a notable reversible capacity of 1424 mAh $g^{-1}$and maintained 86% of this capacity after 200 cycles. Additionally, the battery underwent cycling at a rate of 0.5C, interspersed with periods of 0.1C to evaluate capacity recovery following high current rate testing. Initially, at

interspersed 0.1C cycling, a capacity of 1000 mAh g^{-1} was recorded. After undergoing 200 cycles at a rate of 0.5C, the capacity restored to 90% of its initial value upon reverting to 0.1C cycling. Moreover, after 700 cycles, it successfully recovered 75% of the original capacity, demonstrating the resili3ence and potential longevity of the SiNQ-g material in high-rate cycling conditions. Furthermore, the electrochemical performance of batteries utilizing only SiNQ-g as the active material is compared with other silicon-based materials synthesized via magnesium reduction, as shown in Table 4.2.

Table 4.1. A literature review of the electrochemical performance of Si-graphite electrodes from aqueous slurries.

Anode				Electrolyte	Half-cell testing condition	Capacity retention (%)	Ref
Active material	**Composition**	**Si content in active material (wt.%)**	**Active mass loading (mg cm^{-2})**				
c-Si/ MCMB graphite	Si/MCMB/ LiPAA/Super P (15:73:10:2)	17	4.5	1M $LiPF_6$ EC:DMC (1:1) + 10% FEC	0.005–1.5 V 90 mA g^{-1}	40%, 200 cycles	This work
SiNQ-g/ MCMB graphite	SiNQ-g/MCMB/ LiPAA/Super P (15:73:10:2)	17	4.5	1M $LiPF_6$ EC:DMC (1:1) + 10% FEC	0.005–1.5 V 90 mA g^{-1}	85%, 100 cycles 75%, 200 cycles	This work
Commercial Si/ Graphite	Si/CNT/graphite/CMC/PAA/Super P (8.8:3.2:68:7.5:7.5:10)	15	1.2	1 M $LiPF_6$ EC:DMC (3:7)	0.01–1.5 V 120 mA g^{-1}	68%, 50 cycles	[68]
Si-C/ Graphite	Si/C/graphite/PAA/ Super P (12:20:48:10:10)	15	1.5	1M $LiPF_6$ EC:DMC (3:7)	0.01–2.0 V 130 mA g^{-1}	80%, 100 cycles	[183]
Si(CVD)@Carbon/ Flaked graphite	Si/C/graphite/CMC/ Super P (12:8:60:5:15)	15	1.92	1 M $LiPF_6$ EC:EMC:DMC (1:1:1) + 5% FEC + 0.5% VC	0.01–1.2 V 200 mA g^{-1}	94.3%, 100 cycles	[184]
Nano-Si@C/ Graphite	Si/C/graphite/CMC& SBR/Carbon black (11.68:31.68:36.64:10:10)	14.6	1.5 - 2.0	1 M $LiPF_6$ EC:DEC (1:1) + 10% FEC	0.005–1.5 V 120 mA g^{-1}	75.2%, 150 cycles	[185]
SiNPs/ Graphite	Si/Graphite/ LiPAA/Super P (15:73:10:2)	17	2.5	1.2 M $LiPF_6$ EC:EMC (3:7) +10% FEC	0.05–1.5 V 87.5 mA g^{-1}	66.4%, 100 cycles	[186]

Table 4.2: Summary of the electrochemical performance of silicon-containing electrodes produced from magnesium reduction.

Starting material	Mg reduction conditions	2nd Cycle capacity (mAh g^{-1})	Capacity Retention	Ref
SiNQ-g	650 °C for 5 h	1424	86% after 200 cycles	This work
SBA-15	660 °C for 5 h	~350	~51.7% after 50 cycles	[42]
SBA-15 coated in carbonized sucrose	660 °C for 5 h	~1200	~87.8% after 50 cycles	
Si nanotube	660 °C for 3 h	1545	~65% after 90 cycles	[187]
SBA-15 coated in carbonized sucrose	660 °C for 5 h	1492	63% after 50 cycles	[44]
SiO_2	700 °C for 5 h	685.8	70.3% after 50 cycles	[46]
Silica-gel on Graphene form Si/graphene	675 °C for 8 h	1743	78.8% after 120 cycles	[47]
Silica from rice husk	650 °C for 7 h	2294	57.1% after 100 cycles	[48]
SiO_2 nanosphere	700 °C for 6 h	2980	73.8% after 50 cycles	[49]
SiO_2 (15 nm)	700 °C for 2 h	1866.2	37.2% after 100 cycles	[50]
MCM-41	650 °C for 7 h	1757	68.3% after 100 cycles	[51]
Glass fiber coated with Carbon	600 °C for 5 h	1059	47.3% after 150 cycles	[52]

Chapter Five : KINETICS OF LITHIUM-ION DIFFUSION THROUGH POROUS AND HOLLOW SI-BASED MATERIALS[**]

5. Synopsis

The electrochemical behavior of lithium-ion batteries (LIBs) is dependent upon the selection of electrode materials and the properties of the materials, which are shaped by a complex network of factors spanning from the atomic level to the macroscopic domain [188]. Understanding the nuances of electrode materials is crucial for formulating tailored strategies that cater to the specificities of each material, thereby optimizing the performance of lithium-ion batteries. Various electrochemical characterization techniques have been employed for kinetic investigations, including cyclic voltammetry (CV), electrochemical impedance spectroscopy (EIS), and galvanostatic intermittent titration technique (GITT). However, methods such as EIS and CV provide an insight into overall average diffusivity, but they do not adequately capture the dynamic nature of Li diffusion within LIBs as a function of state of charge/discharge [89]. A comparative analysis of these techniques reveals that Li diffusion values determined using EIS, CV, and GITT may vary by several orders of magnitude [189]. GITT is emerging as the prominent method due to its capacity to dynamically monitor and analyze lithium-ion diffusion as a function of state of charge / discharge, providing invaluable insights into the electrochemical performance at different state of charge (SOC) levels.

[**] The authors also acknowledge financial support through Clemson University's Virtual Prototyping of Autonomy Enabled Ground Systems (VIPR-GS), under Cooperative Agreement W56HZV-21-2-0001 with the US Army DEVCOM Ground Vehicle Systems Center (GVSC)

The widely-adopted approach for analyzing data derived from GITT involves the application of Fick's equation to calculate the diffusion coefficient. This mathematical relationship, detailed below, provides a rigorous framework for understanding the underlying diffusion processes, however this equation is derived for intercalation-type electrode materials [90,91].

$$D_{GITT} = \frac{4}{\pi}\left(\frac{IV_M}{FS}\right)\left[\frac{\frac{dE(x)}{dx}}{\frac{dE(t)}{d\sqrt{t}}}\right]^2 , \; d \ll \frac{L^2}{D_{GITT}} \qquad (13)$$

Where S is the size of the contact area between the electrolyte and electrode, I is the current that is being applied, V_M is the molar volume of active material, $\frac{dE(t)}{d\sqrt{t}}$ is the straight line slope from plot of the voltage vs square root of time extrapolated from GITT testing, and $\frac{dE(x)}{dx}$ is obtained from the derivative of the equilibrium electrode voltage vs x LixSI plot.

Silicon - a phase transformation material - undergoes phase transformation during the charge/discharge process [86]. This phase change is a crucial aspect to consider in understanding the electrochemical behavior of silicon in battery applications. Equation (13) fails to consider the material's phase transformation, as well as the mechanical stress inflicted on the structure due to the volume changes in silicon throughout the charge/discharge process. This study aims to develop a model to interpret SiNQ GITT, which factors in (a) the phase transformation of silicon, (b) the mechanical stress and volume expansion characteristic to Li-Si alloying, and (c) the distinctive hollow and porous morphology of SiNQ materials.

5.1. Development of GITT Model for Analysis of 1D Hollow and Porous Si Nanotubes

We assume that all the SiNQ particles within a given electrode sample are at the same potential (electrically in parallel). So, to study lithium diffusion within the electrode as a function

of state of charge/discharge, we leverage a single particle model developed below. This single particle model developed to extract lithium diffusion coefficients from the experimental GITT data accounts for (a) phase transformation, (b) volume expansion/contraction and mechanical stress/strain, and (c) innate hollowness of SiNQs.

As shown in Figure 5.1, SiNQ is assumed to have two phases: (a) the delithaited or low state of charge phase α and (b) the lithiated or the high state of charge phase β. The β phase is assumed to be present near the boundaries and the α phase is sandwiched because the hollow nature of SiNQ implies that it will get lithiated from both the inner and outer radii.

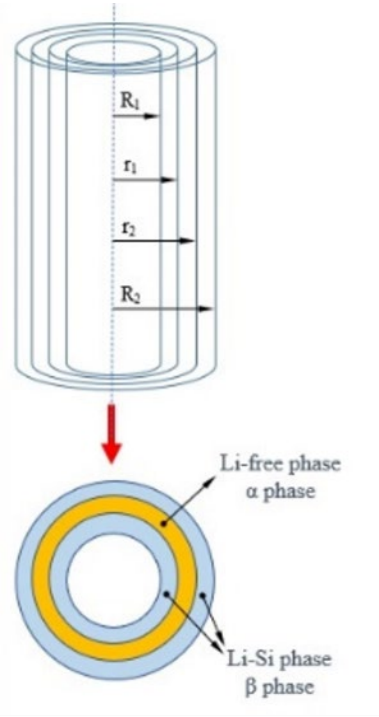

Figure 5.1. Schematic representation of SiNQ and cross sectional overview showing the lithium-free (α) phase and Li-Si (β) phase.

The interfacial boundary condition for flux at an electrode surface is governed by the following equations [190]

$$J_i(r) = -D_i \frac{\partial C_i}{\partial r} + C_i v(r) \quad (14)$$

where $i \in \{\alpha, \beta\}, C$ represents concentration, r the radial co-ordinate, and v stands for interfacial velocity. The interfacial velocity is assumed to be zero within any particular current and rest pulse. However, we update the interfacial location and the inner and outer radii after every rest pulse. This is akin to discretizing the volume expansion/contraction and interfacial movement problem in time. The temporal and spatial variation of lithium concentration is governed by the following equation

$$\frac{\partial C_i}{\partial t} = \nabla . J_i \quad (15)$$

Assuming the interface to be stagnant (as described above) gives

$$\frac{\partial C_i}{\partial t} = \frac{D_i}{r} \frac{\partial}{\partial r} (r \frac{\partial C_i}{\partial r}) \quad (16)$$

where (a) $R_1 \leq r < r_1$ and $r_2 \leq r \leq R_2$ for $i = \beta$ and (b) $r_1 \leq r < r_2$ for $i = \alpha$.

The boundary conditions for the β phase (shown below) assume an immediate charge transfer reaction at the electrode-electrolyte interface. Hence, the lithium flux at the interface should be equal to the rate of electron supply. This implies that

$$-D_\alpha \frac{\partial C_\alpha}{\partial r}|_{r=R_1} = \frac{i\rho_\alpha (R_2^2 - R_1^2)}{2FR_1} \quad (17)$$

$$D_\alpha \frac{\partial C_\alpha}{\partial r}|_{r=R_2} = \frac{i\rho_\alpha (R_2^2 - R_1^2)}{2FR_2} \quad (18)$$

where i represents the specific current density (positive for discharge (lithiation of SiNQ), negative for charge (delithiation of SiNQ), and 0 for the rest pulse), ρ is the material density, and F is the Faraday's constant. Additionally, at the interfaces r_1 and r_2, the flux in both the phases should be equal. Hence,

$$-D_\beta \frac{\partial C_\beta}{\partial r}|_{r=r_1} = -D_\alpha \frac{\partial C_\alpha}{\partial r}|_{r=r_1}, \quad (19)$$

$$-D_\beta \frac{\partial C_\beta}{\partial r}|_{r=r_2} = -D_\alpha \frac{\partial C_\alpha}{\partial r}|_{r=r_2}. \quad (20)$$

The interfacial concentration in the α and β phases is related to each other via the following relationship:

$$(k_1 \frac{C_\alpha}{C_{max}} + b_1)|_{r_1,r_2} = (k_2 \frac{C_\beta}{C_{max}} + b_2)|_{r_1,r_2}, \quad (21)$$

where k_1, b_1, k_2, and b_2 are the slope and intercept of the α and β phase lines, respectively.

The initial condition is as follows:

$$C_i(r, t = 0) = C_{i,init}(r) \quad (22)$$

In order to avoid computational complexities, we solve the problem for the rest pulse ($i = 0$), which makes the governing equations and the boundary conditions homogeneous. This allows us to use the 'separation of variable' technique: a technique used for solving partial differential equations. Briefly, we assume that $C_i(r, t) = G(r)H(t)$. Leveraging the separation of variable technique yields the following analytical solution:

$$C_i = \sum_{n=1}^{\infty} (a_{in} J_0(\lambda_{in} r) + b_{in} Y_0(\lambda_{in} r)) \exp(-\lambda_{in}^2 D_i t), \quad i \in \{\alpha, \beta\} \quad (23)$$

The coefficients $a_{in}, b_{in,}$ and λ_{in} are obtained using the (a) boundary conditions and the (b) initial condition in conjunction with the orthogonality condition (shown in Figure 5.1).

In line with LIB theory, during charge, lithium ions diffuse radially into the active material and are extracted during discharge [191]. This transformation between material phases, coupled with significant volume changes, renders silicon susceptible to brittle fracture [192]. Consequently, a linear elastic model will be employed to analyze deformations and evaluate stress conditions within the α and β phases. The stress-strain relations in cylindrical coordinate system in the radial and tangential direction are as follows [97]:

$$\varepsilon_r = \frac{1}{E}(\sigma_r - 2\nu\sigma_\theta) + \frac{1}{3}\Omega C \quad (24)$$

$$\varepsilon_\theta = \frac{1}{E}((1-\nu)\sigma_\theta - \nu\sigma_r) + \frac{1}{3}\Omega C \quad (25)$$

where σ represents stress, ε represents strain, E is the Young's modulus, Ω is the partial molar volume, and υ is the Poisson's ratio. Due to the assumption of cylindrical symmetry for SiNQ-g, the radial and tangential strains have the following relation [97]:

$$\varepsilon_r = \frac{du}{dr} \quad (26)$$

$$\varepsilon_\theta = \frac{u}{r} \quad (27)$$

where u represents the radial displacement. In the context of solid-state diffusion, mechanical equilibrium is approached as a problem of static equilibrium. This approach is justified by the fact that the diffusion of species within solids transpires at a markedly slower rate than the

process of elastic deformation [193]. Static mechanical equilibrium in the cylindrical is represented by [97]:

$$\frac{d\sigma_r}{dr} + \frac{\sigma_r - \sigma_\theta}{r} = 0 \tag{28}$$

Combining the equations above will allow us to find the equation needed to calculate for the stress component at any point, r_1, where $R_1 \leq r_1 \leq R_2$. The equation is as follows:

$$\begin{aligned} 2(1-\nu)\,[r^2\sigma_r(r_1)] - \nu(r_1^2 - R_1^2)\sigma_{r,ave}(r_1) \\ = -\frac{E\Omega}{3}(r_1^2 - R_1^2)C_{s,ave}(r_1) + (r_1^2 - R_1^2)constant_2 \end{aligned} \tag{29}$$

where $\sigma_{r,ave}$ represents the average stress concentration in the cylinder, and given by the following equation:

$$\sigma_{r,ave}(r_1) = \frac{2}{(r_1^2 - R_1^2)}\int_{R_1}^{r_1} \sigma_r r\, d\sigma_r \tag{30}$$

The aim, using these equations, is to analyze data from GITT experiments, segregate individual current pulses, and refine the concentration equations to align with the experimental data, adjusting D_α for the best fit. This process will determine D_α for each pulse, resulting in a plot of lithium ion diffusion in relation to the state of charge.

5.2. Results and Discussion

The material properties of Li and Si are summarized on Table 5.1.

Table 5.1. Active material properties

Parameters	Values
Ω_{Si} ($m^3\ mol^{-1}$) [194]	9×10^{-6}
Ω_{Li} ($m^3\ mol^{-1}$)	1.297×10^{-5}
$c_{Si,max}$ ($mol\ m^{-3}$) [195]	278000
c_{th} ($mAh\ g^{-1}$)	1800
$\Delta\ c_{th}$ ($mAh\ g^{-1}$)	104.955

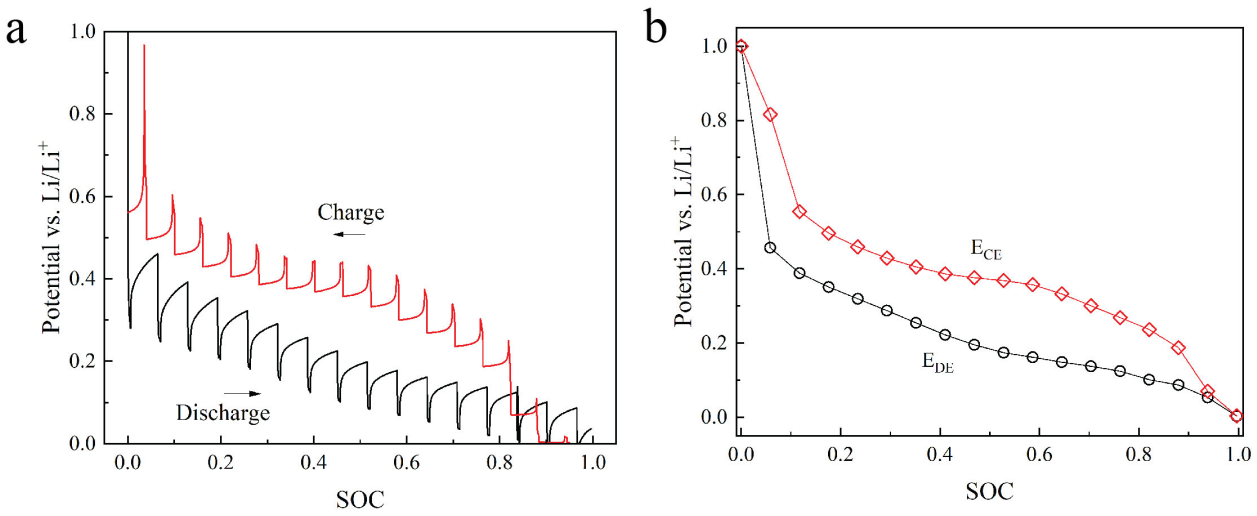

Figure 5.2. *(a) Charge and discharge GITT curve for SiNQ sample and (b) equilibrium potential from charge and discharge GITT curve.*

The data derived from GITT testing, showing the voltage response during the current pulses are plotted in relation to the state of charge (SOC) and depicted in Figure *5.2*a. The voltage plateau where the equilibrium voltage is achieved is extrapolated from every rest period and presented in Figure 5.2b. The SOC was determined using the theoretical capacity of Si-SiOx mixture (~1800 mAh/g), the applied current pulse, pulse duration, and the total mass of Si present

in the electrode, and the Si:SiOx ratio of 27:73 (determined experimentally in previous chapters). These calculations were performed utilizing the following equations [90]:

$$\Delta c = -\frac{I\,t}{m_{AM}} \quad (31)$$

$$SOC^{p+1} = SOC^{p} + \frac{\Delta c}{c_{th}} \quad (32)$$

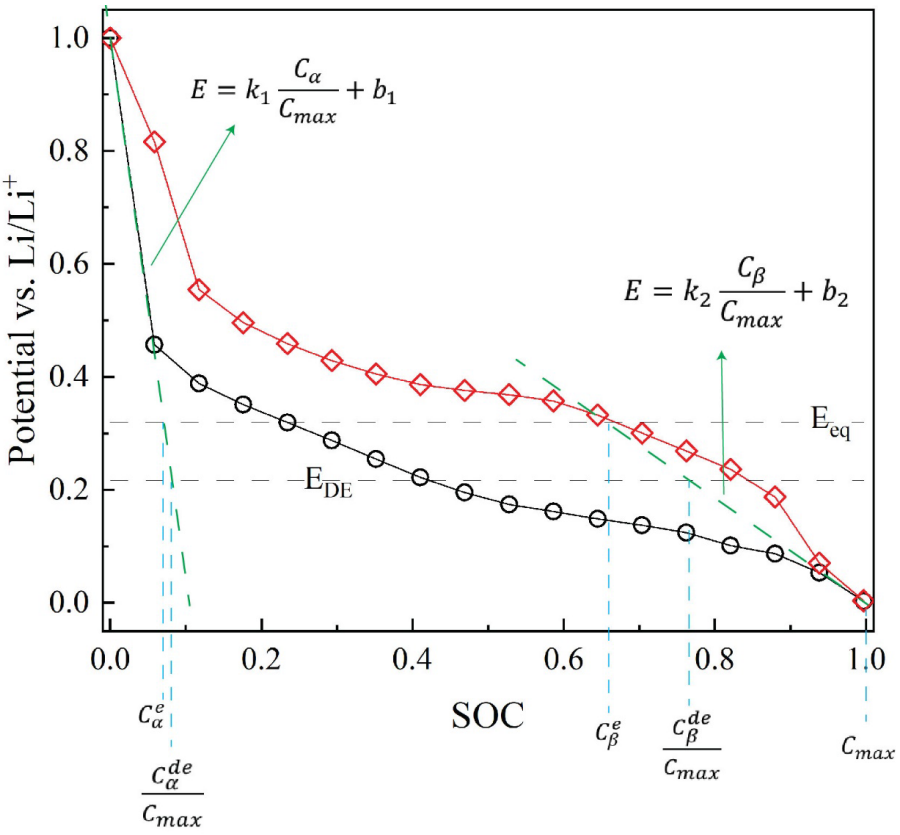

Figure 5.3. GITT parameters were derived in accordance with the potential-composition isotherm chart, as elaborated in the schematic diagram by Zhu and Wang [91].

GITT parameters required for simulation purposes must be extracted from the equilibrium potential plot illustrated in Figure 5.2b. The process employed to extrapolate these parameters is meticulously outlined in Figure 5.3and the results are listed in Table 5.2. The equilibrium potential (E_{eq}) is approximated by taking the mean of the discharge equilibrium potential (E_{DE}) and the

charge equilibrium potential (E_{CE}) [91]. The slope profile is derived by applying the slope formula to the first and second discharge equilibrium points, as well as the last two discharge equilibrium points. Subsequently, the essential parameters outlined in Table 5.2 are determined by tracing vertically downward from the intersection points to locate their corresponding values on the x-axis. The parameters k_1, k_2, b_1, b_2 were obtained by fitting straight lines to the 1st 2 discharge equilibrium voltage and the last 2 charge equilibrium voltage points.

Table 5.2.Parameters for GITT simulation.

Parameter	Value
b_1	1
k_1	-9.3153
b_2	1.1374
k_2	-1.1439
C_{max} (mol/cm^3)	4333.12
C_a^e (mol/cm^3)	254.8894118
C_b^e (mol/cm^3)	4078.230588
$\frac{C_a^e}{C_{max}}$	0.058823536
$\frac{C_\beta^e}{C_{max}}$	0.94117657

In order to solve the governing equations, for the rest pulses, it is necessary to determine the initial concentration profile at the beginning of the rest pulse. The initial concentration profile at the beginning of the rest pulse can be determined by studying the evolution of interfacial concentration towards the end of the preceding discharge pulse. The experimental interfacial concentration profiles for the α and β phases were found to evolve linearly with time for the last portion of the pulses. The linear fits for the α and β phase are shown in Figure 5.4a and b. This

indicates that the change in concentration due to lithiation at the electrode-electrolyte interface is directly leading to a change in concentration at the interface between α and β phases, shown as r_1 and r_2 in Figure 5.4c. This is only possible after concentration gradients have been established throughout the β/α phases and when the slope and curvature of the concentration profile (in radial direction) does not change over time. However, the concentration itself increases as a function of time because of the ongoing lithiation process.

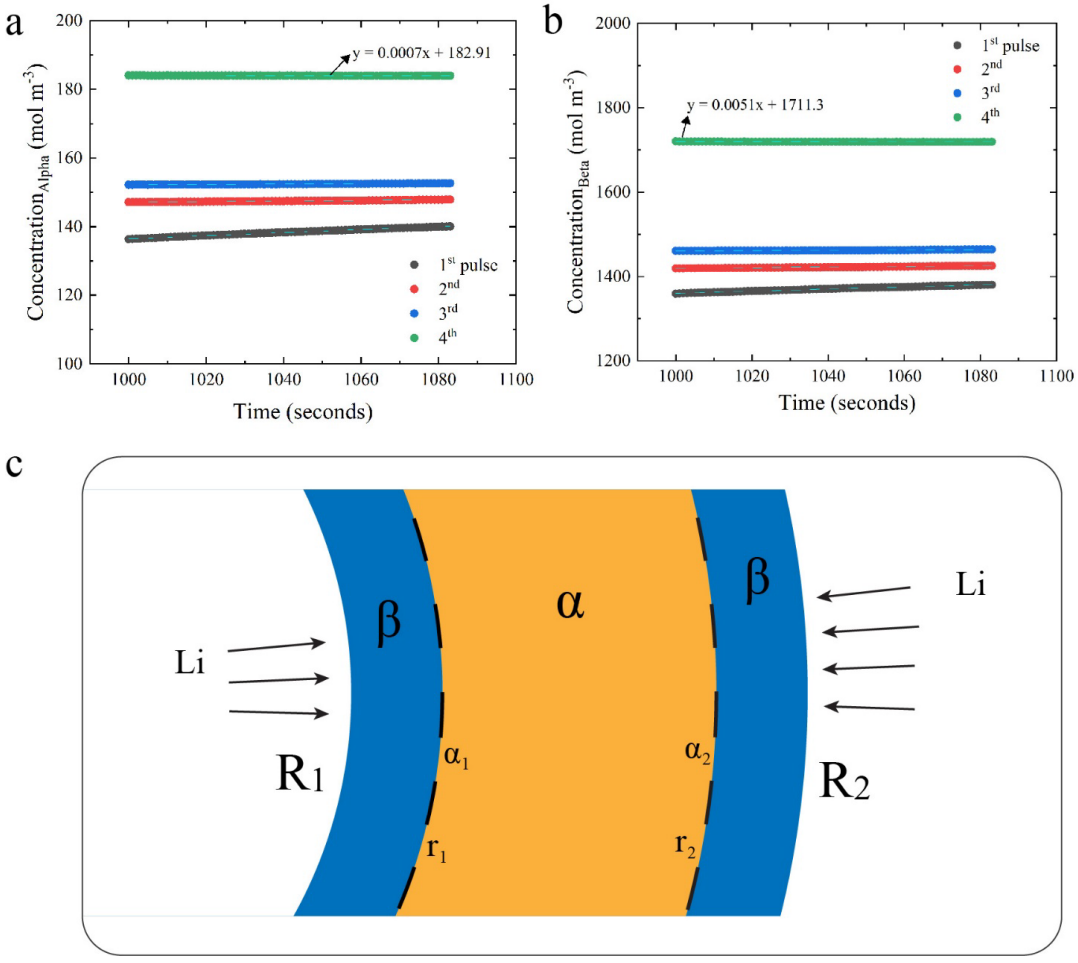

Figure 5.4. Concentration profiles showing the linear region of each current pulse and the subsequent fitting for the (a) alpha phase and (b) beta phase, and (c) schematic representation of the phase separation.

This determination of the initial concentration profile for the rest pulse leverages both (a) the known interfacial concentration values at the start of the rest pulse and (b) the fact that the current during the rest pulse is equal to zero (implying slope of concentration profile (in the radial direction) at the electrode-electrolyte interfaces should be equal to 0). The initial concentration profile for the rest pulse is of the form shown below

$$C(r) = \frac{C_0 r^2}{4D_\beta} - C_1 \ln(r) + C_2, \quad (33)$$

where C_0 is the slope of the interfacial concentration with respect to time towards the end of the preceding discharge/charge pulse.

One Term approximation

Using the above mentioned initial concentration profile, the orthogonality condition and the boundary conditions, an exact solution may analytical solution seems possible. However, due to lack of available computational resources (software such as MATLAB) which are needed to solve coupled non-linear equations simultaneously, a 'one term approximation' approach was adopted. In one-term approximation approach, only the first term (i.e. the lowest eigenvalue (λ)) of the infinite summation series for the concentration profile is considered. This is because the contribution of terms with higher eigenvalues are expected to drop to zero much faster compared to the terms with smaller eigenvalues. While this simplifies the problem, it does lead to root-mean-squared error of about 10% for both C_β and C_a when compared to the experimental profiles. The % error was calculated with respect to the difference in experimentally obtained interfacial concentrations at the start and the end of the rest pulse. The plots obtained from the first rest pulse have been shown in Figure 5.5. Efforts are in progress to improve the accuracy of the fits by incorporating a few more terms with higher eigenvalues.

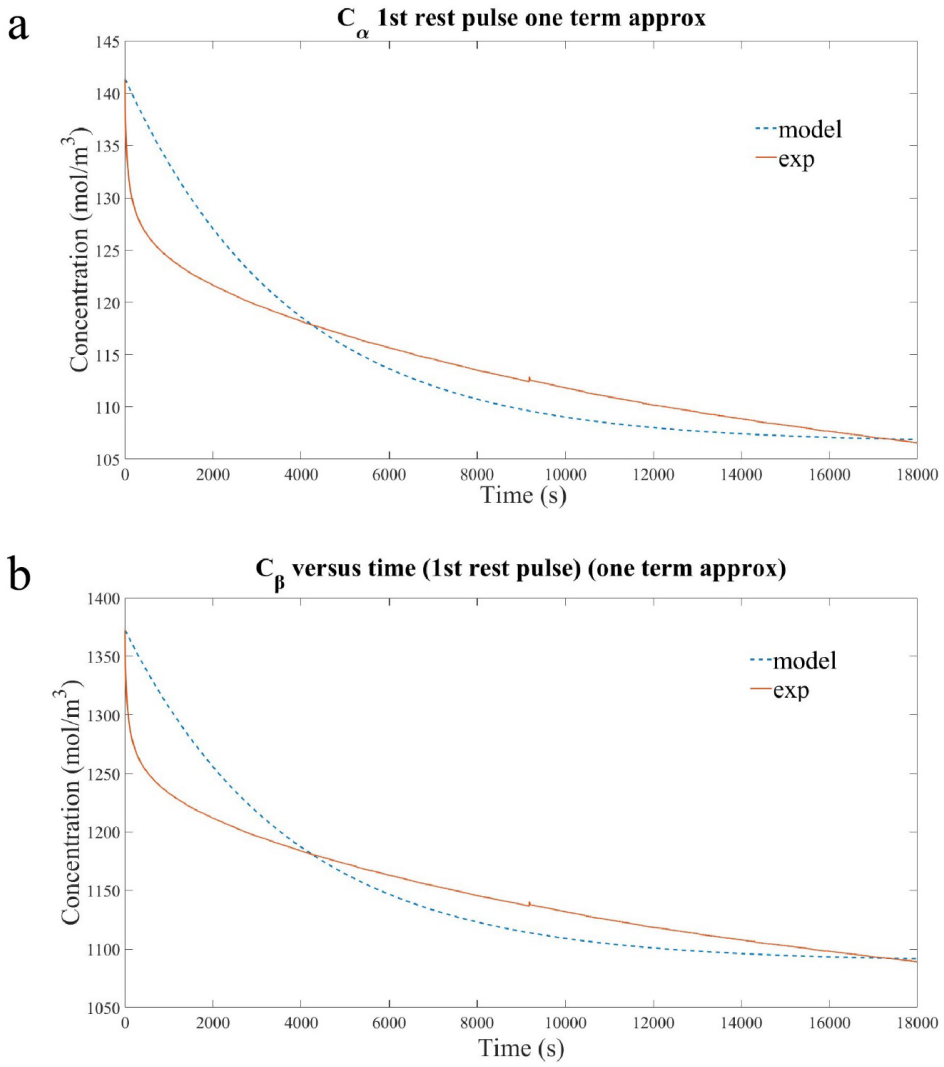

Figure 5.5. Simulated fitting of the rest period for the concentration profile in the (a) α and (b) β phase.

Utilizing a single-term approximation introduces certain limitations due to the single value of λ, which represents a specific length scale (as λr- the argument of Bessel functions in the concentration profile- is non-dimensional). Hence, this method fails to capture the full spectrum of relevant length scales that vary over the duration of the rest period. These variations in length scale can result from different phases—already taken into account—or due to volume changes over time. To address this, we propose fitting the model for each one-hour interval.

To address this, we propose fitting the model for each one-hour interval, recalculating the values of C_0, C_1, and C_2 for both α and β phase. This approach allows for the approximation of constant straight slopes representing the diffusion length scale within each period. We will need to find the steady state concentrations of $C_{\beta,SS}$ and $C_{\alpha,SS}$ from

$$Total\ moles\ of\ Li = C_{\beta,SS} \times V_\beta + C_{\alpha,SS} \times \mathrm{V}_\alpha$$

$$1.7776E^{-6} = C_{\beta,SS} \times 1.0022E^{-9} + C_{\alpha,SS} \times 2.88447E^{-9}$$

Note that the volume and moles here are at the electrode level. $C_{\beta,SS}$ and $C_{\alpha,SS}$ are also related by the following relation:

$$k_1 \frac{C_{\alpha,SS}}{C_{max}} + b_1 = k_2 \frac{C_{\beta,SS}}{C_{max}} + b_2$$

$$C_{\alpha,SS} = \frac{C_{max}}{k_1}\left(k_2 \frac{C_{\beta,SS}}{C_{max}} + b_2 - b_1\right)$$

$$Total\ moles\ of\ Li = C_{\beta,SS} \times V_\beta + \frac{C_{max}}{k_1}\left(k_2 \frac{C_{\beta,SS}}{C_{max}} + b_2 - b_1\right) \times \mathrm{V}_\alpha$$

$$C_{\beta,SS} = \frac{Li_{total} k_1 - C_{max} V_\alpha (b_2 - b_1)}{k_1 V_\beta + k_2 V_\alpha}$$

$$C_{\beta,SS} = 1368.2\ mol\ m^{-3}$$

However, the experimental data suggests that the extrapolated C_β concentration within the first 5 seconds is below 1348 mol m^{-3}. So this implies that there is a volume change during the first cycle. Figure 5.6 shown below shows that the diffusion coefficients obtained using Eq. 1 for the lithiation

and delithiation pulses ~ 1E-16 m^2 s^{-1}. However, as shown in Figure 5.4a and b, the interfacial concentration grows linearly with time for almost all the charge/discharge pulses during at least the last 200 s. This indicates that the shape of the spatial concentration profile does not change over time after the first 1600 s, implying that the lithium ions have traversed across the α/β phase. Thus, an order of magnitude analysis to get an approximate diffusion coefficient suggests that $D \sim \frac{L^2}{t}$ where $t \sim 1600$ s, and L is the length scale of the corresponding phase. L can be obtained by calculating the interfacial radii r_1 and r_2. The interfacial radii after the first discharge pulse (which leads to lithiation of SiNQ) are obtained by (a) assuming that total volume before and after lithiation has not changed (this is not very far from reality for the first pulse as state of charge does not change significantly within one pulse), (b) the concentration profile at the end of the rest pulse is uniform within a particular phase, and the concentration is equal to the interfacial concentration. Since lithiation only takes place during the discharge pulse, the total number of moles of lithium ions at the end of rest pulse should be equal to the number of moles of lithium at the end of the preceding discharge pulse. This calculation yields $D_\beta \sim 1E-22\ m^2 s^{-1}$ and $D_\alpha \sim 1E-21\ m^2 s^{-1}$ for the first discharge pulse. This clearly shows that not accounting for phase transformation can lead to an over-estimation of diffusion coefficients by 5-6 orders of magnitude. Literature on lithium-ion kinetics in Si materials indicates a lithium diffusion coefficient range from 10^{-12} to 10^{-11} [92,93] for Si nanoparticles, and 10^{-11} to 10^{-9} for porous 3-dimensional Si [96]. Variations in diffusion coefficient values is attributed to factors including particle size, electrode tortuosity, surface area, and morphology [92]. The diffusion coefficient values from literature are not distinguished by their respective phases due to the limitations of Eq. 1. Zhu and Wang's GITT modeling of lithium iron phosphate electrode reported diffusion coefficients values for the α and β phase, highlighting the need for distinction between the two phases [91]. This underscores the

importance of a tailored approach for GITT modeling to obtain an accurate representation of lithium-ion kinetics in SiNQ.

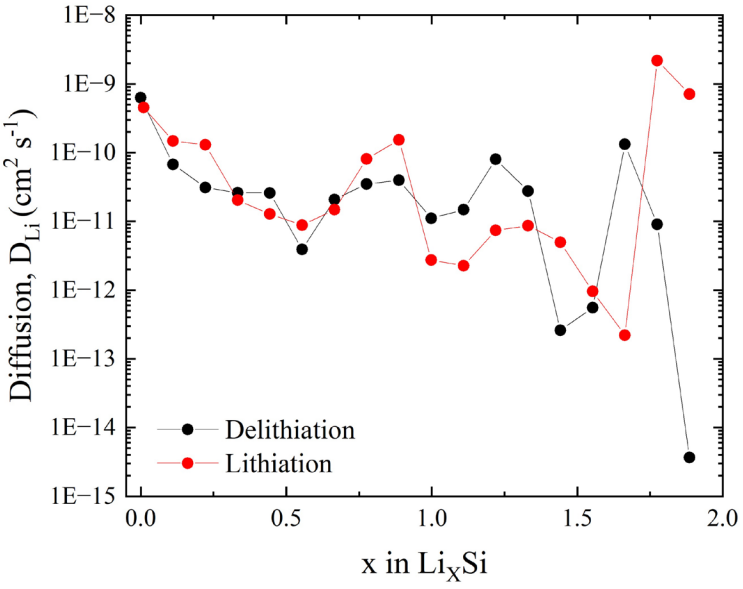

Figure 5.6. Diffusion coefficient calculated based on equation (13)

Chapter Six : SUMMARY AND FUTURE WORK

6. Summary

6.1. Summary: Cellulose Nanocrystals as a Bio-template for Silica Formation

The commercial integration of silicon-based batteries has been constrained to a 5-10 wt.% silicon content in Tesla Model 3 batteries, primarily due to the substantial volume expansion of silicon materials [196]. Engineering specialized structures that offer space for expansion is deemed the most effective solution to this challenge. Although numerous strategies for addressing this issue have been explored, as detailed in Chapter 1, they frequently involve the use of hazardous chemicals that raise safety issues or present scalability challenges. The research proposed here seeks to harness bio-renewable cellulose nanocrystals (CNCs) to develop valuable silicon-based materials for LIBs. It highlights the advantages of using CNCs as a bio-template for generating materials with exceptional surface area and porosity. Given their abundance, renewability, and distinct structural features, CNCs serve as an ideal foundation for crafting high surface area, porous silicon-based materials. This approach leads to the development of SilicaNQs, characterized by their significant surface area and porosity, providing a greener, sustainable, and economical method for producing one-dimensional porous silicon-based materials.

This study meticulously examined the critical factors influencing silica formation to achieve a defect-free silica product. It comprehensively explored the impact of solvents, co-solvents, catalysts, and the template-to-surfactant ratio on silica formation. The BET surface area and BJH pore volume of the SilicaNQ material synthesized surpassed the performance of commercially available mesoporous silica product. In addition, a streamlined one-step carbon coating technique was introduced, where the template is seamlessly converted to carbon in one simple pyrolysis step. This innovation significantly enhanced the electrochemical performance,

notably doubling the capacity of SilicaNQ@C. Additionally, the study successfully demonstrated the scalability of the material production process, transitioning from 200 mgs per trial to several grams per trial in a laboratory setting. The novel templating method and scalable process developed in this chapter was awarded a patent [197]. Despite this progress, the process is still categorized as small-scale, so achieving full commercialization would necessitate collaboration with a manufacturing partner to realize its market potential.

6.2. Summary: Magnesiothermic Reduction for Formation of Si-based materials from Templated Mesoporous SilicaNQ

Leveraging the ultra-high surface area and significant pore volume material discussed in Chapter 3, this study utilized magnesiothermic reduction to transform silica into elemental silicon. The primary aim was to explore how different crucible materials, selected based on their thermal diffusivity properties, impact the final product. Specifically, alumina and graphite crucibles were compared, noting that graphite's thermal diffusivity surpasses alumina's by tenfold at 650°C. By varying only the crucible material, we aimed to discern its influence on the morphological integrity of the resultant SiNQ materials. The findings revealed that SiNQ-g, processed in graphite, boasted a BET surface area double that of SiNQ-a and maintained more of its original hollow structure and porosity under electron microscopy. Addressing the challenge of structural collapse during the conversion of silica into Si could unlock a broader range of technological applications for Si. The novel method of utilizing a high thermally diffusive crucible material and the resulting novel Si materials for lithium-ion battery applications were also mentioned in the patent [197]. Moreover, this research path led to the elimination of hydrofluoric acid (HF) etching, enhancing the process's safety and sustainability.

Most notably, the SiNQ materials are water dispersible, eliminating the need for toxic solvents such as NMP, that is typically used in the slurry making of hydrophobic commercial Si nanoparticles. The SiNQ materials possess unique material properties, characterized by crystalline Si pockets within an amorphous Si suboxide matrix. Graphite co-utilization was investigated to understand how SiNQ performs with commercial graphite battery materials. SiNQ-graphite composite anodes, comprising 17 wt.% SiNQ and achieving an active mass loading of 4.5 mg cm^{-2}, were fabricated using a water-based slurry. The distinct one-dimensional, hollow morphology of SiNQ arms accommodates the volumetric fluctuations during lithium insertion and extraction, resulting in anodes of high capacity and excellent cycling stability. Remarkably, SiNQ-g materials, rich in Si suboxides, matched the capacity of commercially available pure Si nanostructures, highlighting their effectiveness. In addition, SiNQ-based anodes showcased high capacity and remarkable cycling stability under high current density (5.4 mA cm^{-2}) cycling. A critical barrier to commercialization is the depletion of active lithium in the battery after the initial cycle. Prelithiation strategies are adopted commercially to overcome the active material loss [198]. A straightforward pre-lithiation strategy was implemented for SiNQ, yielding anodes with nearly 100% initial coulombic efficiency (ICE), representing a notable breakthrough in enhancing the performance of lithium-ion batteries.

6.3. Summary: Kinetics of Lithium-ion Diffusion into SiNQ

SiNQ is a unique material produced from this research, therefore it is crucial to elucidate the lithium-ion kinetics in the material. To address the complexities inherent in LIB research, specifically in analyzing lithium kinetics during the GITT tests, a sophisticated approach to solving the governing equations was necessary. This entailed determining the initial lithium concentration profiles at the onset of rest periods, which were inferred from the linear evolution of interfacial

concentrations at the end of discharge pulses obtained from experimental data. This linear relationship indicated a direct link between concentration changes at the electrode-electrolyte interface and the phase interfaces, suggesting a steady concentration lithium-ion gradient within the material. Utilizing these insights, along with well-established boundary conditions, an initial concentration profile for each rest period was established. Given the computational limitations and the complexity of solving coupled non-linear equations, a 'one term approximation' method was employed, focusing on the term with the lowest eigenvalue (i.e. first term) for simplification, though this resulted in a root-mean-squared error of approximately 10%. Despite the simplification, this method provides a foundational understanding of lithium kinetics within the β and α phases of LIB materials. Future efforts aim to refine this model by incorporating additional terms to enhance the accuracy of the simulations, as demonstrated in the initial rest pulse findings. This research underscores the dynamic interplay of lithium concentration gradients in LIBs and offers a pathway to more accurately model and predict battery behavior under various charging conditions.

6.4. Future work

For the SilicaNQ materials, our research focused on evaluating their electrochemical performance using buckypaper as the current collector. However, for successful commercialization, transitioning to copper foil as the standard current collector is imperative. The choice to utilize buckypaper in this study stemmed from challenges encountered in the formulation of effective slurries for copper foil applications. Despite experimenting with various polymer binders, including PAA, PVDF, CMC, SBR, and sodium alginate, among others, in diverse slurry compositions, these initial trials did not yield satisfactory outcomes. This necessitates a more

exhaustive future exploration to identify a viable slurry formulation compatible with metallic foils, which are prevalent in commercial battery manufacturing processes.

In the investigation of SiNQ materials, a critical aspect was the analysis of volume changes after battery testing, which presented several challenges. Focused ion beam (FIB) milling is a widely employed technique for material etching to reveal cross-sectional areas without compromising coating integrity, especially in terms of compression. We experienced obstacles due to the high hardness of graphite within the electrode, which drastically increased the mill time and the beam strength required. A key consequence of using a higher beam strength is the risk of copper redeposition on the exposed surfaces when the gallium beam reaches the copper foil, hampering SEM analysis of electrode expansion. Our objective in the future work is to refine the FIB milling procedure to prevent copper foil redeposition on the surface of milled sections. Furthermore, we have established collaboration efforts with Sandia National Laboratory on future in-situ TEM studies, aiming to understand the behavior of SiNQ during lithiation and delithiation processes in a more comprehensive manner.

For future work on GITT analysis, our aim is to enhance the precision of the current model by incorporating additional terms. This initiative is inspired by insights gleaned from the initial analysis of rest pulse behavior. Our goal is to develop a robust model that accurately captures lithium-ion dynamics within SiNQ materials, contributing to a deeper understanding of their electrochemical performance.

APPENDIX

Permissions

Figure 1.1 (Ref 25):
Springer Nature
License Number: 5766170302494

Figure 1.2 (Ref 55):
Elsevier
License Number: 5766170857730

Figure 1.4 (Ref 75):
Springer Nature
License Number: 5766180066967

Figure 1.5 (Ref 11):
Elsevier
License Number: 5766171341438

Figure 1.6 (Ref 83):
Creative Commons Attribution-NonCommercial 3.0 Unported Licence

Figure 1.7 (Ref 87):
Creative Commons Attribution Non-Commercial License

Figure 1.8 (Ref 89):
Creative Commons Attribution Non-Commercial License

Stress equations:

$$\varepsilon_r = \frac{1}{E}(\sigma_r - 2\nu\sigma_\theta) + \frac{1}{3}\Omega C \quad (1)$$

$$\varepsilon_\theta = \frac{1}{E}((1-\nu)\sigma_\theta - \nu\sigma_r) + \frac{1}{3}\Omega C \quad (2)$$

$$\frac{d\sigma_r}{dr} + \frac{\sigma_r - \sigma_\theta}{r} = 0 \quad (3)$$

$$\varepsilon_r = \frac{du}{dr} \quad (4)$$

$$\varepsilon_\theta = \frac{u}{r} \quad (5)$$

$$C_{s,ave}(r_1) = \frac{2}{(r_1^2 - R_1^2)} \int_{R_1}^{r_1} C_s \, r dr$$

6

Stress derivation:

$$\varepsilon_\theta = \frac{u}{r}$$

$$d\varepsilon_\theta = \frac{rdu - udr}{r^2} = \frac{du}{r} - \frac{udr}{r^2}$$

$$\frac{d\varepsilon_\theta}{dr} = \frac{1}{r}\frac{du}{dr} - \frac{u}{r^2}$$

$$\frac{d\varepsilon_\theta}{dr} = \frac{1}{r}\varepsilon_r - \frac{u}{r^2} = \frac{1}{r}\varepsilon_r - \frac{\varepsilon_\theta}{r} = \frac{\varepsilon_r - \varepsilon_\theta}{r}$$

Using 1 and 2

$$\frac{d\varepsilon_\theta}{dr} = \frac{1+\nu}{rE}(\sigma_r - \sigma_\theta) \quad (7)$$

$$\frac{d\varepsilon_\theta}{dr} = \frac{1}{E}\left(\frac{(1-\nu)d\sigma_\theta}{dr} - \frac{\nu d\sigma_r}{dr}\right) + \frac{1}{3}\Omega\frac{\mathrm{d}C_s}{dr}$$

$$\frac{1+\nu}{rE}(\sigma_r - \sigma_\theta) = \frac{1}{E}\left((1-\nu)\frac{d\sigma_\theta}{dr} - \nu\frac{d\sigma_r}{dr}\right) + \frac{1}{3}\Omega\frac{\mathrm{d}C_s}{dr}$$

Using 3

$$\frac{d\sigma_r}{dr} = -\frac{\sigma_r - \sigma_\theta}{r}$$

$$-\frac{rd\sigma_r}{dr} = \sigma_r - \sigma_\theta$$

$$\frac{1+\nu}{rE}\left(-\frac{rd\sigma_r}{dr}\right) = \frac{1}{E}\left((1-\nu)\frac{d\sigma_\theta}{dr} - \nu\frac{d\sigma_r}{dr}\right) + \frac{1}{3}\Omega\frac{\mathrm{d}C_s}{dr}$$

$$-\frac{1+\nu}{E}\left(\frac{d\sigma_r}{dr}\right) = \frac{(1-\nu)}{E}\frac{d\sigma_\theta}{dr} - \frac{\nu}{E}\frac{d\sigma_r}{dr} + \frac{1}{3}\Omega\frac{\mathrm{d}C_s}{dr}$$

$$\frac{\nu}{E}\frac{d\sigma_r}{dr} - \frac{1+\nu}{E}\left(\frac{d\sigma_r}{dr}\right) = \frac{(1-\nu)}{E}\frac{d\sigma_\theta}{dr} + \frac{1}{3}\Omega\frac{\mathrm{d}C_s}{dr}$$

$$-\frac{1}{E}\frac{d\sigma_r}{dr} = \frac{(1-\nu)}{E}\frac{d\sigma_\theta}{dr} + \frac{1}{3}\Omega\frac{\mathrm{d}C_s}{dr}$$

$$\frac{d\sigma_r}{dr} = -(1-\nu)\frac{d\sigma_\theta}{dr} - \frac{E\Omega}{3}\frac{\mathrm{d}C_s}{dr}$$

$$\sigma_r = -(1-\nu)\sigma_\theta - \frac{E\Omega}{3}C_s + contant_1$$

From 3

$$\frac{d\sigma_r}{dr} = -\frac{\sigma_r - \sigma_\theta}{r} \quad (8)$$

$$\frac{rd\sigma_r}{dr} = \sigma_\theta - \sigma_r$$

$$\frac{rd^2\sigma_r}{dr^2} + \frac{d\sigma_r}{dr} = \frac{d\sigma_\theta}{dr} - \frac{d\sigma_r}{dr}$$

$$\frac{rd^2\sigma_r}{dr^2} = \frac{d\sigma_\theta}{dr} - 2\frac{d\sigma_r}{dr}$$

Using 8

$$\frac{d\sigma_r}{dr} = -(1-\nu)\frac{d\sigma_\theta}{dr} - \frac{E\Omega}{3}\frac{\mathrm{d}C_s}{dr}$$

$$(1-\nu)\frac{d\sigma_\theta}{dr} = -\frac{d\sigma_r}{dr} - \frac{E\Omega}{3}\frac{\mathrm{d}C_s}{dr}$$

$$(1-\nu)\left(\frac{rd^2\sigma_r}{dr^2} + 2\frac{d\sigma_r}{dr}\right) = -\frac{d\sigma_r}{dr} - \frac{E\Omega}{3}\frac{\mathrm{d}C_s}{dr}$$

$$\frac{rd^2\sigma_r}{dr^2} + 2\frac{d\sigma_r}{dr} - \frac{r\nu d^2\sigma_r}{dr^2} - \frac{2\nu d\sigma_r}{dr} = -\frac{d\sigma_r}{dr} - \frac{E\Omega}{3}\frac{\mathrm{d}C_s}{dr}$$

$$r(1-\nu)\frac{d^2\sigma_r}{dr^2} - \frac{2\nu d\sigma_r}{dr} + 3\frac{d\sigma_r}{dr} = -\frac{E\Omega}{3}\frac{\mathrm{d}C_s}{dr}$$

$$r(1-\nu)\frac{d^2\sigma_r}{dr^2} + (3-2\nu)\frac{d\sigma_r}{dr} = -\frac{E\Omega}{3}\frac{\mathrm{d}C_s}{dr}$$

$$\int u\,dv = uv - \int v\,du$$

$$(1-\nu)\int r\frac{d^2\sigma_r}{dr^2}\,dr$$

$$(1-\nu)\left[r\frac{d\sigma_r}{dr} - \int\frac{d\sigma_r}{dr}dr\right] = (1-\nu)\left[r\frac{d\sigma_r}{dr} - \sigma_r\right]$$

$$(1-\nu)\left[r\frac{d\sigma_r}{dr} - \sigma_r\right] + (3-2\nu)\sigma_r = -\frac{E\Omega}{3}C_s + constant_2$$

$$(1-\nu)r\frac{d\sigma_r}{dr} + (2-\nu)\sigma_r = -\frac{E\Omega}{3}C_s + constant_2$$

$$(1-\nu)r\frac{d\sigma_r}{\sigma_r} + (2-\nu)dr = -\frac{E\Omega}{3}C_s\frac{dr}{\sigma_r} + \frac{dr}{\sigma_r}constant_2$$

$$(1-\nu)r^2\frac{d\sigma_r}{\sigma_r} + (2-\nu)dr = -\frac{E\Omega}{3}C_s\frac{rdr}{\sigma_r} + \frac{rdr}{\sigma_r}constant_2$$

$$(1-\nu)\int_{R_1}^{r_1} r^2\,d\sigma_r + (2-\nu)\int_{R_1}^{r_1}\sigma_r r\,d\sigma_r = -\frac{E\Omega}{3}\int_{R_1}^{r_1}C_s r\,dr + \int_{R_1}^{r_1} r\,dr\,constant_2$$

$$\int_{R_1}^{r_1} d[r^2\sigma_r] = \int_{R_1}^{r_1} r^2\,d\sigma_r + 2r\sigma_r dr$$

$$(1-\nu)\int_{R_1}^{r_1} r^2\,d\sigma_r + 2r\sigma_r dr - \nu\int_{R_1}^{r_1}\sigma_r r\,d\sigma_r = -\frac{E\Omega}{3}\int_{R_1}^{r_1}C_s r\,dr + \int_{R_1}^{r_1} r\,dr\,constant_2$$

$$(1-\nu)\left[r^2\sigma_r(r)|_{R_1}^{r_1}\right] - \nu\int_{R_1}^{r_1}\sigma_r r\,d\sigma_r = -\frac{E\Omega}{3}\left[\frac{r^2}{2}C_s(r)|_{R_1}^{r_1}\right] + \left[\frac{r^2}{2}|_{R_1}^{r_1}\right]constant_2$$

$$\sigma_r(R_1) = \sigma_r(R_2) = 0$$

$$(1-\nu)\left[r^2\sigma_r(r_1)\right] - \nu\int_{R_1}^{r_1}\sigma_r r\,d\sigma_r = -\frac{E\Omega}{3}\frac{(r_1^2 - R_1^2)}{2}C_{s,ave}(r_1) + \frac{(r_1^2 - R_1^2)}{2}constant_2$$

$$2(1-\nu)\left[r^2\sigma_r(r_1)\right] - 2\nu\int_{R_1}^{r_1}\sigma_r r\,d\sigma_r = -\frac{E\Omega}{3}(r_1^2 - R_1^2)C_{s,ave}(r_1) + (r_1^2 - R_1^2)constant_2$$

$$\sigma_{r,ave}(r_1) = \frac{2}{(r_1^2 - R_1^2)} \int_{R_1}^{r_1} \sigma_r r \, d\sigma_r$$

$$2(1-\nu)\,[r^2\sigma_r(r_1)] - \nu(r_1^2 - R_1^2)\sigma_{r,ave}(r_1) = -\frac{E\Omega}{3}(r_1^2 - R_1^2)C_{s,ave}(r_1) + (r_1^2 - R_1^2)constant_2$$

First pulse Li-ion concentration:

$$C_{\alpha 1} = \sum_{n=1}^{\infty} [\, a_{1n} J_0(\lambda_n r) + b_{1n} Y_0(\lambda_n r)]\, e^{-\lambda_n^2 D_\alpha t} + C_1 \ln(r) + C_2$$

$$C_{\alpha 2} = \sum_{m=1}^{\infty} [\, a_{1m} J_0(\lambda_m r) + b_{1m} Y_0(\lambda_m r)]\, e^{-\lambda_m^2 D_\alpha t} + C_3 \ln(r) + C_4$$

$$C_3 = \frac{i\rho_\alpha (R_2^2 - R_1^2)}{2FD_\alpha} = -\mathrm{C}_1$$

$$\frac{\partial C_{\alpha 1H}}{\partial r}|_{r=R_1} = 0$$

$$\frac{\partial C_{\alpha 1H}}{\partial r}|_{r=R_3} = 0$$

$$\frac{\partial C_{\alpha 2H}}{\partial r}|_{r=R_2} = 0$$

$$\frac{\partial C_{\alpha 2H}}{\partial r}|_{r=R_3} = 0$$

$$C_{\alpha 1}(t=0) = C_{\alpha 2}(t=0) = 0$$

$$C_{\alpha 1}(t, R_3) = C_{\alpha 2}(t, R_3)$$

λ_n derivation:

$$\frac{\partial C_{\alpha 1}}{\partial r}|_{r=R_1} = [\sum_{n=1}^{\infty} -\lambda_n [a_{1n} J_1(\lambda_n R_1) + b_{1n} Y_1(\lambda_n R_1)] e^{-\lambda_n^2 D_\alpha t}] + \frac{C_1}{R_1}$$

$$\frac{\partial C_{\alpha 1H}}{\partial r} = 0$$

$$[\sum_{n=1}^{\infty} -\lambda_n [a_{1n} J_1(\lambda_n R_3) + b_{1n} Y_1(\lambda_n R_3)] e^{-\lambda_n^2 D_\alpha t}] = 0$$

$$a_{1n} J_1(\lambda_n R_1) + b_{1n} Y_1(\lambda_n R_1) = 0$$

$$a_{1n} = \frac{-b_{1n} Y_1(\lambda_n R_1)}{J_1(\lambda_n R_1)}$$

$$\frac{Y_1(\lambda_n R_1)}{J_1(\lambda_n R_1)} J_1(\lambda_n R_3) + Y_1(\lambda_n R_3) = 0$$

10

λ_m derivation:

$$\frac{\partial C_{\alpha 2}}{\partial r}|_{r=R_3} = [\sum_{m=1}^{\infty} -\lambda_m [a_{2m} J_1(\lambda_m R_3) + b_{2m} Y_1(\lambda_m R_3)] e^{-\lambda_m^2 D_\alpha t}] + \frac{C_3}{R_3}$$

$$\frac{\partial C_{\alpha 2H}}{\partial r} = 0$$

$$[\sum_{n=1}^{\infty} -\lambda_m [a_{2m} J_1(\lambda_m R_2) + b_{2m} Y_1(\lambda_m R_2)] e^{-\lambda_m^2 D_\alpha t}] = 0$$

$$a_{2m} J_1(\lambda_m R_3) + b_{2m} Y_1(\lambda_m R_3) = 0$$

$$a_{2m} = \frac{-b_{2m} Y_1(\lambda_n R_2)}{J_1(\lambda_n R_2)}$$

$$\frac{Y_1(\lambda_m R_2)}{J_1(\lambda_m R_2)} J_1(\lambda_m R_3) + Y_1(\lambda_m R_3) = 0$$

b_{1n} derivation:

$$C_{\alpha 1} = \sum_{n=1}^{\infty} [a_{1n} J_0(\lambda_n r) + b_{1n} Y_0(\lambda_n r)] e^{-\lambda_n^2 D_\alpha t} + C_1 \ln(r) + C_2$$

$$C_{\alpha 1}(t = 0) = 0$$

$$\sum_{n=1}^{\infty} [a_{1n} J_0(\lambda_n r) + b_{1n} Y_0(\lambda_n r)] + C_1 \ln(r) = 0$$

$$a_{1n} J_0(\lambda_n r) + b_{1n} Y_0(\lambda_n r) = -C_1 \ln(r)$$

$$\frac{-b_{1n} Y_1(\lambda_n R_1)}{J_1(\lambda_n R_1)} J_0(\lambda_n r) + b_{1n} Y_0(\lambda_n r) = -C_1 \ln(r)$$

$$b_{1n} \left[\frac{-Y_1(\lambda_n R_1)}{J_1(\lambda_n R_1)} J_0(\lambda_n r) + Y_0(\lambda_n r)\right] = -C_1 \ln(r)$$

$$b_{1n} = \frac{-\int_{R_1}^{R_3} C_1 \ln(r) r \left[\frac{-Y_1(\lambda_n R_1)}{J_1(\lambda_n R_1)} J_0(\lambda_n r) + Y_0(\lambda_n r)\right] dr}{\int_{R_1}^{R_3} r \left[\frac{-Y_1(\lambda_n R_1)}{J_1(\lambda_n R_1)} J_0(\lambda_n r) + Y_0(\lambda_n r)\right]^2 dr}$$

Relating $C_{\alpha 1}$ and $C_{\alpha 2}$:

$$\frac{\partial C_{\alpha 1}}{\partial r}|_{r=R_3} = D_\alpha [\sum_{n=1}^{\infty} -\lambda_n [a_{1n} J_1(\lambda_n R_3) + b_{1n} Y_1(\lambda_n R_3)] e^{-\lambda_n^2 D_\beta t}] + \frac{C_1}{R_3}$$

$$C_1 = -C_3$$

$$\frac{\partial C_{\alpha 2}}{\partial r}|_{r=R_3} = D_\alpha [\sum_{m=1}^{\infty} -\lambda_m [a_{2m} J_1(\lambda_m R_3) + b_{2m} Y_1(\lambda_m R_3)] e^{-\lambda_m^2 D_\beta t}] + \frac{C_3}{R_3}$$

$$\frac{\partial C_{\alpha 1H}}{\partial r}|_{R_3} = \frac{\partial C_{\alpha 2H}}{\partial r}|_{R_3} = 0$$

$$C_{\alpha 1}(t, R_3) = C_{\alpha 2}(t, R_3)$$

Stress for second pulse onward:

$$r(1-\upsilon)\frac{d^2\sigma_r}{dr^2}+(3-2\upsilon)\frac{d\sigma_r}{dr}=\frac{-E\Omega}{3}\cdot\frac{dC_s}{dr}$$

$$(1-\upsilon)[r_1^2\sigma_r(r_1)]+\upsilon\int_{R_1}^{r_1}\sigma_r r dr=\frac{-E\Omega C_{s,ave}(r_1)(r_1^2-R_1^2)}{6}+\frac{C_1(r_1^2-R_1^2)}{2}$$

$$C_1=constant$$

$$(1-\upsilon)[r_2^2\sigma_r(r_2)]+\upsilon\int_{r_2}^{R_2}\sigma_r r dr=\frac{-E\Omega C_{s,ave}(r_2)(R_2^2-r_2^2)}{6}+\frac{C_2(R_2^2-r_2^2)}{2}$$

$$(1-\upsilon)[r_2^2\sigma_r(r_2)-r_1^2\sigma_r(r_1)]+\upsilon\int_{r_1}^{r_2}\sigma_r r dr=\frac{-E\Omega}{6}[C_{s,ave}(r_1)(r_2^2-r_1^2)]+\frac{C_1(r_1^2-R_1^2)}{2}$$

$$C_{s,ave}(r_1)=\frac{2}{(r_1^2-R_1^2)}\int_{R_1}^{r_1}C_s r dr$$

$$\sigma_{r,ave}(r_1)=\frac{2}{(r_1^2-R_1^2)}\int_{R_1}^{r_1}\sigma_r r dr$$

REFERENCE

[1] Li M, Lu J, Chen Z, Amine K. 30 Years of Lithium-Ion Batteries. Adv Mater 2018;30. https://doi.org/10.1002/ADMA.201800561.

[2] Energy Agency I. Global EV Outlook 2021 Accelerating ambitions despite the pandemic 2021.

[3] Zhang H, Yang Y, Ren D, Wang L, He X. Graphite as anode materials: Fundamental mechanism, recent progress and advances. Energy Storage Mater 2021;36:147–70. https://doi.org/10.1016/J.ENSM.2020.12.027.

[4] Thackeray MM, Wolverton C, Isaacs ED. Electrical energy storage for transportation—approaching the limits of, and going beyond, lithium-ion batteries. Energy Environ Sci 2012;5:7854–63. https://doi.org/10.1039/C2EE21892E.

[5] Eshetu GG, Figgemeier E. Confronting the Challenges of Next-Generation Silicon Anode-Based Lithium-Ion Batteries: Role of Designer Electrolyte Additives and Polymeric Binders. ChemSusChem 2019;12:2515–39. https://doi.org/10.1002/CSSC.201900209.

[6] Lambert F. Tesla confirms acquisition of battery startup in new patent - Electrek n.d. https://electrek.co/2021/11/05/tesla-confirms-acquisition-siilion-battery-startup-new-patent/ (accessed March 31, 2022).

[7] Goldman JL, Long BR, Gewirth AA, Nuzzo RG. Strain Anisotropies and Self-Limiting Capacities in Single-Crystalline 3D Silicon Microstructures: Models for High Energy Density Lithium-Ion Battery Anodes. Adv Funct Mater 2011;21:2412–22. https://doi.org/10.1002/ADFM.201002487.

[8] Li X, Zhang M, Yuan S, Lu C. Research Progress of Silicon/Carbon Anode Materials for

Lithium-Ion Batteries: Structure Design and Synthesis Method. ChemElectroChem 2020;7:4289–302. https://doi.org/10.1002/CELC.202001060.

[9] Zhu J, Mathews I, Ren D, Li W, Cogswell D, Xing B, et al. End-of-life or second-life options for retired electric vehicle batteries. Cell Reports Phys Sci 2021;2:100537. https://doi.org/10.1016/J.XCRP.2021.100537.

[10] Yim C-H, Niketic S, Salem N, Naboka O, Abu-Lebdeh Y. Towards Improving the Practical Energy Density of Li-Ion Batteries: Optimization and Evaluation of Silicon:Graphite Composites in Full Cells. J Electrochem Soc 2017;164:A6294–302. https://doi.org/10.1149/2.0481701JES/XML.

[11] Chae S, Ko M, Kim K, Ahn K, Cho J. Confronting Issues of the Practical Implementation of Si Anode in High-Energy Lithium-Ion Batteries. Joule 2017;1:47–60. https://doi.org/10.1016/J.JOULE.2017.07.006.

[12] Alhmoud H, Brodoceanu D, Elnathan R, Kraus T, Voelcker NH. A MACEing silicon: Towards single-step etching of defined porous nanostructures for biomedicine. Prog Mater Sci 2021;116:100636. https://doi.org/10.1016/J.PMATSCI.2019.100636.

[13] Toor F, Miller JB, Davidson LM, Nichols L, Duan W, Jura MP, et al. Nanostructured silicon via metal assisted catalyzed etch (MACE): chemistry fundamentals and pattern engineering. Nanotechnology 2016;27:412003. https://doi.org/10.1088/0957-4484/27/41/412003.

[14] Yuda AP, Koraag PYE, Iskandar F, Wasisto HS, Sumboja A. Advances of the top-down synthesis approach for high-performance silicon anodes in Li-ion batteries. J Mater Chem A 2021;9:18906–26. https://doi.org/10.1039/d1ta02711e.

[15] Artoni P, Pecora EF, Irrera A, Priolo F. Kinetics of si and ge nanowires growth through electron beam evaporation. Nanoscale Res Lett 2011;6:1–8. https://doi.org/10.1186/1556-276X-6-162/FIGURES/5.

[16] Leonardi AA, Faro MJ Lo, Irrera A. Silicon Nanowires Synthesis by Metal-Assisted Chemical Etching: A Review. Nanomater 2021, Vol 11, Page 383 2021;11:383. https://doi.org/10.3390/NANO11020383.

[17] Schmidt V, Wittemann J V., Senz S, Gósele U. Silicon nanowires: A review on aspects of their growth and their electrical properties. Adv Mater 2009;21:2681–702. https://doi.org/10.1002/ADMA.200803754.

[18] Ratke L, Voorhees PW. Growth and Coarsening: Ostwald Ripening in Material Processing - Lorenz Ratke, Peter W. Voorhees - Google Books. Springer Berlin Heidelberg; 2013.

[19] Den Hertog MI, Rouviere JL, Dhalluin F, Desré PJ, Gentile P, Ferret P, et al. Control of gold surface diffusion on Si nanowires. Nano Lett 2008;8:1544–50. https://doi.org/10.1021/NL073356I/ASSET/IMAGES/NL-2007-03356I_M007.GIF.

[20] Puglisi RA, Bongiorno C, Borgh G, Fazio E, Garozzo C, Mannino G, et al. Study on the Physico-Chemical Properties of the Si Nanowires Surface. Nanomater 2019, Vol 9, Page 818 2019;9:818. https://doi.org/10.3390/NANO9060818.

[21] Zhang F, Sautter K, Larsen AM, Findley DA, Davis RC, Samha H, et al. Chemical vapor deposition of three aminosilanes on silicon dioxide: Surface characterization, stability, effects of silane concentration, and cyanine dye adsorption. Langmuir 2010;26:14648–54. https://doi.org/10.1021/LA102447Y/SUPPL_FILE/LA102447Y_SI_001.PDF.

[22] Reyntjens S, Puers R. A review of focused ion beam applications in microsystemtechnology. J Micromechanics Microengineering 2001;11:287. https://doi.org/10.1088/0960-1317/11/4/301.

[23] Vu A, Qian Y, Stein A. Porous electrode materials for lithium-ion batteries-how to prepare them and what makes them special. Adv Energy Mater 2012;2:1056–85. https://doi.org/10.1002/aenm.201200320.

[24] Wang KX, Li XH, Chen JS. Surface and interface engineering of electrode materials for lithium-ion batteries. Adv Mater 2015;27:527–45. https://doi.org/10.1002/adma.201402962.

[25] Li X, Gu M, Hu S, Kennard R, Yan P, Chen X, et al. Mesoporous silicon sponge as an anti-pulverization structure for high-performance lithium-ion battery anodes. Nat Commun 2014 51 2014;5:1–7. https://doi.org/10.1038/ncomms5105.

[26] Ge M, Rong J, Fang X, Zhou C. Porous Doped Silicon Nanowires for Lithium Ion Battery Anode with Long Cycle Life 2012. https://doi.org/10.1021/nl300206e.

[27] Shen C, Ge M, Luo L, Fang X, Liu Y, Zhang A, et al. In Situ and Ex Situ TEM Study of Lithiation Behaviours of Porous Silicon Nanostructures. Sci Reports 2016 61 2016;6:1–11. https://doi.org/10.1038/srep31334.

[28] Song T, Hu L, Paik U. One-dimensional silicon nanostructures for Li ion batteries. J Phys Chem Lett 2014;5:720–31. https://doi.org/10.1021/jz4027979.

[29] Qu Y, Zhou H, Duan X. Porous silicon nanowires. Nanoscale 2011;3:4060–8. https://doi.org/10.1039/c1nr10668f.

[30] Zhong X, Qu Y, Lin YC, Liao L, Duan X. Unveiling the formation pathway of single

crystalline porous silicon nanowires. ACS Appl Mater Interfaces 2011;3:261–70. https://doi.org/10.1021/am1009056.

[31] Zhao D, Yang P, Huo Q, Chmelka BF, Stucky GD. Topological mesoporous materials. Solid Catal Porous Solids 1998;3:111–21. https://doi.org/10.1016/S1359-0286(98)80073-9.

[32] Xie Y, Kocaefe D, Chen C, Kocaefe Y. Review of Research on Template Methods for Nanomaterials. J Nanomater 2016;2016:1–10.

[33] Filsinger DH, Bourrie DB. Silica to Silicon: Key Carbothermic Reactions and Kinetics. J Am Ceram Soc 1990;73. https://doi.org/10.1111/j.1151-2916.1990.tb09820.x.

[34] Yoshikawa N, Kikuchi A, Taniguchi S. Anomalous Temperature Dependence of the Growth Rate of the Reaction Layer between Silica and Molten Aluminum. J Am Ceram Soc 2002;85:1827–34. https://doi.org/10.1111/J.1151-2916.2002.TB00360.X.

[35] Fang DL, Zhao YC, Wang SS, Hu TS, Zheng CH. Highly efficient synthesis of nano-Si anode material for Li-ion batteries by a ball-milling assisted low-temperature aluminothermic reduction. Electrochim Acta 2020;330:135346. https://doi.org/10.1016/J.ELECTACTA.2019.135346.

[36] Zhou ZW, Liu YT, Xie XM, Ye XY. Aluminothermic reduction enabled synthesis of silicon hollow microspheres from commercialized silica nanoparticles for superior lithium storage. Chem Commun 2016;52:8401–4. https://doi.org/10.1039/C6CC03766F.

[37] Cui J, Cui Y, Li S, Sun H, Wen Z, Sun J. Microsized Porous SiOx@C Composites Synthesized through Aluminothermic Reduction from Rice Husks and Used as Anode for Lithium-Ion Batteries. ACS Appl Mater Interfaces 2016;8:30239–47.

https://doi.org/10.1021/ACSAMI.6B10260/ASSET/IMAGES/LARGE/AM-2016-10260K_0006.JPEG.

[38] Mishra K, Zheng J, Patel R, Estevez L, Jia H, Luo L, et al. High performance porous Si@C anodes synthesized by low temperature aluminothermic reaction. Electrochim Acta 2018;269:509–16. https://doi.org/10.1016/J.ELECTACTA.2018.02.166.

[39] Hou L, Xing B, Kang W, Zeng H, Guo H, Cheng S, et al. Aluminothermic reduction synthesis of porous silicon nanosheets from vermiculite as high-performance anode materials for lithium-ion batteries. Appl Clay Sci 2022;218:106418. https://doi.org/10.1016/J.CLAY.2022.106418.

[40] Wang D, Zhang D, Dong Y, Lin X, Liu R, Li A, et al. Reconstructed Nano-Si Assembled Microsphere via Molten Salt-Assisted Low-Temperature Aluminothermic Reduction of Diatomite as High-Performance Anodes for Lithium-Ion Batteries. ACS Appl Energy Mater 2021;4:6146–53. https://doi.org/10.1021/ACSAEM.1C00938/ASSET/IMAGES/LARGE/AE1C00938_0006.JPEG.

[41] Lin N, Han Y, Zhou J, Zhang K, Xu T, Zhu Y, et al. A low temperature molten salt process for aluminothermic reduction of silicon oxides to crystalline Si for Li-ion batteries. Energy Environ Sci 2015;8:3187–91. https://doi.org/10.1039/C5EE02487K.

[42] Tang Y, Yuan S, Guo Y, Huang R, Wang J, Yang B, et al. Highly Ordered Mesoporous Si/C Nanocomposite as High Performance Anode Material for Li-ion Batteries. Electrochim Acta 2016;200:182–8. https://doi.org/10.1016/j.electacta.2016.03.085.

[43] Wen Z, Lu G, Mao S, Kim H, Cui S, Yu K, et al. Silicon nanotube anode for lithium-ion

batteries. Electrochem Commun 2013;29:67–70. https://doi.org/10.1016/j.elecom.2013.01.015.

[44] Hong I, Scrosati B, Croce F. Mesoporous, Si/C composite anode for Li battery obtained by “magnesium-thermal” reduction process. Solid State Ionics 2013;232:24–8. https://doi.org/10.1016/j.ssi.2012.11.003.

[45] Bao Z, Weatherspoon MR, Shian S, Cai Y, Graham PD, Allan SM, et al. Chemical reduction of three-dimensional silica micro-assemblies into microporous silicon replicas. Nature 2007;446:172–5. https://doi.org/10.1038/nature05570.

[46] Zhou Y, Tian Z, Fan R, Zhao S, Zhou R, Guo H, et al. Scalable synthesis of Si/SiO2@C composite from micro-silica particles for high performance lithium battery anodes. Powder Technol 2015;284:365–70. https://doi.org/10.1016/j.powtec.2015.07.007.

[47] Du Y, Zhu G, Wang K, Wang Y, Wang C, Xia Y. Si/graphene composite prepared by magnesium thermal reduction of SiO 2 as anode material for lithium-ion batteries. Electrochem Commun 2013;36:107–10. https://doi.org/10.1016/j.elecom.2013.09.019.

[48] Shi L, Wang W, Wang A, Yuan K, Yang Y. Understanding the impact mechanism of the thermal effect on the porous silicon anode material preparation via magnesiothermic reduction. J Alloys Compd 2016;661:27–37. https://doi.org/10.1016/j.jallcom.2015.11.196.

[49] Wang W, Favors Z, Ionescu R, Ye R, Bay HH, Ozkan M, et al. Monodisperse porous silicon spheres as anode materials for lithium ion batteries. Sci Rep 2015;5:2–7. https://doi.org/10.1038/srep08781.

[50] Wu L, Yang J, Zhou X, Zhang M, Ren Y, Nie Y. Silicon nanoparticles embedded in a

porous carbon matrix as a high-performance anode for lithium-ion batteries. J Mater Chem A 2016;4:11381–7. https://doi.org/10.1039/c6ta04398d.

[51] Shivaraju GC, Sudakar C, Prakash AS. High-rate and long-cycle life performance of nano-porous nano-silicon derived from mesoporous MCM-41 as an anode for lithium-ion battery. Electrochim Acta 2019;294:357–64. https://doi.org/10.1016/j.electacta.2018.10.122.

[52] Kang W, Kim JC, Kim DW. Waste glass microfiber filter-derived fabrication of fibrous yolk-shell structured silicon/carbon composite freestanding electrodes for lithium-ion battery anodes. J Power Sources 2020;468:228407. https://doi.org/10.1016/j.jpowsour.2020.228407.

[53] Lai Y, Thompson JR, Dasog M. Metallothermic Reduction of Silica Nanoparticles to Porous Silicon for Drug Delivery Using New and Existing Reductants. Chem - A Eur J 2018;24:7913–20. https://doi.org/10.1002/chem.201705818.

[54] Feng K, Li M, Liu W, Kashkooli AG, Xiao X, Cai M, et al. Silicon-Based Anodes for Lithium-Ion Batteries: From Fundamentals to Practical Applications. Small 2018;14. https://doi.org/10.1002/SMLL.201702737.

[55] Xu ZL, Cao K, Abouali S, Akbari Garakani M, Huang J, Huang JQ, et al. Study of lithiation mechanisms of high performance carbon-coated Si anodes by in-situ microscopy. Energy Storage Mater 2016;3:45–54. https://doi.org/10.1016/J.ENSM.2016.01.003.

[56] Ng SH, Wang J, Wexler D, Chew SY, Liu HK. Amorphous Carbon-Coated Silicon Nanocomposites: A Low-Temperature Synthesis via Spray Pyrolysis and Their

Application as High-Capacity Anodes for Lithium-Ion Batteries 2007. https://doi.org/10.1021/jp072778d.

[57] Qi ZY, Dai LQ, Wang ZF, Xie LJ, Chen JP, Cheng JY, et al. Optimizing the carbon coating to eliminate electrochemical interface polarization in a high performance silicon anode for use in a lithium-ion battery. Xinxing Tan Cailiao/New Carbon Mater 2022;37:245–58. https://doi.org/10.1016/S1872-5805(22)60580-8.

[58] Liu Y, Wen ZY, Wang XY, Hirano A, Imanishi N, Takeda Y. Electrochemical behaviors of Si/C composite synthesized from F-containing precursors. J Power Sources 2009;189:733–7. https://doi.org/10.1016/J.JPOWSOUR.2008.08.016.

[59] Qi C, Li S, Yang Z, Xiao Z, Zhao L, Yang F, et al. Suitable thickness of carbon coating layers for silicon anode. Carbon N Y 2022;186:530–8. https://doi.org/10.1016/J.CARBON.2021.10.062.

[60] Lu Q, Jeong B gon, Peng X, Jeong SW, Xie B, Wu Z. The robust carbon shell to improve stability of porous Si anodes for high-performance lithium-ion batteries. J Alloys Compd 2021;877:160193. https://doi.org/10.1016/J.JALLCOM.2021.160193.

[61] Xu ZL, Gang Y, Garakani MA, Abouali S, Huang JQ, Kim JK. Carbon-coated mesoporous silicon microsphere anodes with greatly reduced volume expansion. J Mater Chem A 2016;4:6098–106. https://doi.org/10.1039/C6TA01344A.

[62] Wang Y, Xu H, Chen X, Jin H, Wang J. Novel constructive self-healing binder for silicon anodes with high mass loading in lithium-ion batteries. Energy Storage Mater 2021;38:121–9. https://doi.org/10.1016/J.ENSM.2021.03.003.

[63] Ma X, Liu M, Gan L, Tripathi PK, Zhao Y, Zhu D, et al. Novel mesoporous Si@C

microspheres as anodes for lithium-ion batteries. Phys Chem Chem Phys 2014;16:4135–42. https://doi.org/10.1039/C3CP54507E.

[64] Jia H, Zheng J, Song J, Luo L, Yi R, Estevez L, et al. A novel approach to synthesize micrometer-sized porous silicon as a high performance anode for lithium-ion batteries. Nano Energy 2018;50:589–97. https://doi.org/10.1016/J.NANOEN.2018.05.048.

[65] Chae S, Choi SH, Kim N, Sung J, Cho J. Integration of Graphite and Silicon Anodes for the Commercialization of High-Energy Lithium-Ion Batteries. Angew Chemie - Int Ed 2020;59:110–35. https://doi.org/10.1002/ANIE.201902085.

[66] Li X, Yan P, Xiao X, Woo JH, Wang C, Liu J, et al. Design of porous Si/C–graphite electrodes with long cycle stability and controlled swelling. Energy Environ Sci 2017;10:1427–34. https://doi.org/10.1039/C7EE00838D.

[67] Choi SH, Nam G, Chae S, Kim D, Kim N, Kim WS, et al. Robust Pitch on Silicon Nanolayer–Embedded Graphite for Suppressing Undesirable Volume Expansion. Adv Energy Mater 2019;9:1–9. https://doi.org/10.1002/aenm.201803121.

[68] Jo H, Kim J, Nguyen DT, Kang KK, Jeon DM, Yang AR, et al. Stabilizing the solid electrolyte interphase layer and cycling performance of silicon-graphite battery anode by using a binary additive of fluorinated carbonates. J Phys Chem C 2016;120:22466–75. https://doi.org/10.1021/acs.jpcc.6b07570.

[69] Li M, Hou X, Sha Y, Wang J, Hu S, Liu X, et al. Facile spray-drying/pyrolysis synthesis of core-shell structure graphite/silicon-porous carbon composite as a superior anode for Li-ion batteries. J Power Sources 2014;248:721–8. https://doi.org/10.1016/j.jpowsour.2013.10.012.

[70] Li X, Yang D, Hou X, Shi J, Peng Y, Yang H. Scalable preparation of mesoporous Silicon@C/graphite hybrid as stable anodes for lithium-ion batteries. J Alloys Compd 2017;728:1–9. https://doi.org/10.1016/j.jallcom.2017.08.244.

[71] Li P, Hwang JY, Sun YK. Nano/microstructured silicon-graphite composite anode for high-energy-density li-ion battery. ACS Nano 2019;13:2624–33. https://doi.org/10.1021/acsnano.9b00169.

[72] Park MH, Kim MG, Joo J, Kim K, Kim J, Ahn S, et al. Silicon nanotube battery anodes. Nano Lett 2009;9:3844–7. https://doi.org/10.1021/nl902058c.

[73] Jia H, Li X, Song J, Zhang X, Luo L, He Y, et al. Hierarchical porous silicon structures with extraordinary mechanical strength as high-performance lithium-ion battery anodes. Nat Commun 2020 111 2020;11:1–9. https://doi.org/10.1038/s41467-020-15217-9.

[74] Xiang H, Zhang K, Ji G, Lee JY, Zou C, Chen X, et al. Graphene/nanosized silicon composites for lithium battery anodes with improved cycling stability. Carbon N Y 2011;49:1787–96. https://doi.org/10.1016/j.carbon.2011.01.002.

[75] Sung J, Kim N, Ma J, Hyeon Lee J, Hun Joo S, Lee T, et al. Subnano-sized silicon anode via crystal growth inhibition mechanism and its application in a prototype battery pack n.d. https://doi.org/10.1038/s41560-021-00945-z.

[76] Profatilova I, De Vito E, Genies S, Vincens C, Gutel E, Fanget O, et al. Impact of Silicon/Graphite Composite Electrode Porosity on the Cycle Life of 18650 Lithium-Ion Cell. ACS Appl Energy Mater 2020;3:11873–85. https://doi.org/10.1021/ACSAEM.0C01999/SUPPL_FILE/AE0C01999_SI_001.PDF.

[77] Lee D, Kondo A, Lee S, Myeong S, Sun S, Hwang I, et al. Controlled swelling behavior

and stable cycling of silicon/graphite granular composite for high energy density in lithium ion batteries. J Power Sources 2020;457:228021. https://doi.org/10.1016/J.JPOWSOUR.2020.228021.

[78] Yazami R, Touzain P. A reversible graphite-lithium negative electrode for electrochemical generators. J Power Sources 1983;9:365–71. https://doi.org/10.1016/0378-7753(83)87040-2.

[79] Bresser D, Paillard E, Passerini S. Advances in Batteries for Medium and Large-Scale Energy Storage. 1st ed. Elsevier; 2014.

[80] Asenbauer J, Eisenmann T, Kuenzel M, Kazzazi A, Chen Z, Bresser D. The success story of graphite as a lithium-ion anode material - fundamentals, remaining challenges, and recent developments including silicon (oxide) composites. Sustain Energy Fuels 2020;4:5387–416. https://doi.org/10.1039/d0se00175a.

[81] Qi Y, Guo H, Hector LG, Timmons A. Threefold Increase in the Young's Modulus of Graphite Negative Electrode during Lithium Intercalation. J Electrochem Soc 2010;157:A558. https://doi.org/10.1149/1.3327913/XML.

[82] Van Der Ven A, Bhattacharya J, Belak AA. Understanding Li diffusion in Li-intercalation compounds. Acc Chem Res 2013;46:1216–25. https://doi.org/10.1021/AR200329R.

[83] Sole C, Drewett NE, Hardwick LJ. In situ Raman study of lithium-ion intercalation into microcrystalline graphite. Faraday Discuss 2014;172:223–37. https://doi.org/10.1039/C4FD00079J.

[84] Mcdowell MT, Lee WS, Nix WD, Cui Y, Mcdowell MT, Lee SW, et al. 25th Anniversary Article: Understanding the Lithiation of Silicon and Other Alloying Anodes for Lithium-

Ion Batteries. Adv Mater 2013;25:4966–85. https://doi.org/10.1002/ADMA.201301795.

[85] Beaulieu LY, Eberman KW, Turner RL, Krause LJ, Dahna JR. Colossal reversible volume changes in lithium alloys. Electrochem Solid-State Lett 2001;4:A137. https://doi.org/10.1149/1.1388178/XML.

[86] Weng L, Xu C, Chen B, Zhou J, Cai R, Wang F. Theoretical analysis of the mechanical behavior in Li–ion battery cylindrical electrodes with phase transformation. Acta Mech 2020;231:1045–62. https://doi.org/10.1007/s00707-019-02589-3.

[87] Luo L, Wu J, Luo J, Huang J, Dravid VP. Dynamics of electrochemical lithiation/delithiation of graphene- encapsulated silicon nanoparticles studied by in-situ TEM. Sci Rep 2014;4:1–7. https://doi.org/10.1038/srep03863.

[88] Churikov A V., Ivanishchev A V., Ushakov A V., Romanova VO. Diffusion aspects of lithium intercalation as applied to the development of electrode materials for lithium-ion batteries. J Solid State Electrochem 2014;18:1425–41. https://doi.org/10.1007/s10008-013-2358-y.

[89] Kim J, Park S, Hwang S, Yoon WS. Principles and Applications of Galvanostatic Intermittent Titration Technique for Lithium-ion Batteries. J Electrochem Sci Technol 2022;13:19–31. https://doi.org/10.33961/jecst.2021.00836.

[90] Verma A, Smith K, Santhanagopalan S, Abraham D, Yao KP, Mukherjee PP, et al. Galvanostatic Intermittent Titration and Performance Based Analysis of LiNi 0.5 Co 0.2 Mn 0.3 O 2 Cathode . J Electrochem Soc 2011;164:A3380–92. https://doi.org/10.1149/2.1701713jes.

[91] Zhu Y, Wang C. Galvanostatic intermittent titration technique for phase-transformation

electrodes. J Phys Chem C 2010;114:2830–41. https://doi.org/10.1021/jp9113333.

[92] Pan K, Zou F, Canova M, Zhu Y, Kim JH. Systematic electrochemical characterizations of Si and SiO anodes for high-capacity Li-Ion batteries. J Power Sources 2019;413:20–8. https://doi.org/10.1016/J.JPOWSOUR.2018.12.010.

[93] Li P, Chen G, Zhang N, Ma R, Liu X. β-cyclodextrin as Lithium-ion Diffusion Channel with Enhanced Kinetics for Stable 2020:72–80. https://doi.org/10.1002/eem2.12092.

[94] Fang J Bin, Chang SZ, Ren Q, Zi TQ, Wu D, Li AD. Tailoring Stress and Ion-Transport Kinetics via a Molecular Layer Deposition-Induced Artificial Solid Electrolyte Interphase for Durable Silicon Composite Anodes. ACS Appl Mater Interfaces 2021;13:32520–30. https://doi.org/10.1021/acsami.1c07572.

[95] Wang Q, Meng T, Li Y, Yang J, Huang B, Ou S, et al. Consecutive chemical bonds reconstructing surface structure of silicon anode for high-performance lithium-ion battery. Energy Storage Mater 2021;39:354–64. https://doi.org/10.1016/J.ENSM.2021.04.043.

[96] Zhang H, Braun P V. Three-dimensional metal scaffold supported bicontinuous silicon battery anodes. Nano Lett 2012;12:2778–83. https://doi.org/10.1021/NL204551M/SUPPL_FILE/NL204551M_SI_001.PDF.

[97] Ko JY, Varini M, Klett M, Ekström H, Lindbergh G. Porous Electrode Model with Particle Stress Effects for Li(Ni 1/3 Co 1/3 Mn 1/3)O 2 Electrode . J Electrochem Soc 2019;166:A2939–49. https://doi.org/10.1149/2.0661913jes.

[98] Tang M, Huang HY, Meethong N, Kao YH, Carter WC, Chiang YM. Model for the particle size, overpotential, and strain dependence of phase transition pathways in storage electrodes: application to nanoscale olivines. Chem Mater 2009;21:1557–71.

https://doi.org/10.1021/CM803172S/ASSET/IMAGES/LARGE/CM-2008-03172S_0015.JPEG.

[99] Hu B, Jiang S, Shkrob IA, Zhang J, Trask SE, Polzin BJ, et al. Understanding of pre-lithiation of poly(acrylic acid) binder: Striking the balances between the cycling performance and slurry stability for silicon-graphite composite electrodes in Li-ion batteries. J Power Sources 2019;416:125–31. https://doi.org/10.1016/j.jpowsour.2019.01.068.

[100] LFA 1000 - Graphite - Thermal diffusivity. Linseis n.d. https://www.linseis.com/en/applications/research-development-academia/lfa-1000-graphite-thermal-conductivity/ (accessed June 3, 2022).

[101] Bai S, Bao W, Qian K, Li W, Sayahpour B, Sreenarayanan B, et al. Elucidating the Role of Prelithiation in Si-based Anodes for Interface. Adv Energy Mater 2023;13:2301041.

[102] Ciriminna R, Sciortino M, Alonzo G, De Schrijver A, Pagliaro M. From molecules to systems: Sol-gel microencapsulation in silica-based materials. Chem Rev 2011;111:765–89. https://doi.org/10.1021/CR100161X/ASSET/IMAGES/MEDIUM/CR-2010-00161X_0040.GIF.

[103] Lei Q, Guo J, Noureddine A, Wang A, Wuttke S, Brinker CJ, et al. Sol–Gel-Based Advanced Porous Silica Materials for Biomedical Applications. Adv Funct Mater 2020;30:1909539. https://doi.org/10.1002/ADFM.201909539.

[104] Niu D, Ma Z, Li Y, Shi J. Synthesis of core-shell structured dual-mesoporous silica spheres with tunable pore size and controllable shell thickness. J Am Chem Soc 2010;132:15144–7. https://doi.org/10.1021/ja1070653.

[105] Liu J, Hartono SB, Jin YG, Li Z, Lu GQ, Qiao SZ. A facile vesicle template route to multi-shelled mesoporous silica hollow nanospheres. J Mater Chem 2010;20:4595–601. https://doi.org/10.1039/B925201K/.

[106] Le Y, Guo D, Cheng B, Yu J. Bio-template-assisted synthesis of hierarchically hollow SiO2 microtubes and their enhanced formaldehyde adsorption performance. Appl Surf Sci 2013;274:110–6. https://doi.org/10.1016/J.APSUSC.2013.02.123.

[107] Yaya L, Cong Y, Lianping S, Qiuyang C, Shitao Y, Lu L. Rough-surface hydroxyl-group-rich hollow mesoporous silica nanospheres with nanocellulose as a template to improve the oxidation stability of bio-oil. Biomass and Bioenergy 2021;154:106243. https://doi.org/10.1016/J.BIOMBIOE.2021.106243.

[108] Witoon T, Chareonpanich M. Synthesis of hierarchical meso-macroporous silica monolith using chitosan as biotemplate and its application as polyethyleneimine support for CO2 capture. Mater Lett 2012;81:181–4. https://doi.org/10.1016/J.MATLET.2012.04.126.

[109] Trache D, Hussin MH, Haafiz MKM, Thakur VK. Recent progress in cellulose nanocrystals: Sources and production. Nanoscale 2017;9:1763–86. https://doi.org/10.1039/c6nr09494e.

[110] Habibi Y, Lucia LA, Rojas OJ. Cellulose nanocrystals: Chemistry, self-assembly, and applications. Chem Rev 2010;110:3479–500. https://doi.org/10.1021/cr900339w.

[111] Brinker CJ, Scherer GW. Sol-Gel Science: The Physics and Chemistry of Sol-Gel Processing. Elsevier Inc.; 2013. https://doi.org/10.1016/C2009-0-22386-5.

[112] Milea CA, Bogatu C, Duţă A. THE INFLUENCE OF PARAMETERS IN SILICA SOL-GEL PROCESS. Bull Transilv Univ Braşov Ser I Eng Sci • 2011;4.

[113] Teng Z, Han Y, Li J, Yan F, Yang W. Preparation of hollow mesoporous silica spheres by a sol–gel/emulsion approach. Microporous Mesoporous Mater 2010;127:67–72. https://doi.org/10.1016/J.MICROMESO.2009.06.028.

[114] Issa AA, Luyt AS. Kinetics of Alkoxysilanes and Organoalkoxysilanes Polymerization: A Review. Polym 2019, Vol 11, Page 537 2019;11:537. https://doi.org/10.3390/POLYM11030537.

[115] Voronkov MG, Yuzhelevskii YA, Mileshkevich VP. The Siloxane Bond and Its Influence on the Structure and Physical Properties of Organosilicon Compounds. Russ Chem Rev 1975;44:355–72. https://doi.org/10.1070/RC1975V044N04ABEH002273/XML.

[116] Aelion R, Loebel A, Eirich F. Hydrolysis of Ethyl Silicate. J Am Chem Soc 1950;72:5705–12. https://doi.org/10.1021/JA01168A090/ASSET/JA01168A090.FP.PNG_V03.

[117] Zhao T, Chen L, Lin R, Zhang P, Lan K, Zhang W, et al. Interfacial Assembly Directed Unique Mesoporous Architectures: From Symmetric to Asymmetric. Accounts Mater Res 2020;1:100–14. https://doi.org/10.1021/ACCOUNTSMR.0C00028/ASSET/IMAGES/MEDIUM/MR0C00028_0012.GIF.

[118] Brinker CJ, Scherer GW. Hydrolysis and Condensation II Silicates. Sol-Gel Sci. Phys. Chem. Sol-Gel Process., 1990.

[119] Danks AE, Hall SR, Schnepp Z. The evolution of 'sol–gel' chemistry as a technique for materials synthesis. Mater Horizons 2016;3:91–112. https://doi.org/10.1039/C5MH00260E.

[120] Buckley AM, Greenblatt M. The Sol-Gel Preparation of Silica Gels. J Chem Educ 1994;71:599–602. https://doi.org/10.1021/ED071P599.

[121] Luo L, Zhao P, Yang H, Liu B, Zhang JG, Cui Y, et al. Surface Coating Constraint Induced Self-Discharging of Silicon Nanoparticles as Anodes for Lithium Ion Batteries. Nano Lett 2015;15:7016–22. https://doi.org/10.1021/ACS.NANOLETT.5B03047/SUPPL_FILE/NL5B03047_SI_007.AVI.

[122] Wu SH, Lin HP. Synthesis of mesoporous silica nanoparticles. Chem Soc Rev 2013;42:3862–75. https://doi.org/10.1039/C3CS35405A.

[123] Lin HP, Mou CY, Singh LP, Bhattacharyya SK, Kumar R, Mishra G, et al. Structural and morphological control of cationic surfactant-templated mesoporous silica. Acc Chem Res 2002;214:927–35. https://doi.org/10.1021/ar000074f.

[124] Wu SH, Lin HP. Synthesis of mesoporous silica nanoparticles. Chem Soc Rev 2013;42:3862–75. https://doi.org/10.1039/c3cs35405a.

[125] Iler RK. The chemistry of silica; Sollubility, polymerization, colloid and surface properties and biochemistry. The occurrence, dissolution and deposition of silica. Wiley New York 1979:602.

[126] Foster EJ, Moon RJ, Agarwal UP, Bortner MJ, Bras J, Camarero-Espinosa S, et al. Current characterization methods for cellulose nanomaterials. Chem Soc Rev 2018;47:2609–79. https://doi.org/10.1039/c6cs00895j.

[127] Abitbol T, Marway H, Cranston E. Surface modification of cellulose nanocrystals with cetyltrimethylammonium bromide. Nord Pulp Pap Res J 2014;29:46–57.

https://doi.org/10.3183/npprj-2014-29-01-p046-057.

[128] Zhu X, Yang Y, Zheng Z, Xiang B, Cui X. Multiwave rheology and dynamic light scattering characterizations for a two-step sol-gel transition of tetraethoxysilane hydrolysis and condensation. J Sol-Gel Sci Technol 2018;88:255–62. https://doi.org/10.1007/S10971-018-4788-6/FIGURES/5.

[129] Lin HP, Mou CY. Structural and morphological control of cationic surfactant-templated mesoporous silica. Acc Chem Res 2002;35:927–35. https://doi.org/10.1021/ar000074f.

[130] Choi DG, Yang SM. Effect of two-step sol–gel reaction on the mesoporous silica structure. J Colloid Interface Sci 2003;261:127–32. https://doi.org/10.1016/S0021-9797(03)00020-1.

[131] Roik N V., Belyakova LA. Sol–gel synthesis of MCM-41 silicas and selective vapor-phase modification of their surface. J Solid State Chem 2013;207:194–202. https://doi.org/10.1016/J.JSSC.2013.09.027.

[132] Nishiyama N, Park DH, Koide A, Egashira Y, Ueyama K. A mesoporous silica (MCM-48) membrane: preparation and characterization. J Memb Sci 2001;182:235–44. https://doi.org/10.1016/S0376-7388(00)00570-6.

[133] Zhang W, Zheng N, Chen L, Xie L, Cui M, Li S, et al. Effect of Shape on Mesoporous Silica Nanoparticles for Oral Delivery of Indomethacin. Pharmaceutics 2019;11. https://doi.org/10.3390/PHARMACEUTICS11010004.

[134] Wan Y, Yang Z, Xiong G, Raman SR, Luo H. Bacterial celluloselated synthesis of free-standing silica nanotubes with a three-dimensional network structure. RSC Adv 2015;5:48875–80. https://doi.org/10.1039/c5ra08658b.

[135] Mahendran L, Ravichandran A, Ballamurugan AM. Organic and Inorganic Template-Assisted Synthesis of Silica Nanotubes and Evaluation of Their Properties. Appl Biochem Biotechnol 2022;194:167–75. https://doi.org/10.1007/S12010-021-03740-4/TABLES/1.

[136] Song JC, Xue FF, Zhang XX, Lu ZY, Sun ZY. Synthesis of yolk–shell mesoporous silica nanoparticles via a facile one-pot approach. Chem Commun 2017;53:3761–4. https://doi.org/10.1039/C7CC01424D.

[137] Liu J, Wang C, Wang X, Wang X, Cheng L, Li Y, et al. Mesoporous Silica Coated Single-Walled Carbon Nanotubes as a Multifunctional Light-Responsive Platform for Cancer Combination Therapy. Adv Funct Mater 2015;25:384–92. https://doi.org/10.1002/ADFM.201403079.

[138] Rana VK, Park SS, Parambadath S, Kim MJ, Kim SH, Mishra S, et al. Hierarchical mesoporous bio-polymer/ silica composites co-templated by trimethyl chitosan and a surfactant for controlled drug delivery. Medchemcomm 2011;2:1162–6. https://doi.org/10.1039/C0MD00222D.

[139] Shen D, Dai Y, Han J, Gan L, Liu J, Long M. A nanocellulose template strategy for the controllable synthesis of tungsten-containing mesoporous silica for ultra-deep oxidative desulfurization. Chem Eng J 2018;332:563–71. https://doi.org/10.1016/J.CEJ.2017.09.087.

[140] Albert K, Huang XC, Hsu HY. Bio-templated silica composites for next-generation biomedical applications. Adv Colloid Interface Sci 2017;249:272–89. https://doi.org/10.1016/J.CIS.2017.04.011.

[141] Quan G, Pan X, Wang Z, Wu Q, Li G, Dian L, et al. Lactosaminated mesoporous silica

nanoparticles for asialoglycoprotein receptor targeted anticancer drug delivery. J Nanobiotechnology 2015;13:1–12. https://doi.org/10.1186/S12951-015-0068-6/TABLES/1.

[142] Zheng T, Clemons CM, Pilla S. Grafting PEG on cellulose nanocrystals via polydopamine chemistry and the effects of PEG graft length on the mechanical performance of composite film. Carbohydr Polym 2021;271:118405. https://doi.org/10.1016/J.CARBPOL.2021.118405.

[143] Mawhinney DB, Glass JA, Yates JT. FTIR study of the oxidation of porous silicon. J Phys Chem B 1997;101:1202–6. https://doi.org/10.1021/jp963322r.

[144] Beganskienė A, Sirutkaitis V, Juškėnas R, Kareiva A, Kurtinaitienė M. FTIR, TEM and NMR investigations of stöber silica nanoparticles Controlled micromachining using LIBS View project Layered double hydroxides-NANOCONCOR View project FTIR, TEM and NMR Iinvestigations of Stöber Silica Nanoparticles. Mater Sci 2004;10.

[145] D'Acierno F, Hamad WY, Michal CA, MacLachlan MJ. Sustainable biochars from carbonization of cellulose filaments and nanocrystals. Bioresour Technol Reports 2021;16:100838. https://doi.org/10.1016/J.BITEB.2021.100838.

[146] Socrates G. Infrared and Raman Characteristic Group Frequencies: Tables and Charts by Socrates, George: Very Good Spiral-bound (2004) | WeBuyBooks. 3rd Editio. John Wiley & Sons Inc, United States; 2004.

[147] Yan N, Wang F, Zhong H, Li Y, Wang Y, Hu L, et al. Hollow Porous SiO2 Nanocubes Towards High-performance Anodes for Lithium-ion Batteries. Sci Reports 2013 31 2013;3:1–6. https://doi.org/10.1038/srep01568.

[148] Wang K, Luo S, Wu Y, He X, Zhao F, Wang J, et al. Super-Aligned Carbon Nanotube Films as Current Collectors for Lightweight and Flexible Lithium Ion Batteries. Adv Funct Mater 2013;23:846–53. https://doi.org/10.1002/ADFM.201202412.

[149] Ronan O, Roy A, Ryan S, Hughes L, Downing C, Jones L, et al. Templated Synthesis of SiO2Nanotubes for Lithium-Ion Battery Applications: An In Situ (Scanning) Transmission Electron Microscopy Study. ACS Omega 2022;8:925. https://doi.org/10.1021/ACSOMEGA.2C06298/SUPPL_FILE/AO2C06298_SI_002.MP4.

[150] Lepooivre F, Larcher D, Tarascon J-M. Electrochemical Activation of Silica for Enhanced Performances of Si-Based Electrodes. J Electrochem Soc 2016;163:2791–6. https://doi.org/10.1149/2.1221613jes.

[151] Liu XH, Wang JW, Huang S, Fan F, Huang X, Liu Y, et al. In situ atomic-scale imaging of electrochemical lithiation in silicon. Nat Nanotechnol 2012;7:749–56. https://doi.org/10.1038/nnano.2012.170.

[152] Liu R, Shen C, Dong Y, Qin J, Wang Q, Iocozzia J, et al. Sandwich-like CNTs/Si/C nanotubes as high performance anode materials for lithium-ion batteries. J Mater Chem A 2018;6:14797–804. https://doi.org/10.1039/c8ta04686g.

[153] Nemaga AW, Mallet J, Michel J, Guery C, Molinari M, Morcrette M. All electrochemical process for synthesis of Si coating on TiO2 nanotubes as durable negative electrode material for lithium ion batteries. J Power Sources 2018;393:43–53. https://doi.org/10.1016/j.jpowsour.2018.04.093.

[154] Wang C, Yang C, Zheng Z. Toward Practical High-Energy and High-Power Lithium Battery Anodes: Present and Future. Adv Sci 2022;9:2105213.

https://doi.org/10.1002/ADVS.202105213.

[155] Sakabe J, Ohta N, Ohnishi T, Mitsuishi K, Takada K. Porous amorphous silicon film anodes for high-capacity and stable all-solid-state lithium batteries. Commun Chem 2018 11 2018;1:1–9. https://doi.org/10.1038/s42004-018-0026-y.

[156] Chen Z, Danilov DL, Eichel RA, Notten PHL. Porous Electrode Modeling and its Applications to Li-Ion Batteries. Adv Energy Mater 2022;12:2201506. https://doi.org/10.1002/AENM.202201506.

[157] Zhao T, Zhu D, Li W, Li A, Zhang J. Novel design and synthesis of carbon-coated porous silicon particles as high-performance lithium-ion battery anodes. J Power Sources 2019;439:227027. https://doi.org/10.1016/J.JPOWSOUR.2019.227027.

[158] Xi F, Zhang Z, Wan X, Li S, Ma W, Chen X, et al. High-Performance Porous Silicon/Nanosilver Anodes from Industrial Low-Grade Silicon for Lithium-Ion Batteries. Cite This ACS Appl Mater Interfaces 2020;12:49089. https://doi.org/10.1021/acsami.0c14157.

[159] LFA 1000 - Aluminium oxide - Thermal diffusivity. Linseis n.d. https://www.linseis.com/en/applications/ceramics-and-glass-industry/lfa-1000-aluminum-oxide-al2o3-thermal-diffusivity-conductivity/ (accessed August 25, 2023).

[160] Sherwood J, Farmer TJ, Clark JH. Catalyst: Possible Consequences of the N-Methyl Pyrrolidone REACH Restriction. CHEMPR 2018;4:2010–2. https://doi.org/10.1016/j.chempr.2018.08.035.

[161] Entwistle J, Rennie A, Patwardhan S. A review of magnesiothermic reduction of silica to porous silicon for lithium-ion battery applications and beyond. J Mater Chem A

2018;6:18344–56. https://doi.org/10.1039/c8ta06370b.

[162] Tsuboi Y, Ura S, Takahiro K, Henmi T, Okada A, Wakasugi T, et al. Magnesiothermic reduction of silica glass substrate—Chemical states of silicon in the generated layers. J Asian Ceram Soc 2017;5:341–9. https://doi.org/10.1016/j.jascer.2017.06.010.

[163] Sing KSW, Everett DH, Haul RAW, Moscou L, Pierotti RA, Rouquerol J, et al. Reporting Physisorption Data for Gas/Solid Systems with Special Reference to the Determination of Surface Area and Porosity. Pure Appl Chem 1985;57. https://doi.org/10.1351/pac198557040603.

[164] Viera G, Mikikian M, Bertran E, Cabarrocas PRI, Boufendi L. Atomic structure of the nanocrystalline Si particles appearing in nanostructured Si thin films produced in low-temperature radiofrequency plasmas. J Appl Phys 2002;92:4684–94. https://doi.org/10.1063/1.1506382.

[165] Hatchard TD, Dahn JR. In Situ XRD and Electrochemical Study of the Reaction of Lithium with Amorphous Silicon. J Electrochem Soc 2004;151:A838. https://doi.org/10.1149/1.1739217.

[166] Curtis IS, Wills RJ, Dasog M. Photocatalytic hydrogen generation using mesoporous silicon nanoparticles: Influence of magnesiothermic reduction conditions and nanoparticle aging on the catalytic activity. Nanoscale 2021;13:2685–92. https://doi.org/10.1039/d0nr07463b.

[167] Meier C, Lüttjohann S, Kravets VG, Nienhaus H, Lorke A, Wiggers H. Raman properties of silicon nanoparticles. Phys E Low-Dimensional Syst Nanostructures 2006;32:155–8. https://doi.org/10.1016/j.physe.2005.12.030.

[168] Volodin VA, Koshelev DI. Quantitative analysis of hydrogen in amorphous silicon using Raman scattering spectroscopy. J Raman Spectrosc 2013;44:1760–4. https://doi.org/10.1002/jrs.4408.

[169] Huang Y, Zeng Y, Zhang Z, Guo X, Liao M, Shou C, et al. UV-Raman scattering of thin film Si with ultrathin silicon oxide tunnel contact for high efficiency crystal silicon solar cells. Sol Energy Mater Sol Cells 2019;192:154–60. https://doi.org/10.1016/j.solmat.2018.12.025.

[170] Li P, Kim H, Myung ST, Sun YK. Diverting Exploration of Silicon Anode into Practical Way: A Review Focused on Silicon-Graphite Composite for Lithium Ion Batteries. Energy Storage Mater 2021;35:550–76. https://doi.org/10.1016/j.ensm.2020.11.028.

[171] He S, Huang S, Wang S, Mizota I, Liu X, Hou X. Considering Critical Factors of Silicon/Graphite Anode Materials for Practical High-Energy Lithium-Ion Battery Applications. Energy and Fuels 2021;35:944–64. https://doi.org/10.1021/acs.energyfuels.0c02948.

[172] Moon J, Lee HC, Jung H, Wakita S, Cho S, Yoon J, et al. Interplay between electrochemical reactions and mechanical responses in silicon–graphite anodes and its impact on degradation. Nat Commun 2021;12. https://doi.org/10.1038/s41467-021-22662-7.

[173] Schmuch R, Wagner R, Hörpel G, Placke T, Winter M. Performance and cost of materials for lithium-based rechargeable automotive batteries. Nat Energy 2018;3:267–78. https://doi.org/10.1038/s41560-018-0107-2.

[174] Cao PF, Naguib M, Du Z, Stacy E, Li B, Hong T, et al. Effect of Binder Architecture on

the Performance of Silicon/Graphite Composite Anodes for Lithium Ion Batteries. ACS Appl Mater Interfaces 2018;10:3470–8. https://doi.org/10.1021/acsami.7b13205.

[175] Xu J, Wang X, Yuan N, Hu B, Ding J, Ge S. Graphite-based lithium ion battery with ultrafast charging and discharging and excellent low temperature performance. J Power Sources 2019;430:74–9. https://doi.org/10.1016/j.jpowsour.2019.05.024.

[176] Yi Z, Wang W, Qian Y, Liu X, Lin N, Qian Y. Mechanical Pressing Route for Scalable Preparation of Microstructured/Nanostrutured Si/Graphite Composite for Lithium Ion Battery Anodes. ACS Sustain Chem Eng 2018;6:14230–8. https://doi.org/10.1021/acssuschemeng.8b02880.

[177] Zhang L, Wang C, Dou Y, Cheng N, Cui D, Du Y, et al. A Yolk–Shell Structured Silicon Anode with Superior Conductivity and High Tap Density for Full Lithium-Ion Batteries. Angew Chemie - Int Ed 2019;58:8824–8. https://doi.org/10.1002/anie.201903709.

[178] Krause LJ, Brandt T, Chevrier VL, Jensen LD. Surface Area Increase of Silicon Alloys in Li-Ion Full Cells Measured by Isothermal Heat Flow Calorimetry. J Electrochem Soc 2017;164:A2277–82. https://doi.org/10.1149/2.0501712jes.

[179] Missyul A, Bolshakov I, Shpanchenko R. XRD study of phase transformations in lithiated graphite anodes by Rietveld method. Powder Diffr 2017;32:S56–62. https://doi.org/10.1017/S0885715617000458.

[180] Wetjen M, Pritzl D, Jung R, Solchenbach S, Ghadimi R, Gasteiger HA. Differentiating the Degradation Phenomena in Silicon-Graphite Electrodes for Lithium-Ion Batteries. J Electrochem Soc 2017;164:A2840–52. https://doi.org/10.1149/2.1921712jes.

[181] Yoon T, Nguyen CC, Seo DM, Lucht BL. Capacity Fading Mechanisms of Silicon

Nanoparticle Negative Electrodes for Lithium Ion Batteries. J Electrochem Soc 2015;162:A2325–30. https://doi.org/10.1149/2.0731512jes.

[182] Cheng YW, Chen CH, Wang SA, Li YC, Peng BL, Huang JH, et al. Propelling performance of silicon thin film lithium ion battery by appropriate dopants. Nano Energy 2022;102:107688. https://doi.org/10.1016/j.nanoen.2022.107688.

[183] Kim SY, Lee J, Kim BH, Kim YJ, Yang KS, Park MS. Facile Synthesis of Carbon-Coated Silicon/Graphite Spherical Composites for High-Performance Lithium-Ion Batteries. ACS Appl Mater Interfaces 2016;8:12109–17. https://doi.org/10.1021/acsami.5b11628.

[184] Yan Z, Yi S, Li X, Jiang J, Yang D, Du N. A scalable silicon/graphite anode with high silicon content for high-energy lithium-ion batteries. Mater Today Energy 2023;31:1–10. https://doi.org/10.1016/j.mtener.2022.101225.

[185] Jeong S, Li X, Zheng J, Yan P, Cao R, Jung HJ, et al. Hard carbon coated nano-Si/graphite composite as a high performance anode for Li-ion batteries. J Power Sources 2016;329:323–9. https://doi.org/10.1016/j.jpowsour.2016.08.089.

[186] Cao PF, Naguib M, Du Z, Stacy E, Li B, Hong T, et al. Effect of Binder Architecture on the Performance of Silicon/Graphite Composite Anodes for Lithium Ion Batteries. J Power Sources 2019;10:3470–8. https://doi.org/10.1021/acsami.7b13205.

[187] Wen Z, Lu G, Mao S, Kim H, Cui S, Yu K, et al. Silicon nanotube anode for lithium-ion batteries. Electrochem Commun 2013;29:67–70. https://doi.org/10.1016/j.elecom.2013.01.015.

[188] Lee W, Kim J, Yun S, Choi W, Kim H, Yoon WS. Multiscale factors in designing alkali-ion (Li, Na, and K) transition metal inorganic compounds for next-generation

rechargeable batteries. Energy Environ Sci 2020;13:4406–49. https://doi.org/10.1039/d0ee01277g.

[189] Park M, Zhang X, Chung M, Less GB, Sastry AM. A review of conduction phenomena in Li-ion batteries. J Power Sources 2010;195:7904–29. https://doi.org/10.1016/j.jpowsour.2010.06.060.

[190] Bard AJ, Faulkner LR. Electrochemical Methods Fundamentals and Applications. 2nd ed. Wiley; 2001. https://doi.org/10.1016/B978-0-12-381373-2.00056-9.

[191] Li J, Fang Q, Liu F, Liu Y. Analytical modeling of dislocation effect on diffusion induced stress in a cylindrical lithium ion battery electrode. J Power Sources 2014;272:121–7. https://doi.org/10.1016/j.jpowsour.2014.07.191.

[192] Cheng G, Zhang Y, Chang TH, Liu Q, Chen L, Lu WD, et al. In Situ Nano-thermomechanical Experiment Reveals Brittle to Ductile Transition in Silicon Nanowires. Nano Lett 2019;19:5327–34. https://doi.org/10.1021/acs.nanolett.9b01789.

[193] Christensen J, Newman J. A Mathematical Model of Stress Generation and Fracture in Lithium Manganese Oxide. J Electrochem Soc 2006;153:A1019. https://doi.org/10.1149/1.2185287.

[194] Gao X, Lu W, Xu J. Unlocking multiphysics design guidelines on Si/C composite nanostructures for high-energy-density and robust lithium-ion battery anode. Nano Energy 2021;81:105591. https://doi.org/10.1016/J.NANOEN.2020.105591.

[195] Dhillon S, Hernández G, Wagner NP, Svensson AM, Brandell D. Modelling capacity fade in silicon-graphite composite electrodes for lithium-ion batteries. Electrochim Acta 2021;377:138067. https://doi.org/10.1016/j.electacta.2021.138067.

[196] Ge M, Cao C, Biesold GM, Sewell CD, Hao S-M, Huang J, et al. Recent Advances in Silicon-Based Electrodes: From Fundamental Research toward Practical Applications. Adv Mater 2021;33:2004577. https://doi.org/10.1002/ADMA.202004577.

[197] Pilla S, Rao AM, Sabet M, Chen N. Hollow Porous Silicon Structures and Method of Formation. 11840454, 2023.

[198] Jia T, Zhong G, Lv Y, Li N, Liu Y, Yu X, et al. Prelithiation strategies for silicon-based anode in high energy density lithium-ion battery. Green Energy Environ 2022. https://doi.org/10.1016/j.gee.2022.08.005.